ผลของการเติมไอออนโลหะที่มีต่อโครงสร้างและสมบัติของเพอรอฟสไกต์ $Ba_{0.5}Sr_{0.5}Co_{0.8}Fe_{0.2}O_{3-\delta}$

นายวัชชรินทร์ งามพึงพิศ

วิทยานิพนธ์นี้เป็นส่วนหนึ่งของการศึกษาตามหลักสูตรปริญญาวิทยาศาสตรมหาบัณฑิต
สาขาวิชาเคมี ภาควิชาเคมี
คณะวิทยาศาสตร์ จุฬาลงกรณ์มหาวิทยาลัย
ปีการศึกษา 2550

EFFECTS OF DOPING METAL IONS ON STRUCTURES AND PROPERTIES OF PEROVSKITES $Ba_{0.5}Sr_{0.5}Co_{0.8}Fe_{0.2}O_{3-\delta}$

Mr. Watcharin Ngampeungpis

A Thesis Submitted in Partial Fulfillment of the Requirements
for the Degree of Master of Science Program in Chemistry
Faculty of Science
Chulalongkorn University
Academic Year 2007

Thesis Title	EFFECTS OF DOPING METAL IONS ON STRUCTURES AND PROPERTIES OF PEROVSKITES $Ba_{0.5}Sr_{0.5}Co_{0.8}Fe_{0.2}O_{3-\delta}$
By	Mr. Watcharin Ngampeungpis
Field of Study	Chemistry
Thesis Advisor	Assistant Professor Oravan Sanguanruang, Ph.D.
Thesis Co-avisor	Parichatr Vanalabhpatana, Ph.D.

Accepted by the Faculty of Science, Chulalongkorn University in Partial Fulfillment of the Requirements for the Master's Degree

S. Hannongbua .....Dean of the Faculty of Science

(Professor Supot Hannongbua, Ph. D.)

THESIS COMMITTEE

Sirirat Kokpol .....Chairman

(Associate Professor Sirirat Kokpol, Ph.D.)

Oravan Sanguanruang .....Thesis Advisor

(Assistant Professor Oravan Sanguanruang, Ph.D.)

Parichatr Vanalabhpatana .....Thesis Co-advisor

(Parichatr Vanalabhpatana, Ph.D.)

Laddawan Pdungsap .....External Member

(Assistant Professor Laddawan Pdungsap, Ph.D.)

Soamwadee Chaianansutcharit .....Member

(Assistant Professor Soamwadee Chaianansutcharit, Ph.D.)

นายวัชชรินทร์ งามพึงพิศ : ผลของการเติมไอออนโลหะที่มีต่อโครงสร้างและสมบัติของเพอรอฟสไกต์ $Ba_{0.5}Sr_{0.5}Co_{0.8}Fe_{0.2}O_{3-\delta}$ (EFFECTS OF DOPING METAL IONS ON STRUCTURES AND PROPERTIES OF PEROVSKITES $Ba_{0.5}Sr_{0.5}Co_{0.8}Fe_{0.2}O_{3-\delta}$) อาจารย์ที่ปรึกษา : ผศ.ดร. อรวรรณ สงวนเรือง อาจารย์ที่ปรึกษาร่วม : อ.ดร. ปาริฉัตร วนลาภพัฒนา 94 หน้า.

ทำการสังเคราะห์ $Ba_{0.5}Sr_{0.5}Co_{0.8}Fe_{0.2}O_{3-\delta}$ (BSCF5582) เพอรอฟสไกต์ที่มีการเติมไอออนโลหะ Pr และ La ที่ตำแหน่ง A และไอออน Mg, Ni, Zn และ Cu ที่ตำแหน่ง B ด้วยวิธีซิเตรตที่ดัดแปลง จากการตรวจสอบเอกลักษณ์ด้วยเทคนิค XRD และ SEM สารตัวอย่างที่เติม Pr, La, Zn และ Cu แสดงเฟสเดี่ยวที่มีโครงสร้างเป็นคิวบิกเพอรอฟสไกต์และไม่มีสารอื่นปน ยกเว้น BSCF5582 ที่เติม Cu 0.1 โมล แทน Fe ผลจากการตรวจสอบโดยใช้เทคนิค O_2–TPD แสดงว่าการเติมไอออนที่ตำแหน่ง A และ B ช่วยเพิ่มช่องว่างออกซิเจน การนำไฟฟ้าของสารที่เติมโลหะไอออนที่ตำแหน่ง A (Pr และ La) เพิ่มขึ้นเมื่อเพิ่มปริมาณของโลหะนั้น แต่การเติมไอออนที่ตำแหน่ง B ทำให้ค่าการนำไฟฟ้าลดลง การเติมไอออนทั้งที่ตำแหน่ง A และ B ทำให้ช่องว่างออกซิเจนและค่าการนำไฟฟ้าต่ำกว่าการเติมไอออนที่ตำแหน่ง A เพียงอย่างเดียว การเติม La 0.2 โมล ทำให้ค่าการนำไฟฟ้าสุดสุด (419.6 ซีเมนต์ต่อเซนติเมตร ที่ 450 องศาเซลเซียส) ซึ่งมากกว่าการนำไฟฟ้าของ BSCF5582 (53.7 ซีเมนต์ต่อเซนติเมตร ที่ 500 องศาเซลเซียส) ประมาณ 8 เท่า การขยายตัวทางความร้อนที่อุณหภูมิสูงของสารที่เติม Pr และ La เพิ่มขึ้นตามปริมาณที่เติมของไอออนชนิดนั้น ซึ่งเป็นผลมาจากการสูญเสียออกซิเจนในโครงสร้างผลึก ซึ่งก่อให้เกิดช่องว่างออกซิเจนในโครงสร้างเพอรอฟสไกต์

ภาควิชา เคมี ลายมือชื่อนิสิต วัชชรินทร์ งามพึงพิศ

สาขาวิชา เคมี ลายมือชื่ออาจารย์ที่ปรึกษา อรวรรณ สงวนเรือง

ปีการศึกษา 2550 ลายมือชื่ออาจารย์ที่ปรึกษาร่วม

4872453323: MAJOR CHEMISTRY
KEY WORD: PEROVSKITE OXIDE/ BSCF5582/ CATHODE MATERIAL

WATCHARIN NGAMPEUNGPIS: EFFECTS OF DOPING METAL IONS ON STRUCTURES AND PROPERTIES OF PEROVSKITES $Ba_{0.5}Sr_{0.5}Co_{0.8}Fe_{0.2}O_{3-\delta}$ THESIS ADVISOR: ASST PROF. ORAVAN SANGUANRUANG, Ph.D. THESIS CO-ADVISOR: PARICHATR VANALABHPATANA, Ph.D., 94 pp.

Doped with Pr and La ions at the A site and Mg, Ni, Zn, and Cu ions at the B site, $Ba_{0.5}Sr_{0.5}Co_{0.8}Fe_{0.2}O_{3-\delta}$ (BSCF5582) perovskites were synthesized by the modified citrate method. As the results, characterized by XRD and SEM, the Pr, La, Zn, and Cu specimens showed homogeneous and single phase with cubic perovskite structure, except Cu–doped BSCF5582 by replacing 0.1 mol Fe. O_2–TPD results demonstrated that the oxygen vacancies can be improved by doping A site and/or B site with metal ions. The electrical conductivity of BSCF5582 doped with metal ions at A site gradually increased with the amount of the metal ions (Pr and La). However, metal doping at the B site ions decreased the electrical conductivity. Also, the oxygen vacancies and electrical conductivity of BSCF5582 doped with metals at both A and B site were less than that of only A site. Doping with 0.2 mol La at the A site of BSCF5582 gave the material with the highest electrical conductivity (419.6 S/cm at 450°C), which was about 8 times higher than that of BSCF5582 (53.7 S/cm at 500°C). At high temperature, the thermal expansions coefficient of Pr or La specimens increased with the enhancement of Pr or La contents, due to the loss of lattice oxygen that caused the formation of oxygen vacancies in the perovskite structure.

Department	Chemistry	Student's Signature	Watcharin Ngampeung
Field of Study	Chemistry	Advisor's Signature	Oravan Sanguanruang
Academic year	2007	Co-Advisor's Signature	Parichatr Vanalabhpatana

ACKNOWLEDGEMENTS

The success of this thesis can be attributed to the extensive support and assistance from Assistant professor Dr. Oravan Saguanruang and Dr. Parichatr Vanalabhpatana. I deeply thank them for their valuable advice and guidance in this research and their kindness throughout this study.

I would like to gratitude to Professor Dr. Sirirat Kokpol, Assistant professor Dr. Soamwadee Chaianunsutcharit and Assistant professor Dr. Luddawan Pdungsap as the chairman and member of this thesis committee, respectively, for all of their kindness and useful advice in the research.

I would like to gratefully thank Dr. Thanakorn Wasanapiarnpong from Department of Material Science, Faculty of Science, Chulalongkorn University for supporting many instruments. Moreover, I would like to thank Department of Chemistry, Faculty of Science, Chulalongkorn University for the valuable knowledge and experience. I would like to thank the Graduate School Chulalongkorn University for supporting a research fund. In addition, Thailand Japan Technology Transfer Project supported a loan by Japan Banks for International Cooperation (TJTTP-JBIC) for instrument support. Furthermore, I would like to thank the members of Materials Chemistry and Catalysis Research Unit for consideration and generosity.

For all of my friends, I greatly appreciate their help and encouragement throughout the course of my research and study.

Finally, I would like to express my deepest gratitude to my family for their entirely care and support. The usefulness of this thesis, I dedicate to my family and all teachers who have taught me since my childhood.

CONTENTS

Page

Page

Page

LIST OF TABLES

Page

Page

LIST OF FIGURES

Figure **Page**

Page

Page

Page

LIST OF SCHEMES

Scheme **Page**

LIST OF ABBREVIATIONS

BSCF	$Ba_{0.5}Sr_{0.5}Co_{0.8}Fe_{0.2}O_{3-\delta}$
FeMg 0.05	$Ba_{0.5}Sr_{0.5}Co_{0.8}Fe_{0.15}Mg_{0.05}O_{3-\delta}$
FeNi 0.05	$Ba_{0.5}Sr_{0.5}Co_{0.8}Fe_{0.15}Ni_{0.05}O_{3-\delta}$
FeZn 0.05	$Ba_{0.5}Sr_{0.5}Co_{0.8}Fe_{0.15}Zn_{0.05}O_{3-\delta}$
FeCu 0.05	$Ba_{0.5}Sr_{0.5}Co_{0.8}Fe_{0.15}Cu_{0.05}O_{3-\delta}$
CoMg 0.05	$Ba_{0.5}Sr_{0.5}Co_{0.75}Fe_{0.2}Mg_{0.05}O_{3-\delta}$
CoNi 0.05	$Ba_{0.5}Sr_{0.5}Co_{0.75}Fe_{0.2}Ni_{0.05}O_{3-\delta}$
CoZn 0.05	$Ba_{0.5}Sr_{0.5}Co_{0.75}Fe_{0.2}Zn_{0.05}O_{3-\delta}$
CoCu 0.05	$Ba_{0.5}Sr_{0.5}Co_{0.75}Fe_{0.2}Cu_{0.05}O_{3-\delta}$
Pr 0.05	$(Ba_{0.5}Sr_{0.5})_{0.95}Pr_{0.05}Co_{0.8}Fe_{0.2}O_{3-\delta}$
La 0.05	$(Ba_{0.5}Sr_{0.5})_{0.95}La_{0.05}Co_{0.8}Fe_{0.2}O_{3-\delta}$
FeMg 0.1	$Ba_{0.5}Sr_{0.5}Co_{0.8}Fe_{0.1}Mg_{0.1}O_{3-\delta}$
FeNi 0.1	$Ba_{0.5}Sr_{0.5}Co_{0.8}Fe_{0.1}Ni_{0.1}O_{3-\delta}$
FeZn 0.1	$Ba_{0.5}Sr_{0.5}Co_{0.8}Fe_{0.1}Zn_{0.1}O_{3-\delta}$
FeCu 0.1	$Ba_{0.5}Sr_{0.5}Co_{0.8}Fe_{0.1}Cu_{0.1}O_{3-\delta}$
CoMg 0.1	$Ba_{0.5}Sr_{0.5}Co_{0.7}Fe_{0.2}Mg_{0.1}O_{3-\delta}$
CoNi 0.1	$Ba_{0.5}Sr_{0.5}Co_{0.7}Fe_{0.2}Ni_{0.1}O_{3-\delta}$
CoZn 0.1	$Ba_{0.5}Sr_{0.5}Co_{0.7}Fe_{0.2}Zn_{0.1}O_{3-\delta}$
CoCu 0.1	$Ba_{0.5}Sr_{0.5}Co_{0.7}Fe_{0.2}Cu_{0.1}O_{3-\delta}$
Pr 0.1	$(Ba_{0.5}Sr_{0.5})_{0.9}Pr_{0.1}Co_{0.8}Fe_{0.2}O_{3-\delta}$
La 0.1	$(Ba_{0.5}Sr_{0.5})_{0.9}La_{0.1}Co_{0.8}Fe_{0.2}O_{3-\delta}$
Pr 0.15	$(Ba_{0.5}Sr_{0.5})_{0.85}Pr_{0.15}Co_{0.8}Fe_{0.2}O_{3-\delta}$
La 0.15	$(Ba_{0.5}Sr_{0.5})_{0.85}La_{0.15}Co_{0.8}Fe_{0.2}O_{3-\delta}$
Pr 0.2	$(Ba_{0.5}Sr_{0.5})_{0.8}Pr02Co_{0.8}Fe_{0.2}O_{3-\delta}$
La 0.2	$(Ba_{0.5}Sr_{0.5})_{0.8}La_{0.2}Co_{0.8}Fe_{0.2}O_{3-\delta}$
Pr0.2FeCu0.05	$(Ba_{0.5}Sr_{0.5})_{0.8}Pr_{0.2}Co_{0.8}Fe_{0.15}Cu_{0.05}O_{3-\delta}$
La0.2FeCu0.05	$(Ba_{0.5}Sr_{0.5})_{0.8}La_{0.2}Co_{0.8}Fe_{0.15}Cu_{0.05}O_{3-\delta}$

°C	Degree celsius
a	Cubic unit lattice parameter
r	Ionic radius
t	Tolerance factor
σ	specific conductivity
TPD	Temperature-programmed desorption
μm	Micrometer
k	Temperature constant
n, m	Mechanism growth constant
X	Internal radius of the neck
Å	Angstrom
δ	Oxygen non-stoichiometry
D_v, k_r, k_f	Functions of temperature
ml	Milliliter
XRD	X-ray diffractrometer
SEM	Scanning electron microscopy
TGA	Thermogravimetric analysis
TCD	Thermal conductivity detector
TEC	Thermal expansion coefficient
CHP	Combined heat and power
R	Electrical resistance
V	Voltage
ρ	Specific resistance
A	Area
l	Length
I	Electrical current
ASR	Area specific resistance
STP	Standard temperature and pressure

CHAPTER I

INTRODUCTION

In the present, there are many advanced technologies for life facilitation especially transportation. The amount of fuel in the world has limited and its price is increasing everyday. Moreover, it makes a polluted problem in the world. Hence, most researchers have tried to find a new energy resource which is fuel cell.

1.1 Fuel cell

The fuel cell is a device that generates electricity by a chemical reaction. There are several kinds of fuel cells which are shown in Table 1 [1]

Table 1.1 Types of fuel cells

Fuel Cell Name	Electrolyte	Qualified Power (W)	Working Temperature (°C)	Electrical efficiency
Alkaline fuel cell (AFC)	Aqueous alkaline solution (e.g.,potassium hydroxide)	10 kW to 100 kW	under 80	Cell: 60–70% System: 62%
Direct methanol fuel cell (DMFC)	Polymer membrane (ionomer)	100 kW to 1MW	90–120	Cell: 20–30% System: 10–20%
Proton exchange membrane fuel cell (PEMFC)	Polymer membrane (ionomer) (e.g., Nafion® or Polybenzimidazole fiber)	100W to 500 kW	(Nafion) 70–120 (PBI)125–220	Cell: 50–70% System: 30–50%
Phosphoric acid fuel cell (PAFC)	Molten phosphoric acid (H_3PO_4)	up to 10MW	150-200	Cell: 55% System: 40% Co-Gen: 90%
Molten carbonate fuel cell (MCFC)	Molten alkaline carbonate (e.g., sodium bicarbonate $NaHCO_3$)	100MW	600-650	Cell: 55% System: 47%
Solid oxide fuel cell (SOFC)	O^{2-}-conducting ceramic oxide (e.g., zirconium dioxide, ZrO_2)	up to 100MW	700–1000	Cell: 60–70% System: 55–60%

Every fuel cell has two electrodes, one positive and one negative, named cathode and anode, respectively. The redox reactions that produce electricity take place at the electrodes.

1.2 Solid oxide fuel cell

A solid oxide fuel cell (SOFC) is a fuel cell which generates electricity directly from a chemical reaction, yet, unlike other fuel cells, an SOFC is composed entirely of solid-state materials, typically ceramics. Their composition also allows SOFC to operate at much higher temperatures than conventional fuel cells. SOFCs are intended mainly for stationary applications with an output from 1 kW to 2 MW. They work at very high temperatures, typically between 700 and 1,000ºC. Their off-gases can be used to fire a secondary gas turbine to improve electrical efficiency. Efficiency could reach as much as 70% in these hybrid systems, called combined heat and power (CHP) device. In these cells, oxygen ions are transferred through a solid oxide electrolyte material at high temperature to react with hydrogen molecule on the anode side.

Due to the high operating temperature of SOFC, they have no need for expensive catalyst, which is the case of proton-exchange fuel cells (platinum). This means that SOFC do not get poisoned by carbon monoxide and this makes them highly fuel-flexible. SOFCs have so far been operated on methane, propane, butane, fermentation gas, gasified biomass, and paint fumes. However, sulfur components present in the fuel must be removed before entering the cell, but this can easily be done by an activated carbon bed or a zinc absorbent. Thermal expansion demands a uniform and slow heating process at startup. Typically, 8 hours or more are to be expected. Micro-tubular geometries promise much faster start up times, typically 13 minutes. Unlike most other types of fuel cells, SOFC can have multiple geometries. The planar geometry is the typical sandwich type geometry employed by most types of fuel cells, where the electrolyte is sandwiched in between the electrodes. SOFC can also be made in tubular geometries where either air or fuel is passed through the inside of the tube and the other gas is passed along the outside of the tube. The tubular design is advantageous because it is much easier to seal and separate the fuel from the air compared to the planar design. However, the performance of the planar design is

currently better than the performance of the tubular design because the planar design has a lower resistance.

Planar SOFC is made up of four layers, three of which are ceramics (Figure 1.1). A single cell consisting of these four layers stacked together is typically only a few millimeters thick. Hundreds of these cells are then stacked together in series to form what most people refer to as a "solid oxide fuel cell." The ceramics used in SOFC do not become electrically and ionically active until they reach very high temperature and as a consequence the stacks have to run at temperatures ranging from 700 to 1,200 °C.

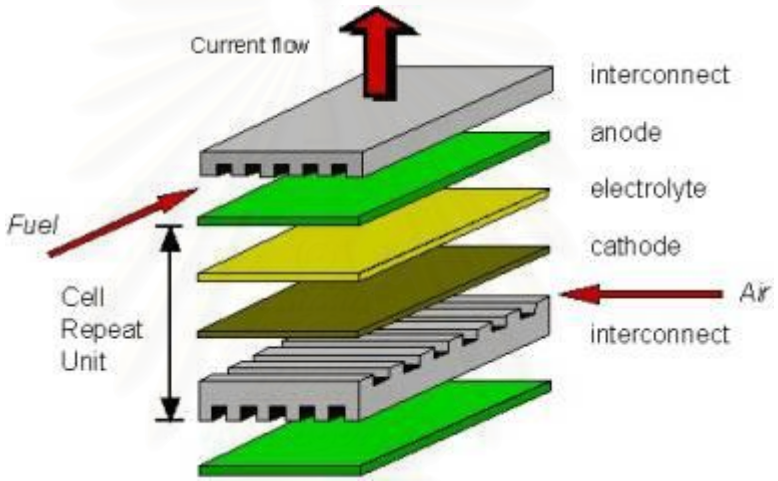

Figure 1.1 Configuration for a planar design SOFC

1.2.1 Cathode

The ceramic cathode layer must be porous, so that it allows air flow through it and into the electrolyte. There are various types of ceramic materials used for the cathode, but all of them must be electrically conductive. The cathode is the positive side of the cell towards which electrons flow. It is the side that is exposed to air and its purpose is to use electrons to reduce the oxygen molecules in the air to oxygen ions.

1.2.2 Electrolyte

The electrolyte is the dense, gas-tight layer of each cell that acts as a membrane separating the air on the cathode side from the fuel on the anode side.

There are many ceramic materials that are being studied for use as an electrolyte, but the most common are zirconium oxide based. Besides being air-tight, the electrolyte must also be electrically insulating so that the electrons resulting from the oxidation reaction on the anode side are forced to travel through an external circuit before reaching the cathode side. The most important requirement of the electrolyte, however is that it must be able to conduct oxygen ions from the cathode to the anode. For this reason, the suitability of an electrolyte material is typically measured in ionic conductivity.

1.2.3 Anode

The ceramic anode layer must be very porous to allow the fuel to flow to the electrolyte. Like the cathode, it must conduct electricity. The most common material used is a cermet made up of nickel mixed with the ceramic material that is used for the electrolyte in that particular cell. The anode is commonly the thickest and strongest layer in each individual cell, and is often the layer that provides the mechanical support. Electrochemically speaking, the anode's job is to use the oxygen ions that diffuse through the electrolyte to oxidize the hydrogen fuel. The oxidation reaction between the oxygen ions and the hydrogen molecule produces both water and electricity.

1.2.4 Interconnect

Interconnect can be either a metallic or ceramic layer that sits between each individual cell. Its purpose is to connect each cell in series, so that the electricity each cell generates can be combined. Because interconnect is exposed to both the oxidizing and reducing side of the cell at high temperatures, it must be extremely stable. For this reason, ceramics have been more successful in the long term than metals as interconnect materials. However, these ceramic interconnect materials are extremely expensive. Fortunately, inexpensive metallic materials are becoming more promising as lower temperature (600-800°C) SOFCs are developed.

1.2.5 Operation of SOFC

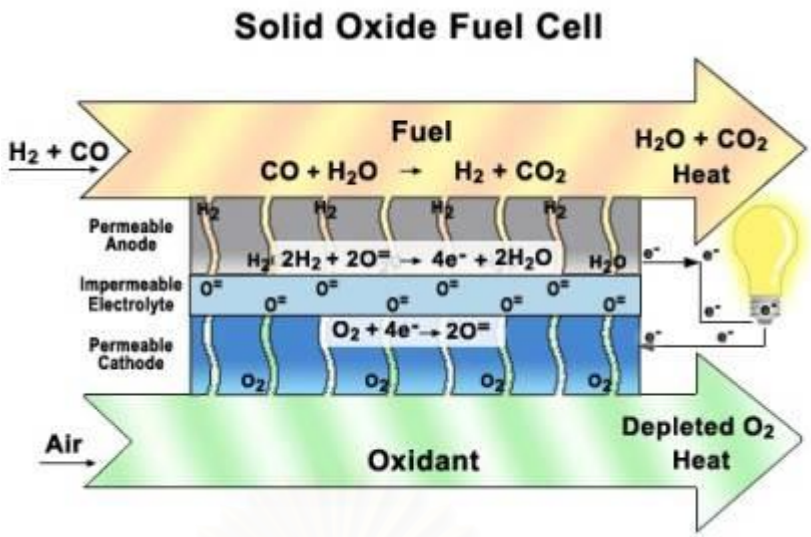

Figure 1.2 Operating concept of a SOFC

Figure 1.2 shows schematically how a SOFC works. The cell is constructed with two porous electrodes that sandwich an electrolyte. Air flows along the cathode (which is therefore also called the "air electrode"). When an oxygen molecule contacts the cathode/electrolyte interface, it catalytically acquires four electrons from the cathode and splits into two oxygen ions. The oxygen ions diffuse into the electrolyte material and migrate to the other side of the cell where they encounter the anode (also called the "fuel electrode"). The oxygen ions encounter the fuel at the anode/electrolyte interface and react catalytically, giving off water, carbon dioxide, heat, and most importantly electrons. The electrons transport through the anode to the external circuit and back to the cathode, providing a source of useful electrical energy in an external circuit.

Over the past years, there has been a continuous interest of investigating perovskite-type (ABO_3) complex oxides because of their superior mixed electronic-ionic conducting properties, making them promising candidate materials for many technical applications, including cathodes for SOFC.

1.3 Perovskite [2]

Perovskite is an inorganic compound that the ideal structure is primitive cube. Perovskite (calcium titanium oxide, $CaTiO_3$) was discovered in the Ural mountains of Russia by G. Rose in 1839 and named for Russian mineralogist, L. A. Perovski (1792-1856). Under the high pressure conditions of the mantle, the

pyroxene enstatite, $MgSiO_3$, is a perovskite polymorph and may be the most common mineral in the Earth. Perovskite is also the name of a more general group of crystals which take the same structure. There are many kinds of perovskites such as oxides, some carbides, nitrides, halides, and hydrides also crystallize in this structure. However, the most interesting perovskite are oxides because they have ionic and electronic conducting properties.

1.3.1 Structure of perovskite oxide [3]

1.3.1.1 Crystal structure

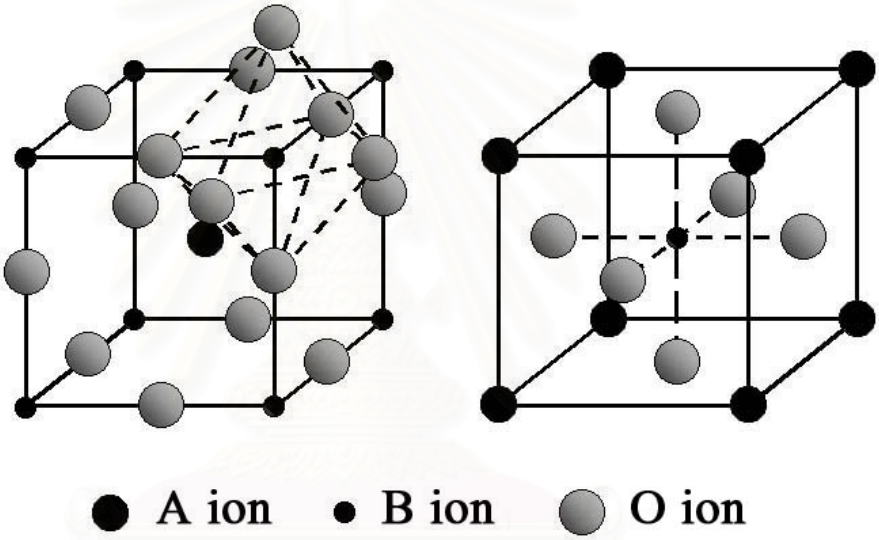

Figure 1.3 ABO_3 ideal perovskite structure showing oxygen octahedron containing the B ion linked through corners to form a three-dimensional cubic lattice.

The crystal structure of perovskite oxide ABO_3 is primitive cube. In the unit formula of ABO_3, A is the larger cation and B is the smaller cation. In this structure, the B cation is 6-fold coordinated and the A cation is 12-fold coordinated with the oxygen anions. Figure 1.3 depicts the corner sharing octahedra that form the skeleton of the structure, in which the center position is occupied by the A cation. Alternatively, this structure can be viewed with the B cation placed in the center of the octahedron and the A cation is in the center of the cube.

In the ideal perovskite structure, the size and coordination preferences of three or more ions need to be satisfied simultaneously by the structure; it is, however, rarely possible that all these choice can be accommodated perfectly. This

can be illustrated for the perovskite structure by deriving a relationship between the radii of the various ions. Figure 1.4 shows the relationship between ionic radii in the perovskite structure.

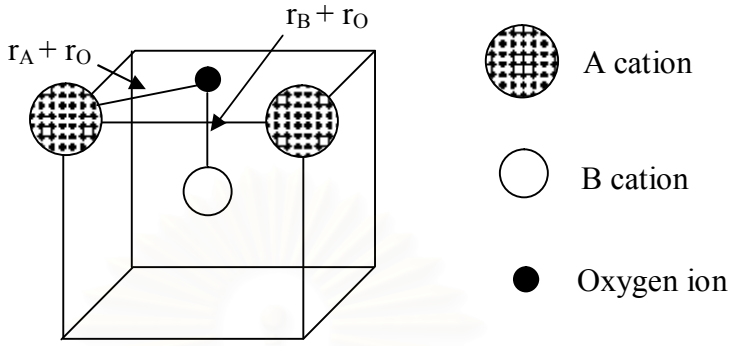

Figure 1.4 The relationship of ionic radii in perovskite structure.

$$a = 2xB - O = 2(r_B + r_O) \tag{1.1}$$

and

$$a = \frac{1}{\sqrt{2}} x2xA - O = \sqrt{2}(r_A + r_O) \tag{1.2}$$

hence,

$$2x(r_B + r_O) = \sqrt{2}x(r_A + r_O) \tag{1.3}$$

where the atoms are touching one another, the B-O distance is equal to $a/2$ (a is the cubic unit cell parameter) while the A-O distance is ($a/\sqrt{2}$) and the following relationship between the ionic radius (r) holds shown in Equation 1.3. In general, the perovskite structure is formed if the tolerance factor, t.

$$t = \frac{(r_A + r_O)}{\sqrt{2}(r_B + r_O)} \tag{1.4}$$

The ideal perovskite is the cubic structure with the tolerance factor close to 1.0 at high temperature. The perovskite structure is stable in the range $0.75 < t < 1.0$, and is cubic in the range $t > 0.95$. Deviations from the ideal structure are well known as orthorhombic, rhombohedral, tetragonal, monoclinic, and triclinic symmetry. The distorted structure may exist at room temperature but it transforms to the cubic structure at ambient temperature.

1.3.1.2 Oxygen nonstoichiometry

Oxygen excess nonstoichiometry in perovskite oxides is not as common as anion-deficient nonstoichiometry probably because introduction of interstitial oxygen in perovskite structure is thermodynamically unfavorable. A few systems display apparent oxygen excess, including $LaMnO_{3+\lambda}$, $Ba_{1-\lambda}La_{\lambda}TiO_{3+\lambda/2}$ and $EuTiO_{3+\lambda}$. There are two reasons occur of oxygen excess nonstoichiometry. First, because the trivalent cation vacancies cause a large electronic imbalance and local lattice distortion, it does not stay close to each other. Second, with the formation of cation vacancies, a nonbonding O2p level is formed by the oxide ions around the vacancies. This nonbonding O2p level serves as the hole-trap.

Many oxygen-deficient perovskites can be described on the basis of complex perovskite-related superstructures of general formula $A_nB_nO_{3n-1}$, in which the stacking manner depends on the size, electronic configurations, and coordination numbers of A and B cations. Oxygen vacancies are accomplished by substituting ions of similar size but different valence. For example, some of the La^{3+} ions in $LaBO_3$ are replaced by Sr^{2+} to form $La_{1-x}Sr_xBO_{3-\delta}$, and therefore, oxygen vacancies are formed in the structure.

1.3.2 Physical properties of perovskite

The ABO_3 perovskites display several interesting physical properties such as ferroelectricity ($BaTiO_3$), ferromagnetism ($SrRuO_3$), weak ferromagnetism ($LaFeO_3$), superconductivity ($YBa_2Cu_3O_7$), large thermal conductivity due to excitation transport ($LaCoO_3$), insulator-to-metallic transitions of interest for thermistor applications ($LaCoO_3$), a fluorescence compatible with laser action ($LaAlO_3$: Nd), and transport properties of interest for high temperature thermoelectric power (La_2CuO_4).

1.3.2.1 Magnetic Properties

In the ideal cubic perovskite structure, each oxygen is shared by two B^{3+} ions, forming a B-O-B angle of 180°. Such a configuration is favorable for

superexchange interactions between magnetic B^{3+} cations. This exchange usually results in antiparallel coupling of nearest-neighbor magnetic moments. When the B^{3+} ions are in two sublattices ($A_2BB'O_6$), other spin arrangements are possible. If B′ is a diamagnetic ion, the B^{3+} ions are aligned antiferromagnetically, and the most important exchange mechanism is believed to be a longer range superexchange interaction through two oxygens of the B-O-B′-O-B type. The B-B separation is now considerably longer than the 0.4 nm separation found in the ideal perovskite. The $LnFeO_3$ (Ln = lanthanide) perovskites are those that have attracted the most attention because of their possible applications as technological magnetic materials. These compounds show a weak spontaneous magnetic moment, which is attributed to a slight canting of the iron moments, which are otherwise antiferromagnetically aligned. The iron moments align in such a way that the direction of easy magnetization is along the *a* or *c* axis of the orthorhombic cell. The weak ferromagnetic moment of 0.03-0.07 μ_B/mol led to the materials being considered for memory devices. Similarly, $LnMnO_3$ shows very interesting magnetic properties. These manganites containing mostly Mn^{3+} or Mn^{4+} ions show antiferromagnetic behavior. However, ferromagnetic behavior is observed in the range from 25 to 35% Mn^{4+}. A weak magnetic interaction was found between Mn^{3+} ions, together with a negative interaction between Mn^{4+} ions and a strong positive interaction between Mn^{3+} and Mn^{4+}. A similar kind of behavior was found for the combination of Co^{3+} and Co^{4+}, but the Cr and Fe compounds were found to be antiferromagnetic.

1.3.2.2 Electrical Properties

The electrical conductivity of perovskites also shows wide variations. Several compounds have been used for their dielectric properties, while others show metallic conductivity, although most are semiconductors. As for other compounds, the electrical behavior in perovskites depends on the outermost electrons, which may be localized at specific atomic sites or may be collective. Since localized electrons may carry a spontaneous moment, there is a strong correlation between the electrical and magnetic properties of perovskites. Rare-earth perovskites containing transition ions show widely differing electrical

properties. For example, $LaNiO_3$, which contains nickel in the low-spin state Ni^{III}, and $LaTiO_3$, which exhibit collective d-electron behavior, showing a metallic conductivity and Pauli paramagnetism. In the $LnCrO_3$ (Ln = lanthanide) perovskite series, $LaCrO_3$ is a semiconductor. For the heavier chromites, there seem to be two regions of conductivity. In the low-temperature region, the activation energy increases along the lanthanide series (from 0.27 eV for Dy to 0.37 eV for Yb), while the high-temperature region is characterized by a value of about 0.23 eV. The mechanism of conduction is attributed to the presence of high mobility Cr^{4+} ions giving rise to p-type extrinsic conduction. The decrease in conductivity in the heavier chromites may be related to a decrease in the covalence of the Cr-O bond and an increased covalence of the Ln-O bond. $LaMnO_3$ perovskite exhibited an abrupt change in conductivity as well as in magnetic susceptibility as a function of temperature close to 447°C. This behavior was explained on the basis that the charge carriers would be holes hopping among localized levels. $LaCoO_3$ displays an even more complex behavior. It is a semiconductor up to about 127°C, after which conductivity increases much more rapidly up to 550°C; in the region from 550 to 927°C it passes through a broad, flat maximum, and, finally, above 927°C it shows a metal-like behavior. At low temperatures, the Co ions are mainly in the low-spin Co^{III} state, and this coexists with the high-spin paramagnetic Co^{3+} state at higher temperatures. As the temperature is further increased, the Co^{3+} and Co^{3+} ion pairs transform to Co^{2+} and Co^{4+} pairs. Thus, the fraction of Co^{3+} disappears around 927°C when only long-range order is present, resulting in a first-order transition. Along with the spin behavior, the outer electrons also show a transition from the localized to a collective behavior. Conductivity can be enhanced considerably by partial substitution of the lanthanide by a divalent ion. Thus, for $Sr_xLa_{1-x}MnO_3$ the Mn ions are Mn^{3+} for x = 0. However, an increase in x results in the creation of Mn^{4+} holes, thereby increasing conductivity. For substitutions $0.2 < x < 0.4$ the system becomes ferromagnetic and shows a metal-semiconductor transformation. A similar type of behavior was observed in Sr-substituted obaltites. The electrical properties of perovskites have aroused special interest since the discovery in 1986 of superconductivity at 40 K in cuprates. These cuprates are hole superconductors, exhibiting a mixed valence of copper Cu^{II}-Cu^{III}. Among these, the exception is Ce doped Nd_2CuO_4, with Tc close to –248°C which belongs to a

different structural type and is an electron superconductor. All these compounds have a common feature, the bidimensional character of the structure, which has been shown to be an important factor for the existence of superconductivity at high temperature.

1.3.2.3 Mixed ionic-electronic conductors

Perovskite oxides show both ionic and electronic conductivity for example $La_{1-x}Sr_xBO_{3-\delta}$. When the B ions can take a mixed-valence state, charge neutrality is maintained by both the formations of oxygen vacancies and a change in the valence state of the B ions. The oxides may show both high oxygen ion conductivity due to the high oxygen vacancy concentration, and a high electronic conductivity due to the mixed-valence state [4]. The concentration of oxygen vacancies can also be increased by mild B-site ion substitution, such as Cu and Ni ions, which naturally take the divalent oxidation state [5]. If the valence state of the B ions is fixed, neutrality is maintained only by the formation of oxygen vacancies. The oxides may be predominantly ionic conductors, in this case.

1.3.3 Perovskite synthesis [2]

There are three steps for preparing perovskite membrane

1. Powder synthesis
2. Shaping
3. Sintering

Powder synthesis is the first step to play a critical role in determining the particle size of the powder, and consequently has an effect on the microstructure of the membrane. There are many routes to synthesize powders, such as a conventional solid-state reaction method and a wet chemical process that includes thermal decomposition of cyanide, metal–EDTA, chemical co-precipitation and the sol–gel process. Cui and Liu [6] reported in their study that powders synthesized by different methods had different temperatures of crystal transformation and the surface defect of powders dried by a supercritical method improved the formation of the crystal structure.

thermal decomposition of cyanide, metal-EDTA, chemical co-precipitation and the sol-gel process. Cui and Liu [6] reported in thir study that powders synthesized by different methods had different temperatures of crystal transformation and the surface defect of powders dried by a supercritical method improved the formation of the crytal structure

The synthesis of perovskite powder has been achieved by many methods, including a conventional solid-state reaction method and a solution reaction that includes thermal decomposition of cyanide, metal-EDTA, chemical co-precipitation and the sol-gel process etc.

1.3.3.1 Solid-state reaction

The solid state reaction is a method to synthesize perovskite oxides because it is a very convenient method. However, the impurities are introduced from raw materials, milling media, and the calcination container. Because of the high temperature required for the complete reaction. Conventional processing of the perovskite-related materials uses solid-state reactions between metal-carbonates, hydroxides, and oxides. LSCF represents a typical case. Raw materials La_2O_3, $SrCO_3$, CoO_3, and Fe_2O_3 were mixed and ball-milled. After drying, then the mixed powders were calcined at 1,000°C to remove impurities and to achieve single-phase perovskite powder.

1.3.3.2 Gas phase reaction

The deposition of perovskite films with a specific thickness and composition generally requires gas phase reaction or transport. Many physical techniques have been developed for gas phase deposition such laser ablation, molecular beam epitaxy, dc sputtering, magnetron sputtering, electron beam evaporation and thermal evaporation. In general, they can be divided into two categories based on the target they use. The first type uses separate targets where a different speed of deposition for each element has to be determined. The second method uses the performed perovskite material itself as target and the stoichiometric phase is transported to the substrate by sputtering or ablation techniques. Gas depositions can be divided further into three categories: (1)

deposition at low substrate temperature followed by a post-annealing at elevated temperatures, (2) deposition at intermediate temperature of 600 to 900°C, and (3) deposition at crystallization temperature under an appropriate atmosphere.

1.3.3.3 Solution reaction

Solution reactions have been developed from solid-state synthesis to produce the required properties of raw perovskite powders, such as spray-pyrolysis, freeze drying, precipitation, sol-gel and liquid mix process, etc. Because of the conventional solid-state synthesis promotes the crystal growth and resulting in a hard agglomeration. The perovskite powders made from solution chemical methods are very fine, and can not be agglomerated, which facilitates the densification process. This method using sintering temperature which can be lower than those made from conventional solid-state synthesis methods.

The initial process was pioneered by Pechini and is referred to either as Pechini process [7]. This method includes first dissolving hydrous oxides or alkoxides of the elements in a polyhydroxy alcohol such as ethylene glycol, with a chelating agent, such as citric acid. Then polyhydroxy alcohol such as ethylene glycol is added and the liquid is heated to 150 to 250°C to allow the chelates to undergo polyesterification. Heating is continued to remove excess water, resulting in solid polymeric resin. The temperature is increased to about 400°C to char or decompose the resin. The temperature is further increased to 500 to 900°C to form crystallites of the mixed oxide composition. The crystallites are typically 20 to 50 nm and clustered into agglomerates. An advantage of the Pechini method is that the viscosity and polymer molecular weight of the solution can be tailored by varying the citric acid/ethylene glycol ratio and the solution synthesis temperature.

The modifications of Pichini process have been developed. One was called amorphous citrate process that involves producing precursor from citric acid and metal nitrate before thermal decomposition. Baythoun and Sale investigated the production of Sr-substituted $LaMnO_3$ perovskite powder by the amorphous citrate process, the manganese citrate-nitrate precursor may be revealed as in equation (1.5).

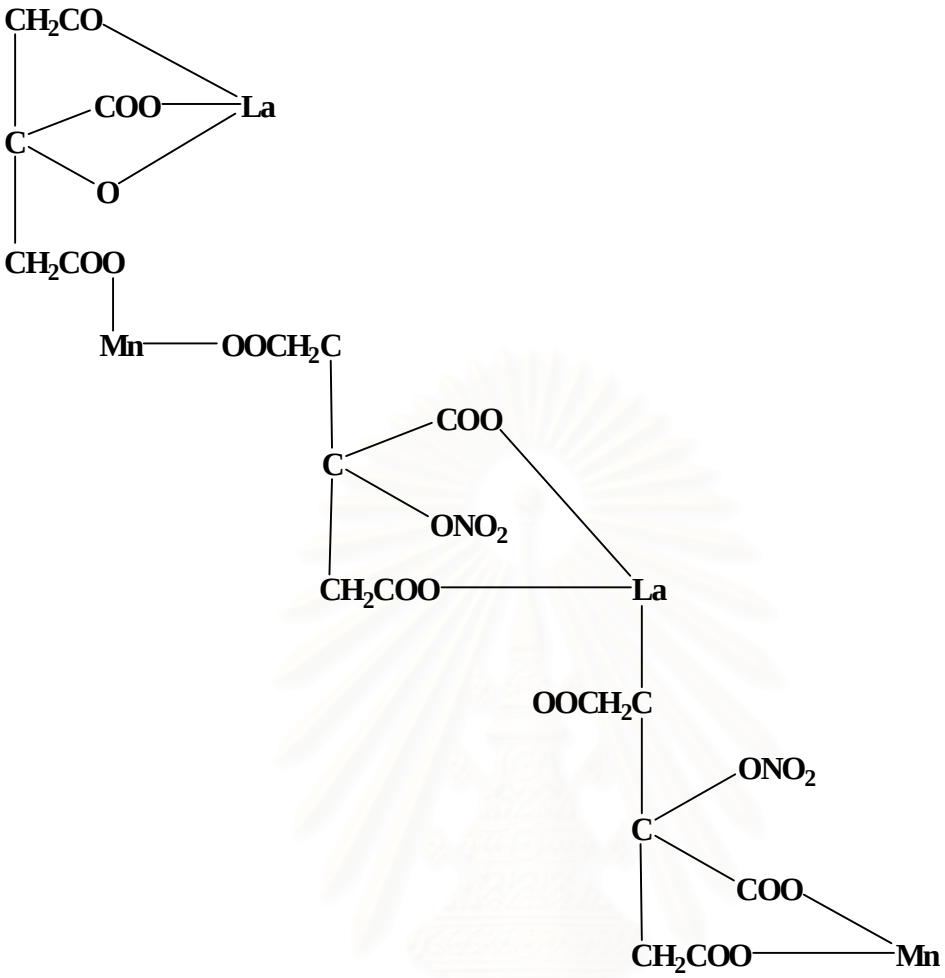

(1.5)

In the complex the lanthanum is triply charged and replaces in one case the hydrogen of three –COOH groups (as in normal citrate formation) and in another case it replaces the hydrogen of one –OH group and two –COOH groups. Manganese in the divalent state replaces the hydrogen in two –COOH groups while NO_2 replaces the hydrogen of one –OH group

The amounts of metal and citric acid should not less than equimolar. In all cases the minimum amount of citric acid used was that necessary to bond the metals if all the NO_3^- ions were replaced. If the high amount of citric acid was used, Mn_2O_3 was presented from the complex as shown in equation (1.6):

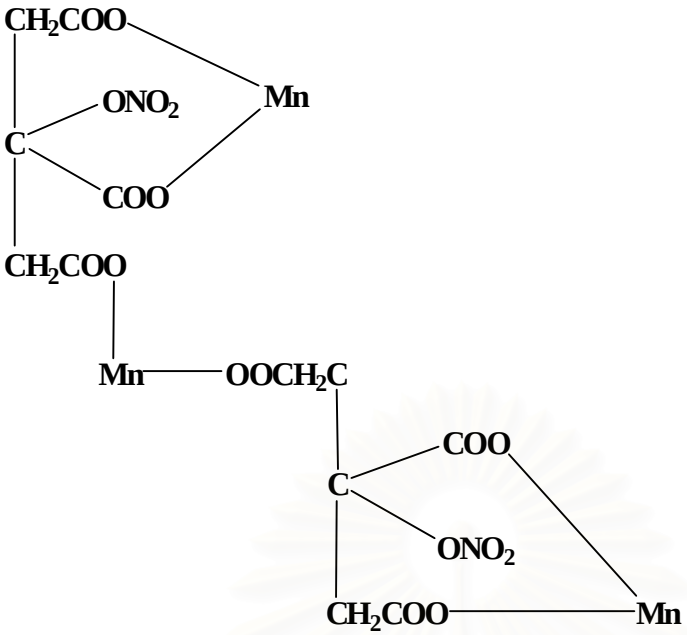

(1.6)

In this case, structure would allow some citric acid, water, and nitrate ions to be lost during the preparation of gel. Every three molecules of citric originally present one remains uncombined and may be removed from the mixture by either evaporation or decomposition to yield acetone, carbon dioxide and water during the precursor preparation in the vacuum oven.

Suresh et al. [8] synthesized $La_{1-x}Sr_xFeO_3$ where x = 0.0-1.0 by the solution combustion method using corresponding metal nitrates, oxalyl dihydrazide (ODH) or tetraformal trisazine (TFTA). Theoretical equation for the formation of ferrite $(LaSr)FeO_3$ assuming complete combustion of the redox mixtures can be written as equation 1.7 :

$$(1\text{-}X)La(NO_3)_3 + XSr(NO_3)_2 + Fe(NO_3)_3 + 3(CON_2H_3)_2 \; ; \; X = 0\text{-}1.0$$

$$\downarrow$$

$$La_{1-X}Sr_XFeO + 6CO_2\ (g) + 9H_2O\ (g) + 9N_2\ (g) \qquad (1.7)$$

(24 mol of gases /mol of $LaSrFeO_3$)

The powder densities and surface area of TFTA derived ferrites were found to be higher than those of ODH derived ferrites. The average agglomerate size distribution is narrower for ODH derived ferrites than the TFTA ferrites and the average agglomerate sizes are 0.89 μm and 4.8 μm respectively.

The perovskite powders made by wet chemical methods are very fine, and can be no agglomerated, which facilitates the densification process. The sintering temperature can be several hundred degrees Celsius lower for the powders made by wet chemical methods than for those made by conventional solid-state synthesis methods. When comparing several techniques in wet chemical methods, liquid mix process is distinguished in the case of less energy consumption, simplest technology, and potential to get fine particles and a single-phase powder. Both adding several acids such as citric, malic acid, or etc. and adjusting the pH of aqueous solution are used to provide the fine homogeneous perovskite with the high surface area.

1.3.4 Powder sizing

Powder particles are influenced on compacting and sintering. In most cases the objective of the pressing step is to achieve maximum particle packing and uniformity, so that minimum shrinkage and retained porosity will result during densification. A single particle size does not produce good packing. Optimum packing for particles all the same size results in over 30% void space. Adding particles of a size equivalent to the largest voids reduces the void pore volume to 23%. Therefore, to achieve maximum particle packing, a range of particle sizes is required.

Hard and dense agglomerates in ceramic powders usually result in large interagglomerate pores after sintering. Therefore, small particle size is important because it facilitates the high strength of green disc and the sintering process. The primary driving force for densification of a compact powder at high temperature is the change in surface free energy. Very small particles have high surface areas. The high surface free energy and very strong thermodynamic driving force decrease their surface by bonding them together. The particle with approximate sizes of 1 μm or less can be compacted into a porous shape and sintered at a high temperature to near-theoretical density [9]. Typically, the finer the powder, the greater its surface area, and the lower the temperature and shorter time for densification. Long time of the sintering temperature causes of the increasing in grain growth and lowering strength.

Calcined powder is not usually available with the optimum particle size distribution. The ball milling and screening are the common techniques to achieve the desire particle size of powder.

1.3.5 Powder compacting by uniaxial pressing [9]

Uniaxial pressing is accomplished by placing the powder in to a rigid die and applying pressure along a single axial direction through a rigid plunger, or piston to achieve compacting. Pressing results in the direct contact of particles, reduces the average distance between particles, and changes the shape of particles. The apparent density of a compact was controlled by mixing of the proper various particles size fractions.

To enhance the compacting, before pressing, the powder should be disaggregated by mixing the powder with solvent such as isopropanol in the ultrasonic bath or added a couple drops of acetone to reduce the surface tension.

1.3.6 Sintering [10]

Sintering is a process that is the thermal treatment of a powder or compact at a temperature below the melting point of the main constituent, for the purpose of increasing its strength by bonding together of the particles. The driving force for sintering is the decrease in surface free energy that occurs as the surface area of the polycrystalline aggregate is reduced. This process can be achieved by solid-state reaction or alternatively in the presence of a liquid phase. When a powder aggregate is sintered, necks form between the particles, and the aggregate may increase in density. The growth of the neck is due to the transport of matter or of the counter-flow of vacancies between the particles and the pores. In crystalline powder, its transport occurs by diffusion (bulk, surface, or grain boundary diffusion), whereas in amorphous materials, it occurs by viscous flow. Kuczynski has defined the neck growth as in equation (1.8).

$$X^n/r^m = kt \qquad (1.8)$$

Where X and r are defined in Figure 1.5, t is the time, k is the temperature dependent constant, n and m are constants dependent on the mechanisms of growth, viscous or bulk diffusion, surface diffusion, or evaporation and condensation. Three stages of sintering can be distinguished. The early stage or initial stages during which the necks form at points of particle contact and the particles usually center approach each other. At this stage the individual particles are still distinguishable. The intermediate stage during that the necks become large, resulting in the formation of an interconnected pore structure. The third or the final stages during, the pores become isolated. Elimination of the interconnectivity of pores eliminates surface and vapor transport.

Closed pores isolated from grain boundaries shrink very slowly because grain boundary diffusion is far away from the pores. The growth of grains, therefore, hinders the attainment of theoretical density, since the pore's growth is also enhanced. It is essential, therefore, to retard grain growth so that densification of the compact can continue to the theoretical limit. This is particularly important with the present trend of using ultrafine particles as starting materials for the fabrication of technical ceramics. Surface diffusion becomes important in the case of very fine particles. Grain boundary diffusion and volume diffusion are the main mechanisms causing shrinkage of the neck, whereas surface diffusion does not contribute to any shrinkage. The most important diffusion paths during the sintering of two spheres with a grain boundary are surface diffusion, grain boundary diffusion, volume diffusion from the grain boundary to the neck surface, and volume diffusion from the sphere surface to the neck surface. The sintering rate also affected by the crystallization and growth processes, which occur concurrently. The sintering rate is reduced when there is intensive grain growth because when diffusion forms the pores occurs toward the boundaries of individual grains, the distance over which diffusion occurs with a reduction in pores is determined by the size of the crystals.

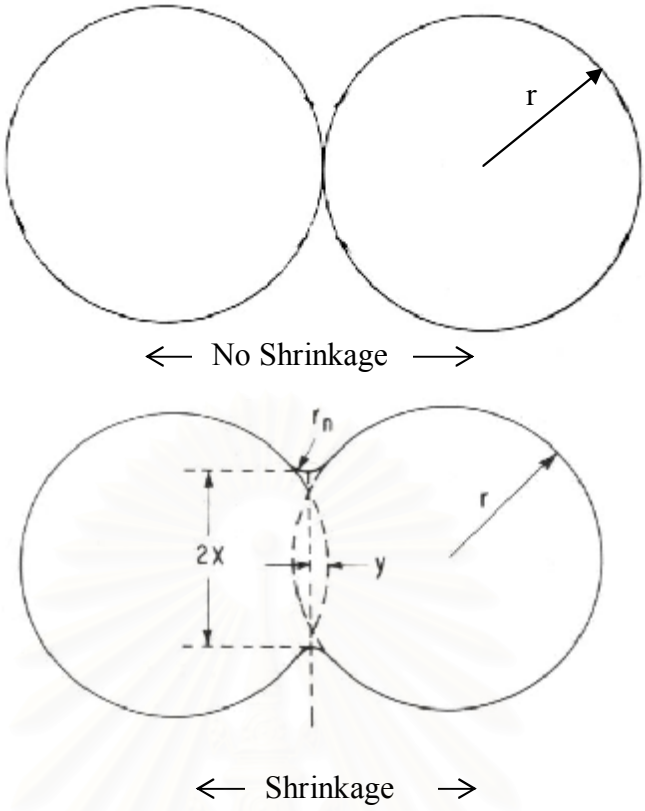

Figure 1.5 Mechanism of sintering; *X* is the internal radius of the neck; *r* is the particle radius.

1.4 Electrical measurement

1.4.1 Two-Point Measurements

$$R = \frac{V}{I} \qquad (1.9)$$

Ohm's law is used in order to determine a resistance. A known current is sourced and flows through the unknown resistance while the voltage developed across the resistance is measured. Dividing the measured voltage by the sourced current, the resistance can be obtained. A problem that occurs when using a 2-wire setup is that the voltage is measured not only across the resistance in question, but also the resistance of the electrode and contacts. When using an ohmmeter to measure resistances above a few ohms, the added resistance is usually 2-point measurement. However, when measuring low resistances or using contact resistance, obtaining accurate results with a 2–wire measurement could be a problem.

1.4.2 Four-Point Measurements

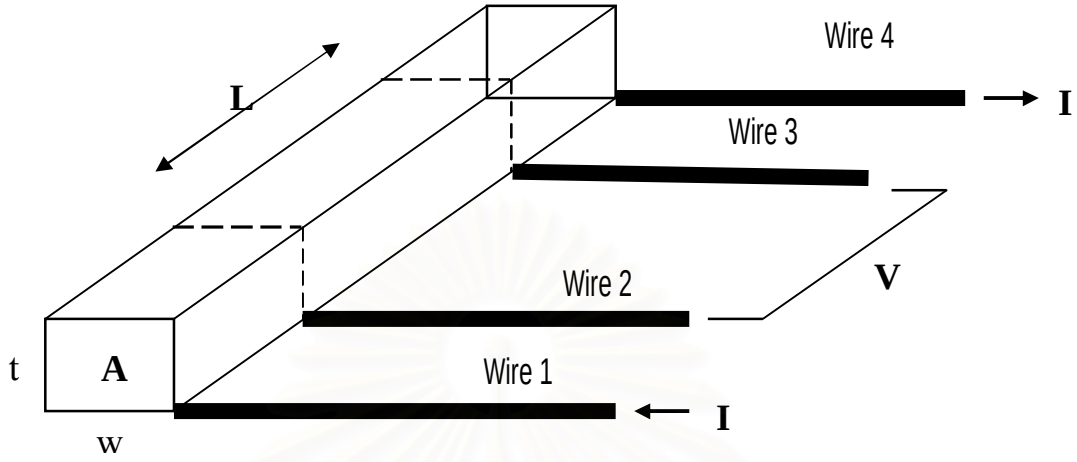

Figure 1.6 4-DC probe measurement

A solution to the problem of 2-point measurement in which the lead and contact resistance is measured along with that of the device under test is the 4-wire or "Kelvin" measurement. Because a second set of probes is used for sensing and negligible current flows in these probes, only the voltage drop across the device under test is measured. As a result, resistance measurement or I-V curve generation is more accurate.

The measurement method then includes a forced current I through the outer wires 1 and 4 and a measurement of the voltage drop over wire 2 and 3, using a very high ohmic measurement device, so that the current flowing through wire 2 and 3 is nearly zero. In that case the individual, additional contact resistance does not play a role as it cancels out of the equation. To study the behavior of the structure an I/V curve is generated, typically in the μA to the mA range. If the graph shows a straight line, the structure behaves as an Ohmic resistor. If R represent the resistance of a structure, the following applies:

$$R = \frac{rL}{A} \qquad (1.10)$$

With L = the length of the structure (m)

A = the area (width × thickness) of the cross section (m^2)

ρ = the specific resistivity (Ω.m)

1.5 Literature review

In 1989, Tereoka et al. investigated the catalytic activities of the $La_{1-x}Sr_xCo_{1-y}Fe_yO_{3-\delta}$ perovskite-type oxides for the combustion of n-butane and methane as well as H_2O_2 decomposition in an alkaline solution. The amount of oxygen desorbed increased with increasing Sr content at a fixed B-site composition, for which an increase in the number of oxide ion vacancies with x was responsible. On the other hand, the total amount of oxygen desorbed was hardly affected by B-site composition, but partial substitution of Fe for Co enhanced desorption and sorption of oxygen particularly in the low-temperature region. Substitution of Sr for La as well as of Fe for Co was found to promote catalytic activity, though the activity changed with oxide composition in a manner dependent on the kind of reactant [11].

$Ba_{0.5}Sr_{0.5}Co_{0.8}Fe_{0.2}O_{3-\delta}$ oxides prepared by different methods under the same sintering profile were examined in terms of microstructure and oxygen permeation performance. The oxide powders were synthesized by solid-state reaction, modified citrate and citrate–EDTA complexing method. The membrane synthesized by the solid-state reaction method showed the highest oxygen permeability [12].

In 2005, Wang et al. characterized the high temperature phase structures of the perovskite-type oxide $Ba_{0.5}Sr_{0.5}Co_{0.8}Fe_{0.2}O_{3-\delta}$ *in situ* by high temperature X-ray diffraction. BSCF exhibits a good phase reversibility and structure stability in air from room temperature to 1000°C. The thermal expansion coefficient of BSCF was determined to be 11.5×10^{-6} $°C^{-1}$, which is smaller than that of $SrCo_{0.8}Fe_{0.2}O_{3-\delta}$ (17.9×10^{-6} $°C^{-1}$). The oxygen permeation flux increased considerably with the increase of the grain size of the membrane [13].

In 2006, Hae et al. prepared $Ba_{0.5}Sr_{0.5}Co_{0.8}Fe_{0.2}O_{3-\delta}$ and $La_{0.6}Ba_{0.4}Co_{0.2}Fe_{0.8}O_{3-\delta}$ (LBCF) by the combined citrate-EDTA method. The cathode performances of the BSCF and LBCF electrodes were sensitive to the conditions of powder preparation. The BSCF electrode prepared from the precursor solution with a pH value of 8 showed low polarization resistance and its area specific resistances (ASR) were 1.1, 0.15 and 0.035 cm^2 at 500, 600, and 700 ◦C,

respectively. On the other hand, the cathode polarization resistances of the LBCF electrode were slightly higher than those of the BSCF electrode [14].

Yang et al. synthesized $Ba_{0.5}Sr_{0.5}Co_{0.8}Fe_{0.1}M_{0.1}O_{3-\delta}$ (M = Cr, Mn, Zr) by solid-state reaction method. These materials possess purely cubic perovskite structure with the exception of $Ba_{0.5}Sr_{0.5}Co_{0.8}Fe_{0.1}M_{0.1}O_{3-\delta}$ (M = Mn, Zr), in which minor impurities exist. The oxygen permeation fluxes of the $Ba_{0.5}Sr_{0.5}Co_{0.8}Fe_{0.1}M_{0.1}O_{3-\delta}$ (M = Fe, Cr, Mn, Zr) membranes increased in the following order: Fe > Cr > Zr > Mn. The X-ray diffraction (XRD) and differential thermal analysis (DTA) experiments showed that the structural stability of BSCF could be significantly improved by partially substitution of Cr, Mn or Zr ion at Fe site of BSCF [15].

Cheng et al. investigated chemical compatibility of the $Ba_{0.5}Sr_{0.5}Co_{0.8}Fe_{0.2}O_{3-\delta}$ with the yttria-stabilized zirconia (YSZ) electrolyte or Gd-doped ceria electrolyte (GDC). The BSCF cathode was adopted for anode-supported YSZ electrolyte cells with and without the application of a 1 μm thick GDC buffering layer between the cathode and the YSZ electrolyte. The interfacial reactions of the BSCF with the YSZ electrolyte surface and the GDC coated YSZ surfaces were investigated. The results depicted a great improvement in cell performance and a significant decrease in polarization resistance after adding the GDC buffer layer. The optimum firing temperature of the GDC film onto the YSZ film was around 1250°C, which led to the maximum power density of 1.56 Wcm^{-2} at 800°C using air as oxidant and hydrogen as fuel [16].

In 2006, Li et al. revealed $(Ba_{0.5}Sr_{0.5})_{1-x}Sm_xCo_{0.8}Fe_{0.2}O_{3-\delta}$ (BSSCF; x = 0.05–0.15) compounds synthesized with EDTA-Pechini method. According to the XRD results, the main phase of the material belongs to the cubic perovskite-type, and the lattice contracting with the increasing contents of Sm^{3+}. The TEC of the compounds is 19.1–20.3x10^{-6} $°C^{-1}$ from 30 to 800 °C, which close to the values of $Ba_{0.5}Sr_{0.5}Co_{0.8}Fe_{0.2}O_{3-\delta}$. In addition, the conductivity of BSSCF is higher than that of BSCF; e.g., about 212% higher at 500 ◦C for the x = 0.15 compound. Electrochemical impedance spectra at intermediate temperature showed the better electrochemical performance of BSSCF than BSCF; e.g., the total resistance values of BSSCF electrode is 2.98 Ωcm^2 at 500 ◦C, nearly 50% lower than that of BSCF. Furthermore, they studied thermal properties of the materials by thermogravimetric

analysis (TGA). TGA results presented the loss of lattice oxygen during heating up and indicated that the diffusion coefficient D decreased with the increasing content of Sm in the sample. [17] In 2007, they demonstrated the cell performance measurements conducted on a Ni-SDC anode supported single cell using a SDC thin film as electrolyte, and $(Ba_{0.5}Sr_{0.5})_{0.9}Sm_{0.1}Co_{0.8}Fe_{0.2}O_{3-\delta}$ layer as cathode. The maximum power densities were 681mWcm^{-2} at 600°C and 820 mWcm^{-2} at 650 °C [18].

Wang et al. investigated that a composite cathode of BSCF containing 30 wt.% CGO (20 mol% Gd_2O_3-doped CeO_2) and a small quantity of Ag was prepared and studied, which shows the lowest area specific resistance (<0.1Ωcm^2 at temperatures higher than 700°C). The average TEC of pure BSCF in the temperature range of 30–850°C was 18.53x10^{-6} °C^{-1} (much higher than that of CGO), which could be reduced to 16.11K°C^{-1} by introduction of 30 wt.% CGO. The electrical conductivity of BSCF was all the same level (~43 S cm^{-1}) from 500 °C to 900 °C [19].

Peña-Martínez et al. tested an intermediate temperature solid oxide fuel cell containing of $La_{0.9}Sr_{0.1}Ga_{0.8}Mg_{0.2}O_{2.85}$ (LSGM) as electrolyte, $Ba_{0.5}Sr_{0.5}Co_{0.8}Fe_{0.2}O_{3-\delta}$ (BSCF) as cathode and $La_{0.75}Sr_{0.25}Cr_{0.5}Mn_{0.5}O_{3-\delta}$ (LSCM) as anode material. The maximum power density value of the BSCF/LSGM/LSCM cell with 1.5 mm thick electrolyte was 160 mWcm^{-2} at 1073 K, using moistened H_2 diluted with N_2 as fuel and air as oxidant [20].

Meng et al. showed a nickel-based anode-supported SOFC assembled with a 10 μm thick $Ce_{0.8}Sm_{0.2}O_{2-\delta}$ (SDC) electrolyte and a $Ba_{0.5}Sr_{0.5}Co_{0.8}Fe_{0.2}O_{3-\delta}$ cathode. The cell performance was investigated with hydrogen and ammonia gas evaporated from liquefied ammonia as fuel. Fueled by hydrogen, the maximum power densities were 1872, 1357, and 748 mWcm^{-2} at 650, 600, and 550 °C, respectively. With ammonia as fuel, the cell showed the maximum power densities of 1190, 434, and 167 mWcm^{-2}, respectively. The results demonstrated that the ammonia was a right convenient liquid fuel for SOFCs as long as it was keeping the decomposition completion of ammonia in the cell or before entering the cell [21].

In 2007, Mohammadi et al. reported $Ba_{0.5}Sr_{0.5}Co_{0.8}Fe_{0.2}O_{3-\delta}$ oxides prepared at different shaping and sintering parameters under the same powder

synthesis method. The oxide powders were synthesized using citrate–EDTA complexing method. The result showed that the best sintering dwell time is about 8–9 hours and after that time there is no change in membrane characteristics. Moreover, the best sintering temperature and the best pressure for pressing of the samples was 1,100°C and 2,000-2,500 bar, respectively [22].

Subramania et al. successfully synthesized Nano-crystalline $Ba_{0.5}Sr_{0.5}Co_{0.8}Fe_{0.2}O_{3-\delta}$ powder by a novel sol–gel thermolysis method using a unique combination of PVA and urea. X-ray diffraction patterns showed a cubic perovskite $Ba_{0.5}Sr_{0.5}Co_{0.8}Fe_{0.2}O_{3-\delta}$ formed by calcining the precursor at 450 ◦C for 5 h. But the well-crystalline cubic perovskite $Ba_{0.5}Sr_{0.5}Co_{0.8}Fe_{0.2}O_{3-\delta}$ can be obtained by calcining the precursor at 650 °C for 5 h. Thermogravimetric (TG) result showed the lattice oxygen loss of the product was about ~2% in its original weight in the temperature range 40–900 °C. In addition, the maximum electrical conductivity of 32 S cm^{-1} was obtained in air at 500 °C, which is higher than the reported value [23].

Bos˘kovic´ et al. showed the nanopowders of $Ba_{0.5}Sr_{0.5}Co_{0.8}Fe_{0.2}O_{3-\delta}$ with perovskite type crystal structure synthesized by modified glycine nitrate procedure. Modification of the procedure was performed by partial replacement of nitrates by acetates, in order to control the burn-up reaction. The obtained nanopowders, according to XRD results are single phase, independent of number of dopants [24].

Shao et al. also investigated the influence of iron doping level in $Ba_{0.5}Sr_{0.5}Co_{1-y}Fe_yO_{3-\delta}$ (y = 0.0–1.0) oxides on their phase structure, oxygen nonstoichiometry, electrical conductivity, performance as symmetrical cell electrode and oxygen permeating membranes. A cubic perovskite structure was observed for all the compositions with the presence of iron. The increase of iron doping level resulted in the decrease of the lattice constant, room-temperature oxygen nonstoichiometry, total electrical conductivity, and the increase of area specific resistance (ASR) as cathode with samaria doped ceria electrolyte. However, promising cathode performance with an ASR as low as 0.613 Ωcm^2 was still obtained at 600 ◦C for $Ba_{0.5}Sr_{0.5}FeO_{3-\delta}$ (BSF). Moreover, the increase of iron doping level resulted in the decrease of oxygen permeation flux from J_{O2} = 2.28 μmol cm^{-2} s^{-1} (STP) for $Ba_{0.5}Sr_{0.5}Co_{0.8}Fe_{0.2}O_{3-\delta}$ to ~0.45 μmol cm^{-2} s^{-1} (STP) at 900 ◦C for BSF (y = 1.0) [25].

Kammer reported the iron–cobalt based perovskite cathodes with different A-site cations ($(Ln_{0.6}Sr_{0.4})_{0.99}Fe_{0.8}Co_{0.2}O_{3-\delta}$, where Ln is La, Pr, Sm or Gd). The La-containing perovskite was hexagonal but the Pr and Sm perovskites were orthorhombic. The gadolinium-based perovskite was a two phase system consisting of an orthorhombic and a cubic perovskite phase. The thermal expansion coefficient (TEC) increased systematically with a decrease in the size of the A-site cation until the gadolinium-containing perovskite where the TEC decreases abruptly. The total electrical conductivity was the highest for the La-based perovskite and the lowest for the Gd-based perovskite [26].

Recently, many researchers are looking for new cathode materials for IT-SOFC. $Ba_{0.5}Sr_{0.5}Co_{0.8}Fe_{0.2}O_{3-\delta}$ is a good candidate for cathode material for IT-SOFC because of its mixed conductivity but it is not as good as the other cathodes (e.g. $La_{0.6}Sr_{0.4}Co_{0.2}Fe_{0.8}O_{3-\delta}$) Moreover, the high operating temperature makes the application of SOFC be limited. In this case, a decrease in operation temperature is needed. Cathode is an important component of SOFC, so developing a new cathode material with well performance at intermediate temperature is the key to decrease the operating temperature [5]. Therefore, this research is focused to improve electrical conductivity by doping $Ba_{0.5}Sr_{0.5}Co_{0.8}Fe_{0.2}O_{3-\delta}$ with various metals at both A and B sites.

1.6 The objectives of the thesis

1. To synthesize $Ba_{0.5}Sr_{0.5}Co_{0.8}Fe_{0.2-x}M_xO_{3-\delta}$, $Ba_{0.5}Sr_{0.5}Co_{0.8-x}Fe_{0.2}M_xO_{3-\delta}$, $(Ba_{0.5}Sr_{0.5})_{1-x}P_xCo_{0.8}Fe_{0.2}O_{3-\delta}$, $(Ba_{0.5}Sr_{0.5})_{1-x}P_xCo_{0.8-y}Fe_{0.2}M_yO_{3-\delta}$, and $(Ba_{0.5}Sr_{0.5})_{1-x}P_xCo_{0.8}Fe_{0.2-y}M_yO_{3-\delta}$ (x = 0.05,0.1) ; (y = 0.05,0.1) ; (M = Mg,Ni,Zn,Cu) ; and (P = La,Pr)
2. To characterize and measure electrical conductivity of doped $Ba_{0.5}Sr_{0.5}Co_{0.8}Fe_{0.2}O_{3-\delta}$ perovskites

1.7 The scope of the thesis

1. Synthesize and characterize the single-phase perovskite oxides
2. Study the effects of doping metal ions on $Ba_{0.5}Sr_{0.5}Co_{0.8}Fe_{0.2}O_{3-\delta}$, such as the change of lattice parameter and oxygen deficiency

3. Determine electrical conductivity by four DC probe technique and oxygen permeation by O_2-TPD

CHAPTER II

EXPERIMENTAL

The synthesis and characterization procedure of perovskite oxide are described as below:

2.1 Chemicals

The chemicals listed in Table 2.1, were used without further purification.

Table 2.1 Reagents for synthesis of perovskites

Reagents	Formula Weight	Purity%	Company
$Ba(NO_3)_2$	261.53	99.0	Fluka
$Sr(NO_3)_2$	211.63	99.0	Fluka
$Fe(NO_3)_3 \cdot 9H_2O$	404.00	98.0	Riedel-deHaën
$Co(NO_3)_2 \cdot 6H_2O$	291.03	98.0	Fluka
$Mg(NO_3)_2.6H_2O$	256.41	99.0	Fluka
$Ni(NO_3)_2.6H_2O$	290.79	98.0	Wako
$Zn(NO_3)_{2.6}H_2O$	297.48	99.0	Fluka
$Cu(NO_3)_2.6H_2O$	241.60	99.0	Fluka
$Pr(NO_3)_3.6H_2O$	435.01	99.9	Mitsuwas
$La(NO_3)_3.6H_2O$	433.01	99.0	Fluka
$C_6H_8O_7$	192.13	99.5	Riedel-deHaën
HNO_3	63.01	65	Merck
NH_3H_2O	35.05	25	Merck
C_2H_5OH	46.07	30	Merck

2.2 Synthesis of perovskite powder by modified citrate method

All components in Table 2.2 were synthesized in basic solution.

Table 2.2 The components of all samples

Doped	Replaced	components	Abbreviation
-	-	$Ba_{0.5}Sr_{0.5}Co_{0.8}Fe_{0.2}O_{3-\delta}$	BSCF
0.05mole in B site	Fe	$Ba_{0.5}Sr_{0.5}Co_{0.8}Fe_{0.15}Mg_{0.05}O_{3-\delta}$	FeMg 0.05
		$Ba_{0.5}Sr_{0.5}Co_{0.8}Fe_{0.15}Ni_{0.05}O_{3-\delta}$	FeNi 0.05
		$Ba_{0.5}Sr_{0.5}Co_{0.8}Fe_{0.15}Zn_{0.05}O_{3-\delta}$	FeZn 0.05
		$Ba_{0.5}Sr_{0.5}Co_{0.8}Fe_{0.15}Cu_{0.05}O_{3-\delta}$	FeCu 0.05
	Co	$Ba_{0.5}Sr_{0.5}Co_{0.75}Fe_{0.2}Mg_{0.05}O_{3-\delta}$	CoMg 0.05
		$Ba_{0.5}Sr_{0.5}Co_{0.75}Fe_{0.2}Ni_{0.05}O_{3-\delta}$	CoNi 0.05
		$Ba_{0.5}Sr_{0.5}Co_{0.75}Fe_{0.2}Zn_{0.05}O_{3-\delta}$	CoZn 0.05
		$Ba_{0.5}Sr_{0.5}Co_{0.75}Fe_{0.2}Cu_{0.05}O_{3-\delta}$	CoCu 0.05
0.05 mole in A site	Ba and Sr	$(Ba_{0.5}Sr_{0.5})_{0.95}Pr_{0.05}Co_{0.8}Fe_{0.2}O_{3-\delta}$	Pr 0.05
		$(Ba_{0.5}Sr_{0.5})_{0.95}La_{0.05}Co_{0.8}Fe_{0.2}O_{3-\delta}$	La 0.05
0.1 mole in B site	Fe	$Ba_{0.5}Sr_{0.5}Co_{0.8}Fe_{0.1}Mg_{0.1}O_{3-\delta}$	FeMg 0.1
		$Ba_{0.5}Sr_{0.5}Co_{0.8}Fe_{0.1}Ni_{0.1}O_{3-\delta}$	FeNi 0.1
		$Ba_{0.5}Sr_{0.5}Co_{0.8}Fe_{0.1}Zn_{0.1}O_{3-\delta}$	FeZn 0.1
		$Ba_{0.5}Sr_{0.5}Co_{0.8}Fe_{0.1}Cu_{0.1}O_{3-\delta}$	FeCu 0.1
	Co	$Ba_{0.5}Sr_{0.5}Co_{0.7}Fe_{0.2}Mg_{0.1}O_{3-\delta}$	CoMg 0.1
		$Ba_{0.5}Sr_{0.5}Co_{0.7}Fe_{0.2}Ni_{0.1}O_{3-\delta}$	CoNi 0.1
		$Ba_{0.5}Sr_{0.5}Co_{0.7}Fe_{0.2}Zn_{0.1}O_{3-\delta}$	CoZn 0.1
		$Ba_{0.5}Sr_{0.5}Co_{0.7}Fe_{0.2}Cu_{0.1}O_{3-\delta}$	CoCu 0.1
0.1 mole in A site	Ba and Sr	$(Ba_{0.5}Sr_{0.5})_{0.9}Pr_{0.1}Co_{0.8}Fe_{0.2}O_{3-\delta}$	Pr 0.1
		$(Ba_{0.5}Sr_{0.5})_{0.9}La_{0.1}Co_{0.8}Fe_{0.2}O_{3-\delta}$	La 0.1
0.15 mole in A site	Ba and Sr	$(Ba_{0.5}Sr_{0.5})_{0.85}Pr_{0.15}Co_{0.8}Fe_{0.2}O_{3-\delta}$	Pr 0.15
		$(Ba_{0.5}Sr_{0.5})_{0.85}La_{0.15}Co_{0.8}Fe_{0.2}O_{3-\delta}$	La 0.15
0.2 mole in A site	Ba and Sr	$(Ba_{0.5}Sr_{0.5})_{0.8}Pr_{02}Co_{0.8}Fe_{0.2}O_{3-\delta}$	Pr 0.2
		$(Ba_{0.5}Sr_{0.5})_{0.8}La_{0.2}Co_{0.8}Fe_{0.2}O_{3-\delta}$	La 0.2
A & B site		$(Ba_{0.5}Sr_{0.5})_{0.8}Pr_{0.2}Co_{0.8}Fe_{0.15}Cu_{0.05}O_{3-\delta}$	Pr0.2FeCu0.05
		$(Ba_{0.5}Sr_{0.5})_{0.8}La_{0.2}Co_{0.8}Fe_{0.15}Cu_{0.05}O_{3-\delta}$	La0.2FeCu0.05

The perovskite oxide powder was synthesized by modified citrate method. The salts of $Ba(NO_3)_2$, $Sr(NO_3)_2$, $Co(NO_3)_2.6\ H_2O$, $Fe(NO_3)_3.9H_2O$, $Mg(NO_3)_2.6H_2O$, $Ni(NO_3)_2.6H_2O$, $Zn(NO_3)_2.6H_2O$, $Cu(NO_3)_2.3H_2O$, $Pr(NO_3)_3.6H_2O$, and $La(NO_3)_3.6H_2O$ at the desired molar ratio (based on perovskite powder 0.02 mol) were dissolved in 10 mL of ultra pure nitric acid (70%) and stirred for 6 hours. The amount of citric acid was added with two times of total metal ions. After stirred for 24 hours, the pH of the mixture was adjusted to 8-9 by ammonia solution (25%) to obtain brown solution and heated to 200-250°C. The spontaneous combustion occurred and the brown-black powder appeared. The powder was calcined at 900-1000°C for 5 hours, depending on the composition. The condition of calcination was shown in scheme 2.1.

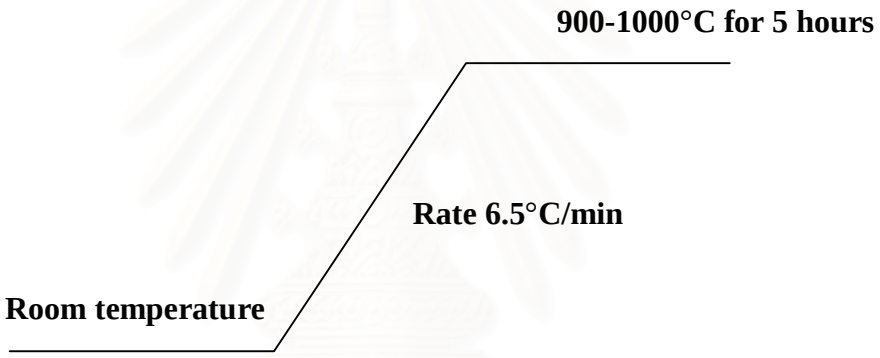

Scheme 2.1 The condition of calcination for perovskite oxide**.**

Then, the calcined powder was milled in ethanol by mortar, pressed with 1-3 ton and sintered at 1000-1100°C depending on the composition to obtain perovskite disk. The condition of sintering of perovskite disk was exhibited in scheme 2.2.

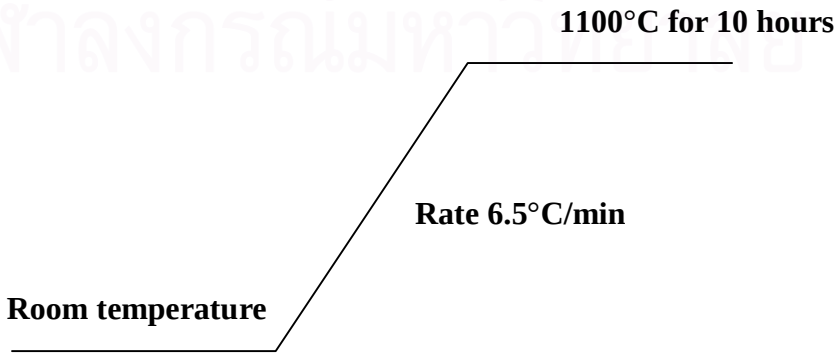

Scheme 2.2 The condition of sintering process for perovskite oxide**.**

2.3 Characterization of the perovskite oxides

2.3.1 X-ray diffractrometry (XRD)

The crystal structure of perovskite oxides was determined by using Rigaku, DMAX 2002 Ultima Plus X-Ray powder diffractometer equipped with a monochromator and a Cu-target X-ray tube (40 kV, 30 mA) and angles of 2θ ranged from 20-70 degree (step time 0.5 s., scan step 0.020^{o}) at Department of Chemistry, Faculty of Science, Chulalongkorn University. Perovskite were characterized after the calcination steps by XRD.

2.3.2 Scanning electron microscopy (SEM)

The morphology of the disks was carried out using a JEOL JSM-5800LV scanning electron microscopy, Oxford Instrument (Link ISIS series 300) at Faculty of Science, Chulalongkorn University. This instrument uses X-rays or electrons scattered back from the surface "illuminated" by a restored electron beam to generate an image with remarkable three-dimensional qualities.

2.3.3 Temperature-programmed desorption (TPD)

The perovskite capabilities of adsorbing O_2 were measured using temperature-programmed desorption (TPD, model Thermo Finnigan/TPDRO 1100), at Department of Chemistry, Faculty of Science, Chulalongkorn University.

The perovskite powder was first pretreated in He atmosphere (30 ml/min) at 500°C for 0.5 hours, then cooled to 100°C, after which adsorption of gas was performed in a flow of O_2 (5.29% balanced by He) for 40 min. The powder was maintained at 100°C in He flow for another 0.5 hours to eliminate physically adsorbed O_2. Thereafter, the TPD was conducted by heating the sample to 800°C at a rate 20°C/min. The desorbed O_2 was analyzed using gas chromatograph with a thermal conductivity detector (TCD).

2.3.4 Electrical conductivity Measurement

The electrical conductivity of perovskite oxide was investigated by DC-4 probe technique. All of disc samples (after sintered at 1100°C for 10 h) were cut to bar (about 12 mm in length, 5 mm in width and 1.5 mm in thickness). Four Pt wires were wrapped around each bar and bonded to the sample using Pt paste. The samples were heated to 950°C for 10 min with the heating rate of 5°C/min to sinter the conducting paste. The conductivity measurements were performed in a tube furnace with an alumina tube using Pt wires to connect the wires on the sample in the hot zone. These wires were then fed through the end cap of the tube. Four-point DC electrical conductivity measurements were performed by sending a current (0.1 to 200 mA) through the wires at the ends of the sample and then measuring the voltage drop across and two middle wires. The electrical conductivity measurement from room temperature to 800°C were collected by potentiostat/galvanostat (Autolab PG100).

2.3.5 Dilatometer

The disc samples (after sintered at 1100°C for 10 h) were cut to bar (about 12 mm in length, 5 mm in width and 1.5 mm in thickness). The thermal expansion coefficients were measured from room temperature to 800°C in air with a heating rate of 10 K/min by dilatometer (NETZSCH DIL 402C) from Department of Materials Science, Faculty of Science, Chulalongkorn University.

CHAPTER III

RESULTS AND DISCUSSIONS

In this research, synthesized perovskite compounds ($Ba_{0.5}Sr_{0.5}Co_{0.8}Fe_{0.2}O_{3-\delta}$) were doped with different contents of metal ions in either A site (Ba, Sr) or B site (Co, Fe). Therefore, using abbreviation is convenient to describe the composition of these compounds. For example, $Ba_{0.5}Sr_{0.5}Co_{0.8}Fe_{0.2}O_{3-\delta}$ is abbreviated to be BSCF. For B site, $Ba_{0.5}Sr_{0.5}Co_{0.8}Fe_{0.15}Mg_{0.05}O_{3-\delta}$ is abbreviated to be FeMg 0.05. It means Fe site in $Ba_{0.5}Sr_{0.5}Co_{0.8}Fe_{0.2}O_{3-\delta}$ is partially substituted by Mg 0.05 mol.

3.1 Synthesis of perovskite oxide by modified citrate method

The perovskite oxides were prepared by modified citrate method with the mole ratio of metal nitrate to citric acid, 1:2. The metal nitrates were dissolved in 70% nitric acid, which then reacted with citric acid to form metal-citrate-nitrate complexes. These metal-citrate complexes can undergo polymerization when ammonia solution was added. Meanwhile, $NH_3 \cdot H_2O$ was added, the white fume of NH_4NO_3 was suddenly observed, which came from the free NO_3^- reacting with $NH_3 \cdot H_2O$ and generated heat. The solution was the metal citrate-nitrate gel resulting from the polymerization of the metal citrate-nitrate complex when liquid NH_3 was added. Then, the solution changed from clear red brown to clear deep brown solution (pH ≈ 9).

The combustion of the metal citrate-nitrate gel solution was composed of three steps, evaporation, decomposition, and spontaneous combustion. The excess solvent was firstly evaporated until a sticky gel was obtained. During the final stage of evaporation, the mixture began to swell, and became viscous. The generated gases can be observed from the large swelling viscous mass. Finally, at around 250°C the spontaneous combustion was initiated to convert the mixture into the powder. A typical burning of 40 ml of gel solution was completed within 20-30 seconds.

The precursor powder obtained by combustion reaction was calcined at 1,000°C for 5 hours in order to achieve pure phase and remove residual organic

compound. The calcined powder was ground and pressed to make a disc. Then, all sample discs were sintered in air at 1,100°C for 10 hours. The disc membranes have relative density higher than 90%.

3.2 Effect of A and B–sites doping on formation of BSCF

3.2.1 Effect of B site doping on the structure and morphology of BSCF

The perovskite structure was known to be stable only for $0.75 \leq t \leq 1.1$ and was cubic in the range $t > 0.95$. As shown in Table 3.1, the tolerance numbers of BSCF doping at B site was close to 1. It is confirmed that structures of the samples were cubic perovskite–type. The metals with different sizes (Mg, Ni, Zn, Cu) doped at Fe or Co site had no effect on the tolerance numbers. Even though the content of metals increased, the numbers were still in the range 1.05-1.06.

Table 3.1 The tolerance numbers of B-site doping on BSCF

Compounds	Tolerance No.	Compounds	Tolerance No.
BSCF	1.07	FeZn 0.05	1.06
FeMg 0.05	1.06	FeZn 0.1	1.06
FeMg 0.1	1.06	CoZn 0.05	1.06
CoMg 0.05	1.06	CoZn 0.1	1.05
CoMg 0.1	1.06	FeCu 0.05	1.06
FeNi 0.05	1.06	FeCu 0.1	1.06
FeNi 0.1	1.06	CoCu0.05	1.06
CoNi 0.05	1.06	CoCu 0.1	1.05
CoNi 0.1	1.06		

3.2.1.1 Mg–doped BSCF

A) XRD results

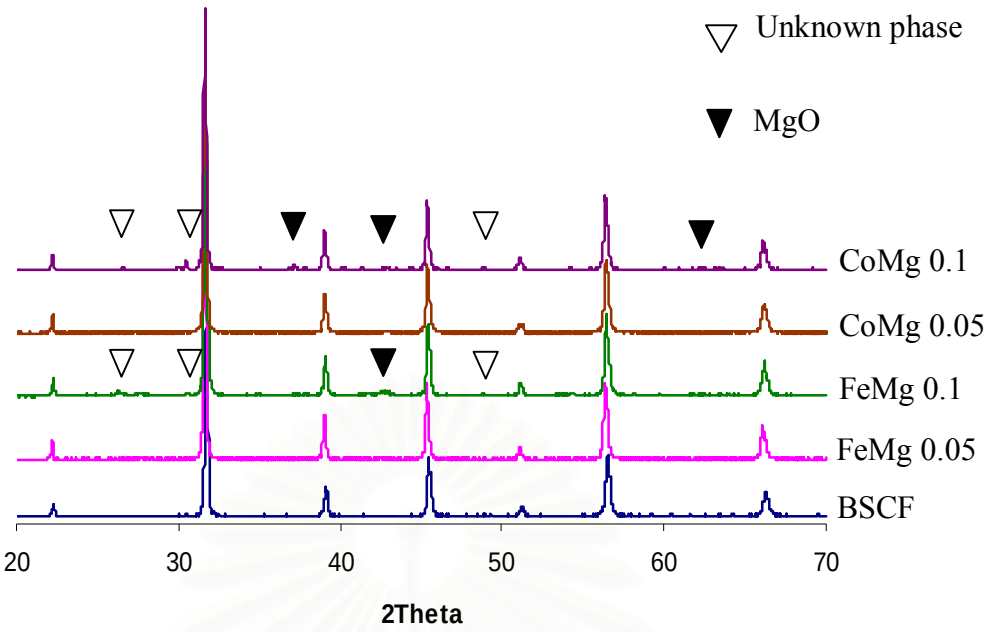

Figure 3.1 The XRD patterns of $Ba_{0.5}Sr_{0.5}Co_{0.8}Fe_{0.2-x}Mg_xO_{3-\delta}$ and $Ba_{0.5}Sr_{0.5}Co_{0.8-x}Fe_{0.2}Mg_xO_{3-\delta}$ (x = 0, 0.05 and 0.1) after calcined at 1000°C for 5 hours

The XRD pattern of BSCF showed the single phase of perovskite oxide and cubic structure with a space group P432 (Figure 3.1). From this Figure, the miller indexes were 100, 110, 111, 200, 210, 211 and 220 at 2θ = 22.3°, 31.8°, 39.2°, 45.6°, 51.3°, 56.6°, 66.4°, respectively. In addition, the lattice parameter calculated by Jade software is 3.9848 A°

Figure 3.1 shows the XRD patterns of $Ba_{0.5}Sr_{0.5}Co_{0.8}Fe_{0.2-x}Mg_xO_{3-\delta}$ and $Ba_{0.5}Sr_{0.5}Co_{0.8-x}Fe_{0.2}Mg_xO_{3-\delta}$. The XRD results indicated that Fe and Co replaced by Mg 0.05 mol showed single phase and a cubic structure but doping Mg 0.1 mol at Fe and Co had the impurity phase. It was observed that XRD peaks of Mg–doped oxides did not shift as compared to undoped BSCF. From Table 3.2, the lattice parameters of Mg replaced Fe and Co slightly increased because the ionic radius of Mg^{2+} (0.86A°) was larger than Fe^{4+} (0.725A°) and Co^{4+} (0.67A°). However, the lattice parameter of doped BSCF did not increase significantly with the increasing content of Mg. It was suggested that 0.05 mol of Mg can replace partially into Co and Fe without any change of the BSCF structure and lattice parameters. Upon increasing the content of Mg, the secondary phase was observed in XRD. It can be explained that the addition of 0.1 mol of Mg to replace Co and Fe can cause the formation of MgO (JCPDS 4–829) and unidentified impurity phases.

Table 3.2 The lattice parameters of $Ba_{0.5}Sr_{0.5}Co_{0.8-x}Fe_{0.2}Mg_xO_{3-\delta}$ and $Ba_{0.5}Sr_{0.5}Co_{0.8-x}Fe_{0.2}Mg_xO_{3-\delta}$ (x = 0, 0.05 and 0.1) after calcined at 1000°C for 5 hours

Sample	Lattice parameter (A°)
BSCF	3.9848
FeMg0.05	3.9939
FeMg0.1	3.9986
CoMg0.05	3.9890
CoMg0.1	3.9950

B) SEM images

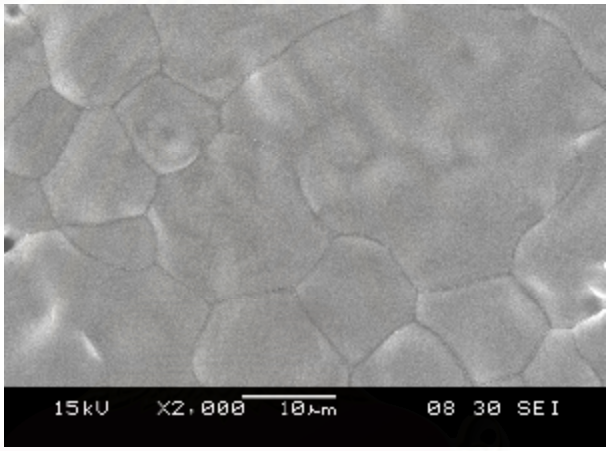

Figure 3.2 SEM micrograph of $Ba_{0.5}Sr_{0.5}Co_{0.8}Fe_{0.2}O_{3-\delta}$ sintered at 1,100°C for 10 hours.

SEM picture of BSCF shows the dense morphology without any impurity phase on the surface which is consistent with the XRD results. The grain size varied in the range 10 to 40 μm.

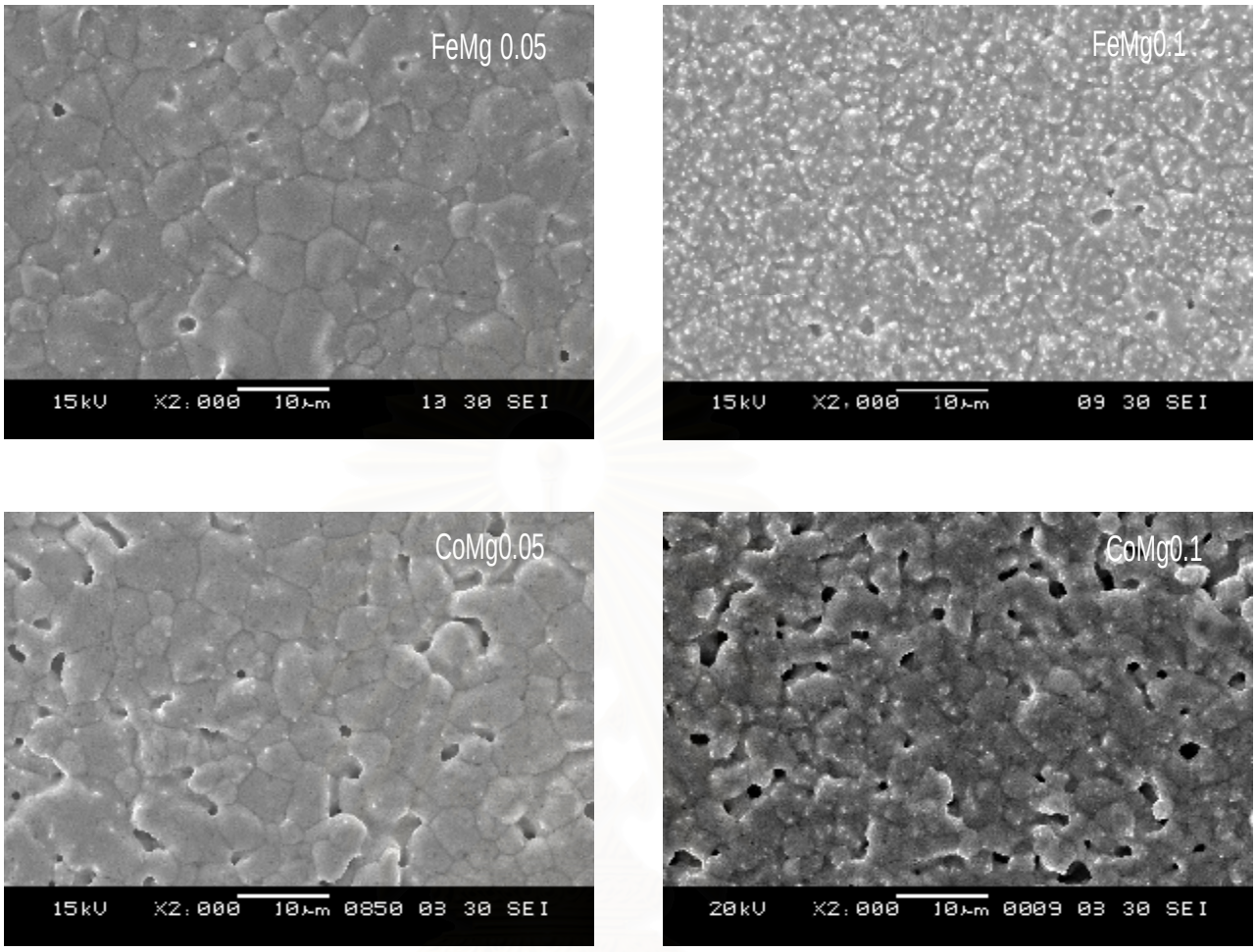

Figure 3.3 SEM micrographs of $Ba_{0.5}Sr_{0.5}Co_{0.8}Fe_{0.2-x}Mg_xO_{3-\delta}$ and $Ba_{0.5}Sr_{0.5}Co_{0.8-x}Fe_{0.2}Mg_xO_{3-\delta}$ (x = 0.05 and 0.1) after sintered at 1,100°C for 10 hours

Figure 3.3 shows the morphologies of samples doping with Mg at Fe and Co. The results showed a lot of white dots (impurity phase) scattered on the surface. XRD patterns of both FeMg0.05 and CoMg0.05 showed single phase which do not agree with SEM results. It is possible that the amount of impurity phase is small so it does not appear in XRD patterns. XRD and SEM results of FeMg0.1 and CoMg0.1 showed impurity phase. It is seen that the amount of impurity phase increased with the increasing in Mg contents. The grain size of Mg specimens varied in the range 3 to 12 µm. Moreover, it was noticed that the microstructure of the high Co containing compositions (FeMg0.05 and FeMg0.1) had low porosity in comparison with the low Co containing compositions (CoMg0.05 and CoMg0.1). These results were consistent with previous research by Lv [27]. Mg ion can not fit in BSCF structure according to

XRD and SEM results. It is suggested that the state of Mg (+2) was lower than Co and Fe (+3 or +4), then a lot of oxygen had to escaped from the crystal lattice to neutralize the charge. It will cause the structure of doped BSCF to collapse. Therefore, MgO and unidentified oxide were formed as secondary phase to maintain the stability of the compound.

3.2.1.2 Ni–doped BSCF

A) XRD results

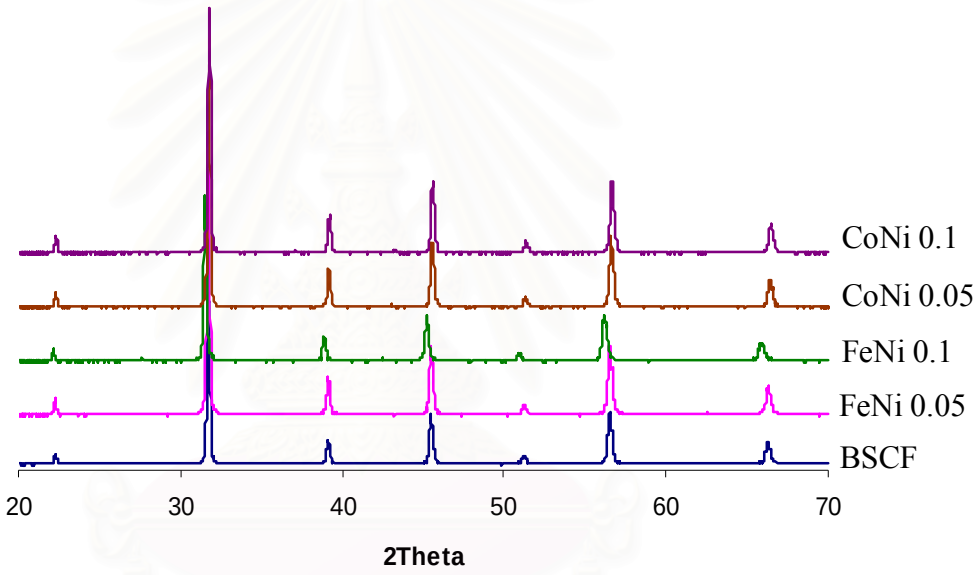

Figure 3.4 The XRD patterns of $Ba_{0.5}Sr_{0.5}Co_{0.8}Fe_{0.2-x}Ni_xO_{3-\delta}$ and $Ba_{0.5}Sr_{0.5}Co_{0.8-x}Fe_{0.2}Ni_xO_{3-\delta}$ (x = 0, 0.05 and 0.1) after calcined at 1000°C for 5 hours

Figure 3.4 shows the XRD patterns of $Ba_{0.5}Sr_{0.5}Co_{0.8}Fe_{0.2-x}Ni_xO_{3-\delta}$ and $Ba_{0.5}Sr_{0.5}Co_{0.8-x}Fe_{0.2}Ni_xO_{3-\delta}$ with x = 0.05 and 0.1 mol. It demonstrated that all samples doping with Ni^{2+} in the B sites of $Ba_{0.5}Sr_{0.5}Co_{0.8}Fe_{0.2}O_{3-\delta}$ have no any impurity phase and the structures are cubic. The XRD patterns of doped Ni^{2+} specimens are slightly shifted to the lower angle compared with BSCF. Although ionic radius of Ni^{2+} (0.83°A) is larger than Co^{4+} (0.67°A) and Fe^{4+} (0.725°A), the lattice parameters of doping Ni in the B site of BSCF are not different from BSCF.

Table 3.3 The lattice parameters of $Ba_{0.5}Sr_{0.5}Co_{0.8}Fe_{0.2-x}Ni_xO_{3-\delta}$ and $Ba_{0.5}Sr_{0.5}Co_{0.8-x}Fe_{0.2}Ni_xO_{3-\delta}$ (x = 0, 0.05 and 0.1) after calcined at 1000°C for 5 hours

Sample	Lattice parameter (A°)
BSCF	3.9848
FeNi0.05	3.9828
FeNi0.1	3.9968
CoNi0.05	3.9817
CoNi0.1	3.9811

B) SEM images

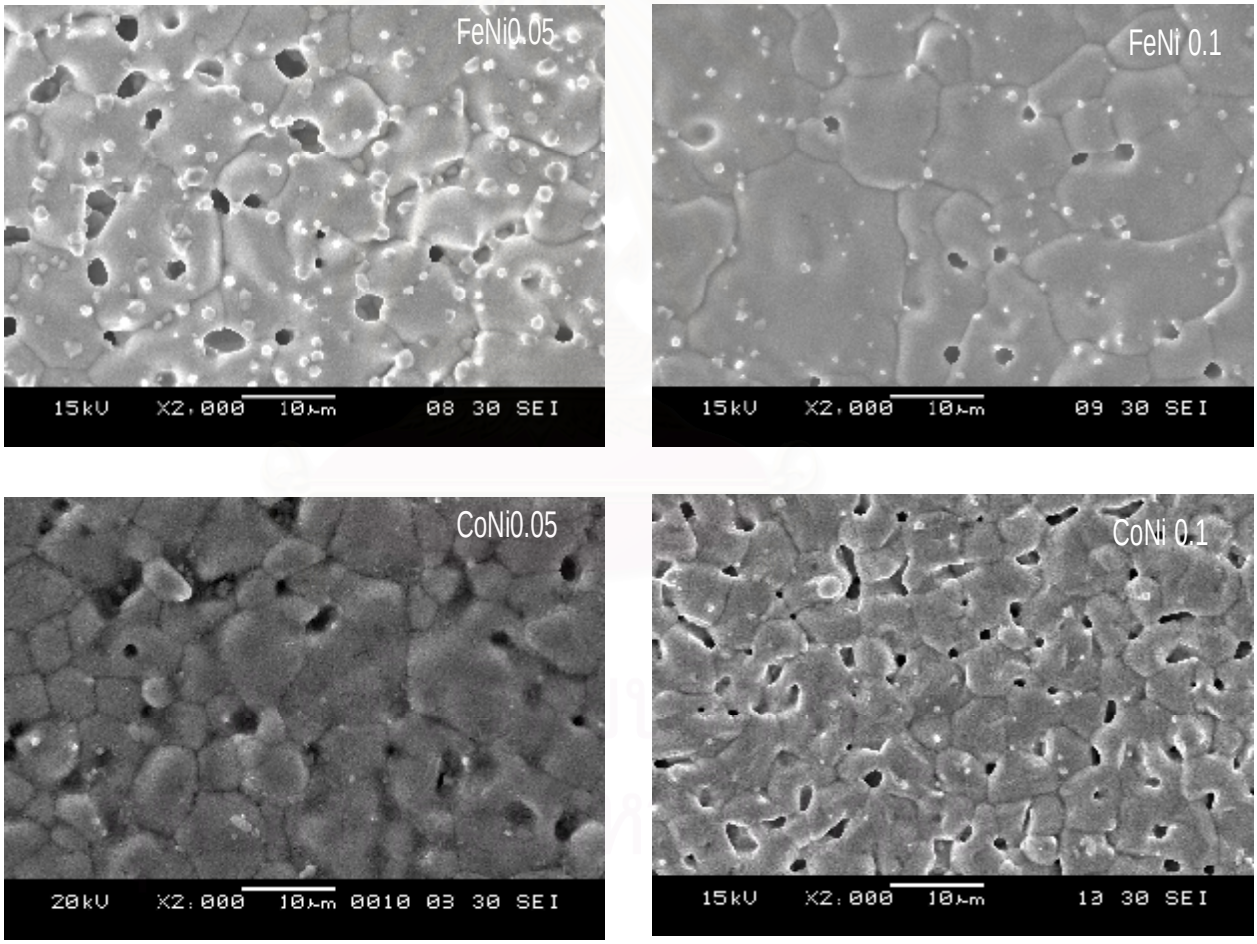

Figure 3.5 SEM micrograph of $Ba_{0.5}Sr_{0.5}Co_{0.8}Fe_{0.2-x}Ni_xO_{3-\delta}$ and $Ba_{0.5}Sr_{0.5}Co_{0.8-x}Fe_{0.2}Ni_xO_{3-\delta}$ (x = 0.05 and 0.1) after sintered at 1,100°C for 10 hours

The morphologies of BSCF doping with Ni at Fe and Co were presented in Figure 3.5. As the results, all of specimens had impurity on the surface and a lot of pore. The SEM micrographs of Ni doped BSCF were inconsistent with XRD patterns which showed single phase. SEM results showed that Ni^{2+} can not be doped in the structure of BSCF. The grain size of Ni^{2+} specimens varied in the range 3 to 12 μm.

It is expected that Ni can not be in the structure of BSCF. Moreover, it is confirmed by SEM results that there were a lot of impurity on the surface of the specimens disk. Generally, the impurity phase should appear in XRD patterns.

3.2.1.3 Zn–doped BSCF

A) XRD results

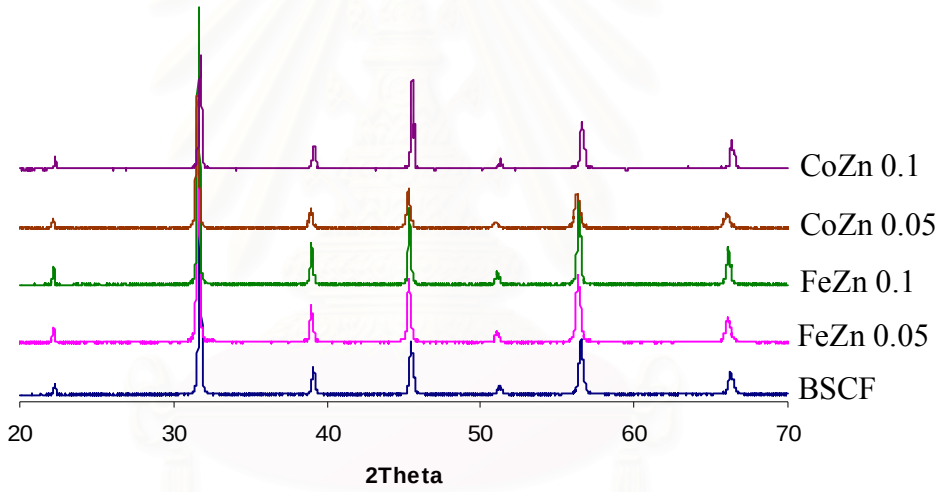

Figure 3.6 The XRD patterns of $Ba_{0.5}Sr_{0.5}Co_{0.8}Fe_{0.2-x}Zn_xO_{3-\delta}$ and $Ba_{0.5}Sr_{0.5}Co_{0.8-x}Fe_{0.2}Zn_xO_{3-\delta}$ (x = 0, 0.05 and 0.1) after calcined at 1000°C for 5 hours

In Figure 3.6, the structures of perovskite doped by Zn at B sites of BSCF are single phase with cubic perovskite structure. In addition, the XRD peaks slightly shifted to the lower angle compared with BSCF. This shift is considered to be the result from the expansion of crystal lattice caused by the bigger ionic radius. From Table 3.4, the lattice parameters of BSCF doping with Zn at B were more than that of BSCF because ionic radius of Zn^{2+} (0.88A°) is larger than Fe^{4+} (0.75A°) and Co^{4+} (0.67A°). The oxidation state of Zn does not change but Zn can be placed in the perovskite structure.

Table 3.4 The lattice parameters of $Ba_{0.5}Sr_{0.5}Co_{0.8}Fe_{0.2-x}Zn_xO_{3-\delta}$ and $Ba_{0.5}Sr_{0.5}Co_{0.8-x}Fe_{0.2}Zn_xO_{3-\delta}$ (x = 0, 0.05 and 0.1) after calcined at 1000°C for 5 hours

Sample	Lattice parameter (A°)
BSCF	3.9848
FeZn0.05	3.9975
FeZn0.1	4.0029
CoZn0.05	3.9950
CoZn0.1	3.9933

B) SEM images

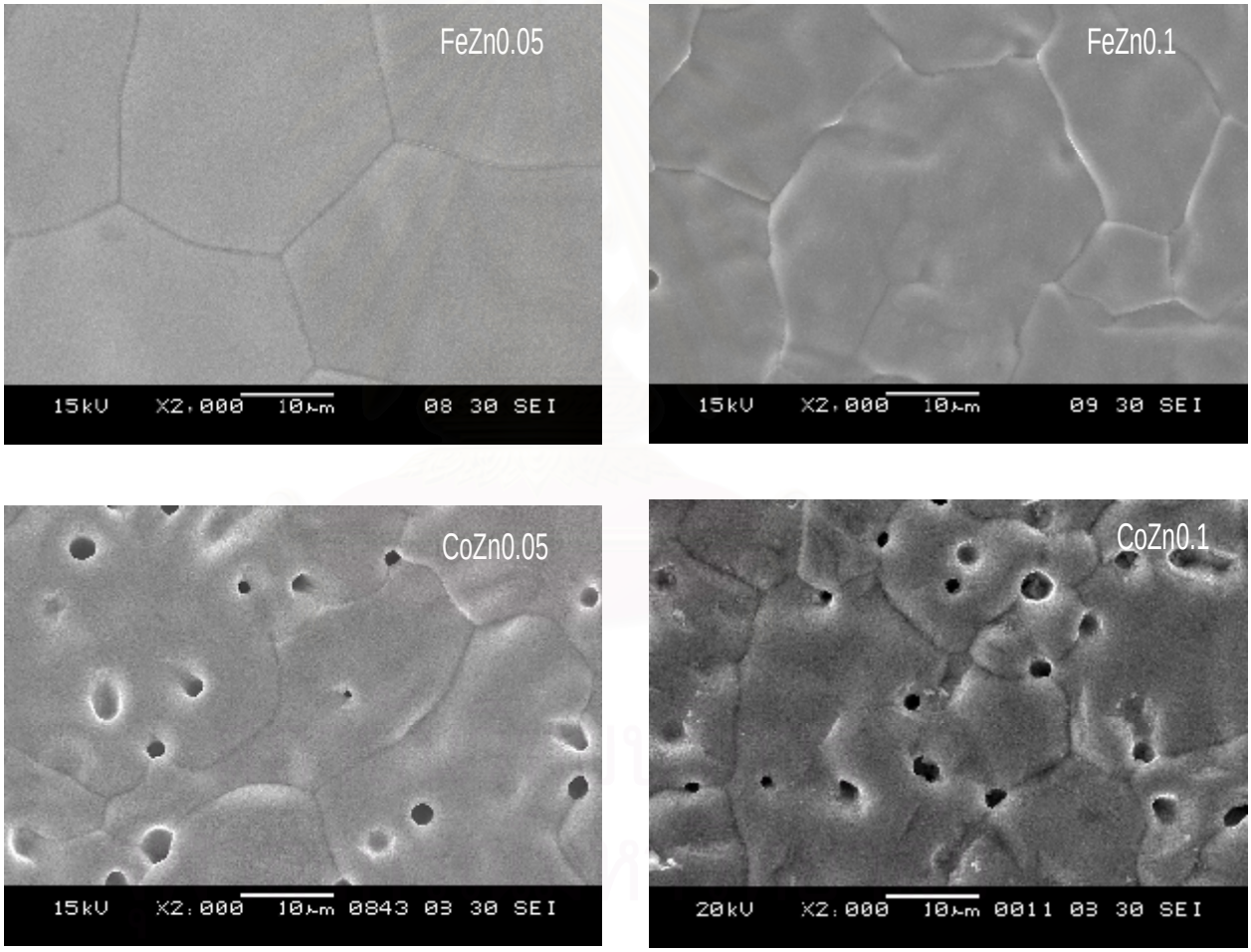

Figure 3.7 SEM micrographs of $Ba_{0.5}Sr_{0.5}Co_{0.8}Fe_{0.2-x}Zn_xO_{3-\delta}$ and $Ba_{0.5}Sr_{0.5}Co_{0.8-x}Fe_{0.2}Zn_xO_{3-\delta}$ (x = 0.05 and 0.1) after sintered at 1,100°C

SEM pictures of Zn–doped BSCF show dense and homogeneous surface (Figure 3.7). It is shown that the porosity of FeZn0.05 and FeZn0.1 were less than that of CoZn0.05 and CoZn0.1. The grain size were in the range 26 to 40 μm.

3.2.1.4 Cu–doped BSCF

A) XRD results

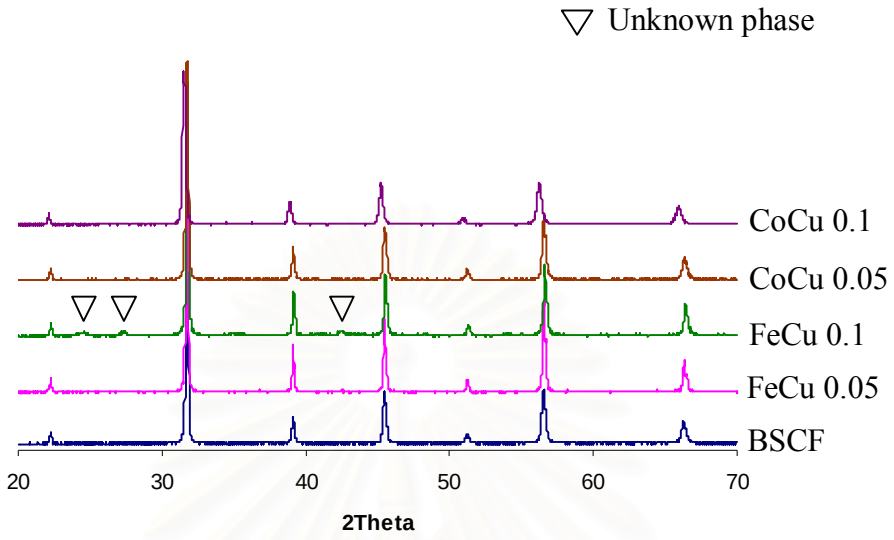

Figure 3.8 The XRD patterns of $Ba_{0.5}Sr_{0.5}Co_{0.8}Fe_{0.2-x}Cu_xO_{3-\delta}$ and $Ba_{0.5}Sr_{0.5}Co_{0.8-x}Fe_{0.2}Cu_xO_{3-\delta}$ (x = 0, 0.05 and 0.1) after calcined at 1000°C for 5 hours.

Figure 3.8 shows the XRD patterns of Cu 0.05 and 0.1 mol partially replaced Fe and Co in BSCF. It showed single phase and cubic phase of BSCF doping with Cu at B. The unknown phase was observed in the XRD pattern of Cu0.1 mol doped at Fe site. The peaks of XRD patterns of doped Cu–BSCF slightly shifted to the lower angle. From Table 3.5, although the ionic radius of Cu^{2+} (0.87A°) was larger than Fe^{4+} (0.725A°) and Co^{4+} (0.67A°), the lattice parameters of BSCF doping with Cu at Fe and Co sites were not different from that of BSCF.

Table 3.5 The lattice parameters of $Ba_{0.5}Sr_{0.5}Co_{0.8}Fe_{0.2-x}Cu_xO_{3-\delta}$ and $Ba_{0.5}Sr_{0.5}Co_{0.8-x}Fe_{0.2}Cu_xO_{3-\delta}$ (x = 0, 0.05 and 0.1)

Sample	Lattice parameter (A°)
BSCF	3.9848
FeCu0.05	3.9825
FeCu0.1	3.9771
CoCu0.05	3.9790
CoCu0.1	3.9837

B) SEM images

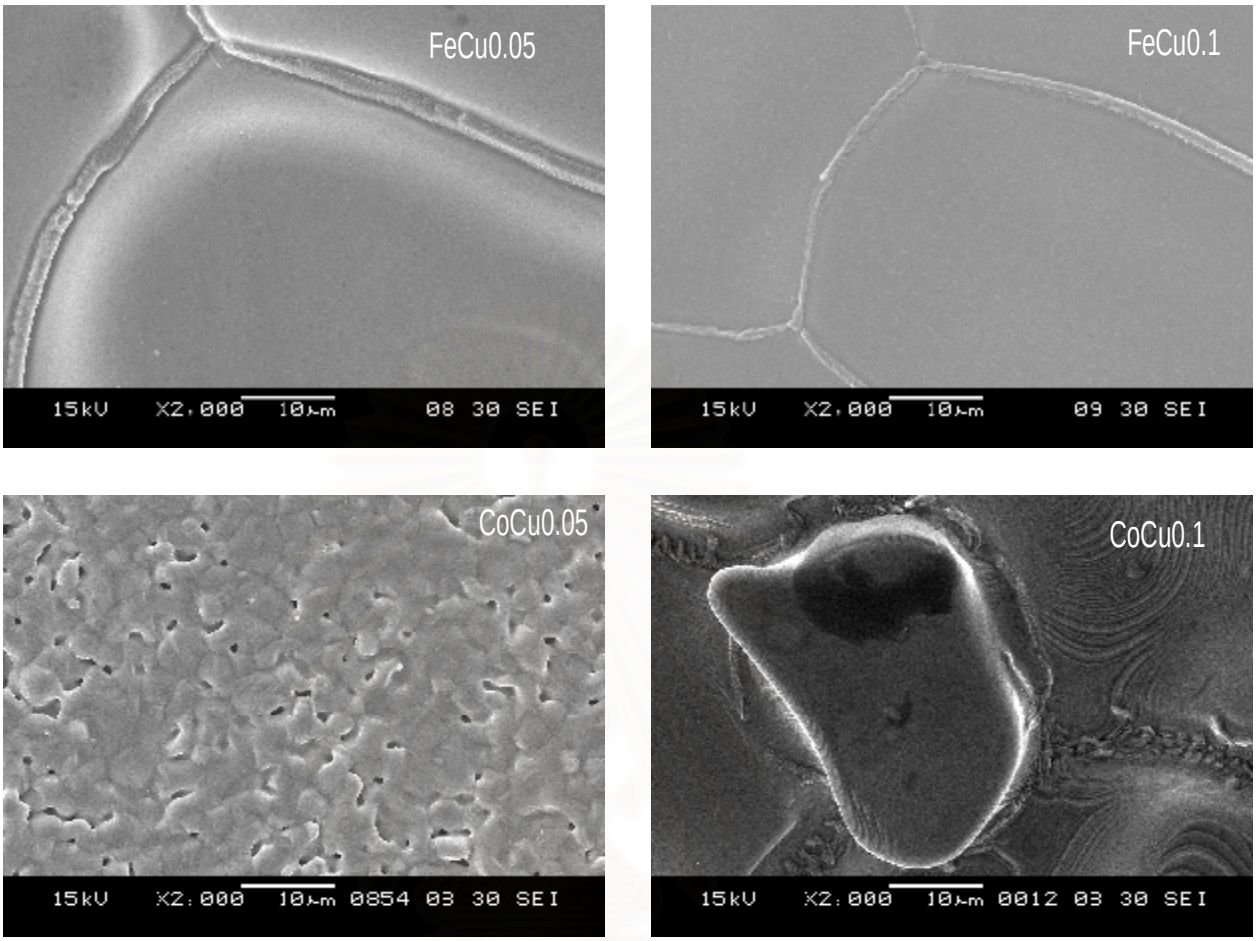

Figure 3.9 SEM micrographs of $Ba_{0.5}Sr_{0.5}Co_{0.8}Fe_{0.2-x}Cu_xO_{3-\delta}$ and $Ba_{0.5}Sr_{0.5}Co_{0.8-x}Fe_{0.2}Cu_xO_{3-\delta}$ (x = 0.05 and 0.1) after sintered at 1,100°C for 10 hours

Figure 3.9 show the morphologies of BSCF doped with Cu at Fe and Co sites. The results show that all of samples were homogeneous. It was noticed that FeCu0.05 and FeCu0.1 were denser than CoCu0.05 and CoCu0.1. The surface of CoCu0.1 disc was melted at 1,100°C. The grain size of FeCu0.05 and FeCu0.1 were more than 60µm but that of CoCu0.05 was in the range 2 to 10 µm. It is possible that doping with Cu can affect the melting point of these materials to decrease, so the grain sizes were larger than that of BSCF.

3.2.2 Effect of A site doping on the structure and morphology of BSCF

The structure stability of perovskite–type compound was determined by the tolerance factor. The calculated tolerance number of BSCF doping at A site was around 1 (Table 3.6). It revealed that the structures of the samples were stable cubic perovskite–type. The Pr and La doped at Ba and Sr site had small effect on the tolerance factors. With increasing content of Pr and La, the tolerance factors increased slightly. However, the numbers were still in the acceptable range 1.09–1.18.

Table 3.6 The tolerance number of A site doping on BSCF

Compounds	Tolerance No.
BSCF	1.07
Pr 0.05	1.09
Pr 0.1	1.11
Pr 0.15	1.14
Pr 0.2	1.16
La 0.05	1.09
La 0.1	1.12
La 0.15	1.15
La 0.2	1.18

3.2.2.1 Pr–doped BSCF

A) XRD results

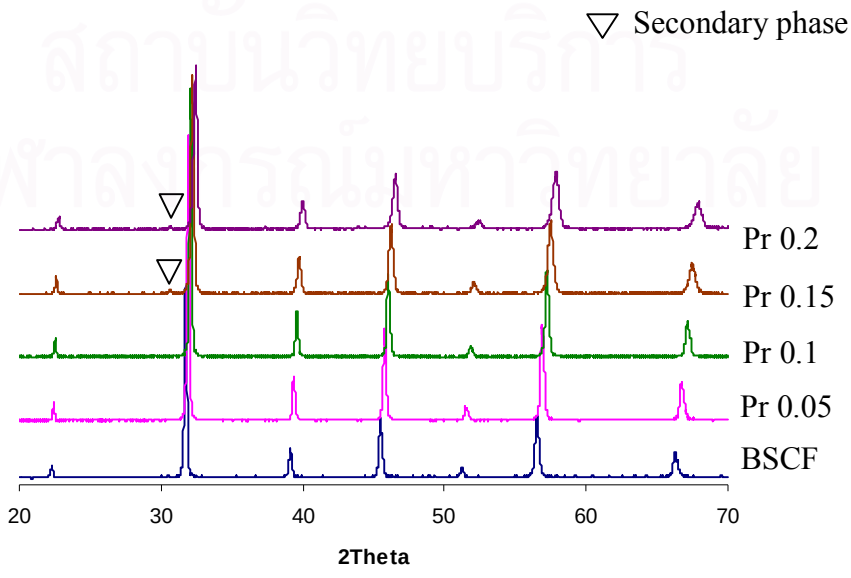

Figure 3.10 The XRD patterns of $(Ba_{0.5}Sr_{0.5})_{1-x}Pr_xCo_{0.8}Fe_{0.2}O_{3-\delta}$ (x = 0, 0.05, 0.1, 0.15 and 0.2) after calcined at 1000°C for 5 hours.

The XRD patterns of $(Ba_{0.5}Sr_{0.5})_{1-x}Pr_xCo_{0.8}Fe_{0.2}O_{3-\delta}$ with x = 0, 0.05, 0.1, 0.15 and 0.2 mol are shown in Figure 3.10. It was confirmed that all oxide samples had cubic perovskite structure. Single phase of perovskite structure was observed for doped BSCF when x = 0.05 and 0.1. A small unidentified impurity phase appeared at 2θ about 31° when x = 0.15 and 0.2. With the increasing of Pr, the XRD peaks shifted gradually to the higher angle corresponding to the lattice shrinkage as shown in Table 3.7. It can be explained that partially substitution of smaller Pr^{3+} (1.319A°) cation for Ba^{2+} (1.75A°) and Sr^{2+} (1.58A°) caused the decreasing of lattice parameters. On the other hand, the conversion of Co^{4+} to Co^{3+} and Fe^{4+} to Fe^{3+} respectively, on the B site to compensate electroneutrality of the oxide with the formation of oxygen vacancies can also affect the crystal lattice. It is concluded that the size and the charge of Pr had the effect on the crystal structure of BSCF.

Table 3.7 The lattice parameters of $(Ba_{0.5}Sr_{0.5})_{1-x}Pr_xCo_{0.8}Fe_{0.2}O_{3-\delta}$ (x = 0, 0.05, 0.1, 0.15 and 0.2)

Sample	Lattice parameter (A°)
BSCF	3.9848
Pr0.05	3.9608
Pr0.1	3.9410
Pr0.15	3.9203
Pr0.2	3.8964

B) SEM images

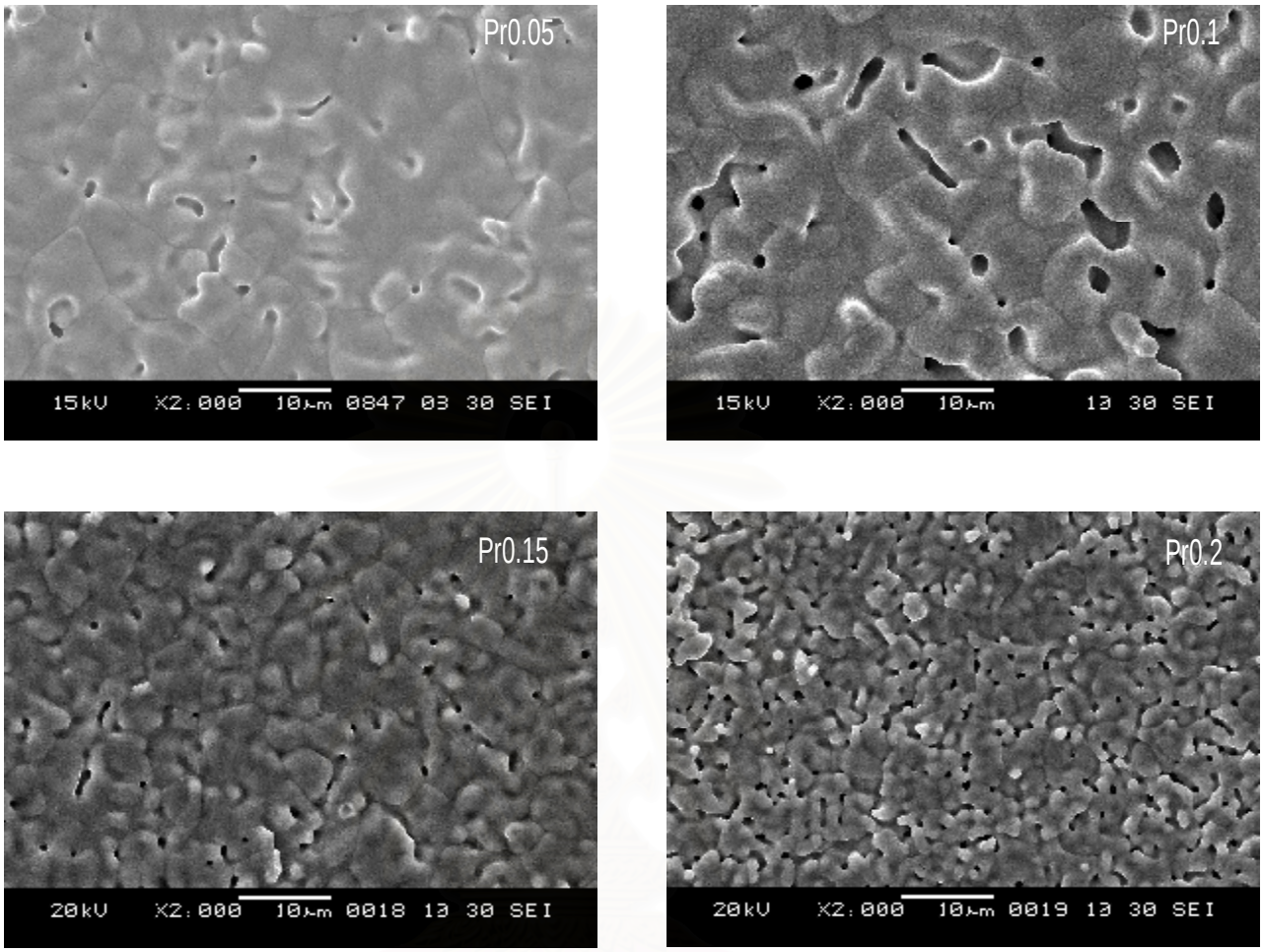

Figure 3.11 SEM micrograph of $(Ba_{0.5}Sr_{0.5})_{1-x}Pr_xCo_{0.8}Fe_{0.2}O_{3-\delta}$ (x = 0.05, 0.1, 0.15 and 0.2) after sintered at 1,100°C for 10 hours.

As given in Figure 3.11, the morphologies of doping BSCF with Pr^{3+} specimens with x =0.05, 0.1, 0.15 and 0.2 were homogeneous and the porosity increased with increasing Pr^{3+} contents. Moreover, the grain size decreased with increasing the amount of Pr^{3+}. It is seen that Pr0.05 was the largest grain size to be in range 5 to 30 µm.

3.2.2.2 La–doped BSCF

A) XRD results

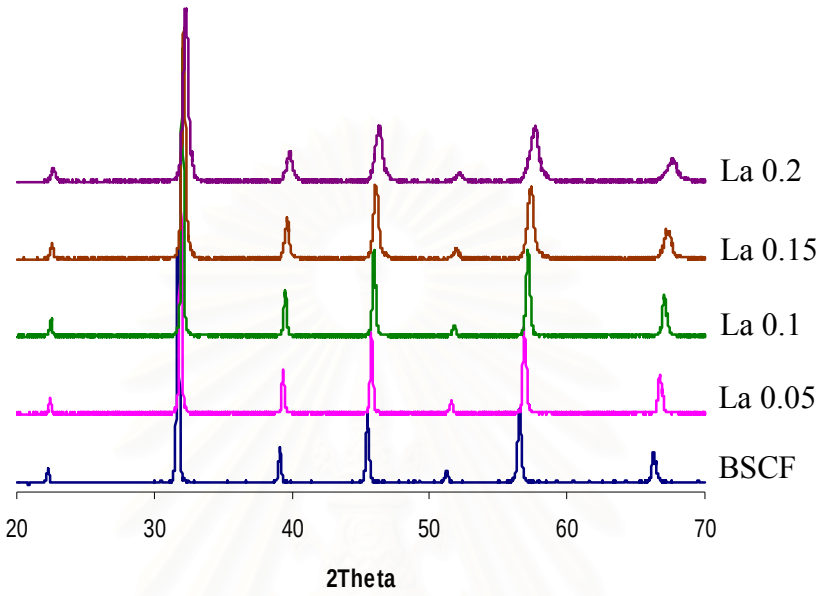

Figure 3.12 The XRD patterns of $(Ba_{0.5}Sr_{0.5})_{1-x}La_xCo_{0.8}Fe_{0.2}O_{3-\delta}$ (x = 0, 0.05, 0.1, 0.15 and 0.2) after calcined at 1000°C for 5 hours

The XRD patterns of $(Ba_{0.5}Sr_{0.5})_{1-x}La_xCo_{0.8}Fe_{0.2}O_{3-\delta}$ with x = 0.05, 0.1, 0.15 and 0.2 mol are shown in Figure 3.12. It exhibited that all BSCF doping with La in A sites of BSCF were single phase with cubic perovskite structure. The XRD peaks shifted clearly to the higher angle compared with BSCF. This shift increased with the increasing content of La^{3+}. The lattice parameters of BSCF doping with La^{3+} in the A sites of BSCF were lower than that of BSCF and it decreased with increasing of the amount of La^{3+} as shown in Table 3.8. The reason was that doping smaller ion of La^{3+} (1.5A°) at Ba^{2+} (1.75A°) and Sr^{2+} (1.58A°) and the change of oxidation state of Co^{4+} and Fe^{4+} and the formation of oxygen vacancies caused the shrinkage of lattice structure. As compared to Pr–doped BSCF, the effect of La–doped was less than Pr–doped perovskite oxide because La^{3+} is larger than Pr^{3+}. The lattice parameter of doping with La^{3+} 0.2 mol specimen was smallest.

Table 3.8 The lattice parameters of $(Ba_{0.5}Sr_{0.5})_{1-x}La_xCo_{0.8}Fe_{0.2}O_{3-\delta}$ (x = 0.05, 0.1, 0.15 and 0.2)

Sample	Lattice parameter (A°)
BSCF	3.9848
La0.05	3.9628
La0.1	3.9459
La0.15	3.9337
La0.2	3.9129

B) SEM images

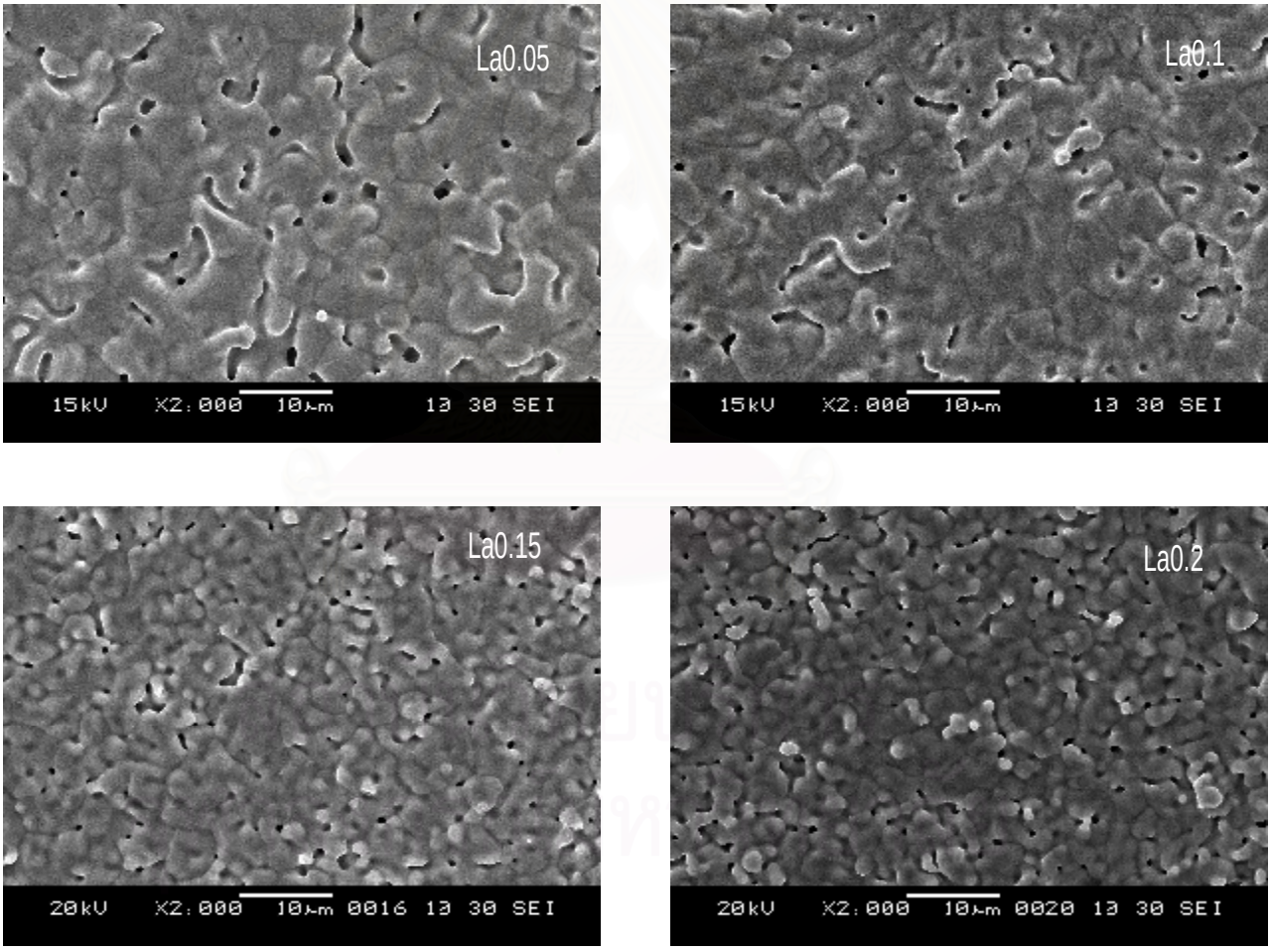

Figure 3.13 SEM micrograph of $(Ba_{0.5}Sr_{0.5})_{1-x}La_xCo_{0.8}Fe_{0.2}O_{3-\delta}$ (x = 0.05 and 0.1) after sintered at 1,100°C for 10 hours

In Figure 3.13, the microstructures of all La^{3+} specimens were homogeneous. The microstructural feature of the specimens is generally similar except different

grain sizes and the porosity. The grain sizes of the lower La^{3+} Contents was larger than that of the higher La^{3+} contents which was similar to the Pr^{3+} results. Furthermore, the porosity of the lower La^{3+} specimens were less than that of the higher La^{3+} specimens. Therefore, La0.05 had the largest grain size which varied in range 8 to 12 μm and lowest of porosity.

3.2.3 Effect of both A and B site doping on the structure and morphology of BSCF

The tolerance numbers of $(Ba_{0.5}Sr_{0.5})_{0.8}Pr_{0.2}Co_{0.8}Fe_{0.15}Cu_{0.05}O_{3-\delta}$ and $(Ba_{0.5}Sr_{0.5})_{0.8}La_{0.2}Co_{0.8}Fe_{0.15}Cu_{0.05}O_{3-\delta}$ were 1.16 and 1.17, respectively. It showed that the structure of perovskites were cubic.

3.2.3.1 Pr and Cu–doped BSCF

A) XRD results

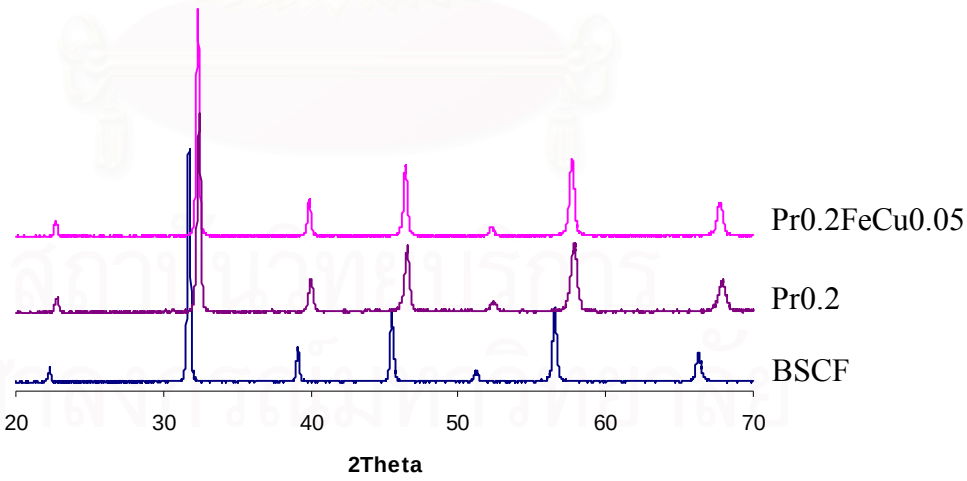

Figure 3.14 The XRD patterns of $(Ba_{0.5}Sr_{0.5})_{0.8}Pr_{0.2}Co_{0.8}Fe_{0.15}Cu_{0.05}O_{3-\delta}$ after calcined at 1000°C for 5 hours compared with $Ba_{0.5}Sr_{0.5}Co_{0.8}Fe_{0.2}O_{3-\delta}$ and $(Ba_{0.5}Sr_{0.5})_{0.8}Pr_{0.2}Co_{0.8}Fe_{0.2}O_{3-\delta}$.

In Figure 3.14, the XRD pattern of $(Ba_{0.5}Sr_{0.5})_{0.8}Pr_{0.2}Co_{0.8}Fe_{0.15}Cu_{0.05}O_{3-\delta}$ showed cubic perovskite-type structure that was similar to BSCF and doped Pr 0.2

mol specimen. The XRD peaks of $(Ba_{0.5}Sr_{0.5})_{0.8}Pr_{0.2}Co_{0.8}Fe_{0.15}Cu_{0.05}O_{3-\delta}$ shifted to the higher angle as compared with BSCF. It showed that Pr and Cu can be doped at A sites and B site simultaneously without distortion of the cubic structure. The lattice parameter of $(Ba_{0.5}Sr_{0.5})_{0.8}Pr_{0.2}Co_{0.8}Fe_{0.15}Cu_{0.05}O_{3-\delta}$ was less than that of BSCF but more than that of $(Ba_{0.5}Sr_{0.5})_{0.8}Pr_{0.2}Co_{0.8}Fe_{0.2}O_{3-\delta}$. It was expected that Pr and Cu partially replaced at A and B site caused the shrinkage of lattice structure (Table3.9).

Table 3.9 The lattice parameters of $(Ba_{0.5}Sr_{0.5})_{0.8}Pr_{0.2}Co_{0.8}Fe_{0.15}Cu_{0.05}O_{3-\delta}$ compared with $Ba_{0.5}Sr_{0.5}Co_{0.8}Fe_{0.2}O_{3-\delta}$ and $(Ba_{0.5}Sr_{0.5})_{0.8}Pr_{0.2}Co_{0.8}Fe_{0.2}O_{3-\delta}$.

Sample	Lattice parameter (A°)
BSCF	3.9848
Pr0.2	3.8964
Pr0.2FeCu0.05	3.9104

B) SEM images

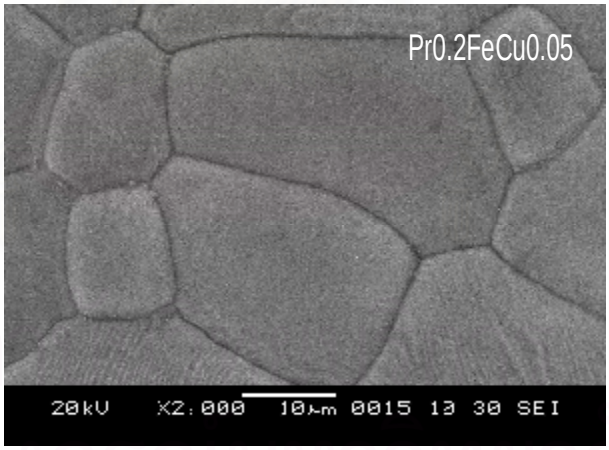

Figure 3.15 SEM micrograph of $(Ba_{0.5}Sr_{0.5})_{0.8}Pr_{0.2}Co_{0.8}Fe_{0.15}Cu_{0.05}O_{3-\delta}$ after sintered at 1,100°C for 10 hours.

The microstructure of Pr0.2FeCu0.05 as shown in Figure 3.15 was homogeneous. It was noticed that the surface of the disc of Pr0.2FeCu0.05 was denser than Pr0.2. Also, the grain size was larger than Pr0.2 and it varied in the range of 10 to 32 μm.

3.2.3.2 La and Cu–doped BSCF

A) XRD results

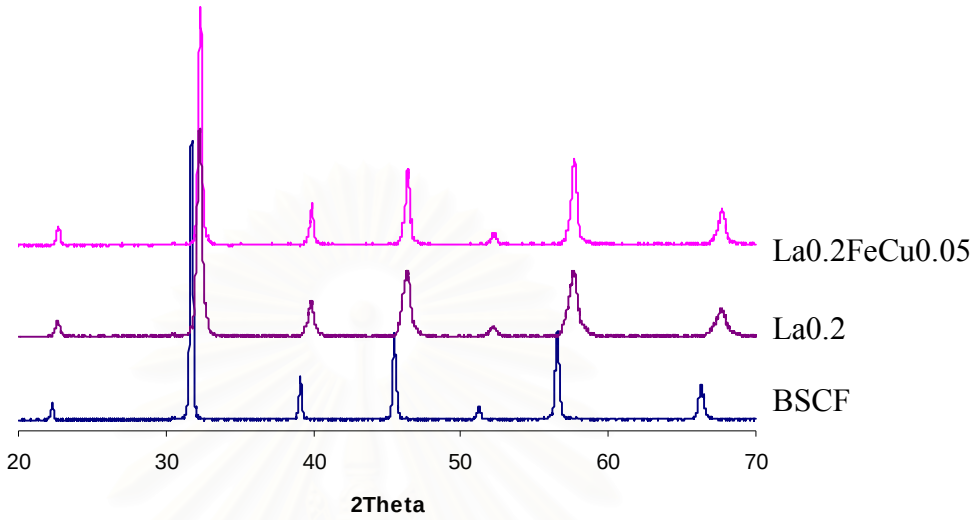

Figure 3.16 The XRD patterns of $(Ba_{0.5}Sr_{0.5})_{0.8}La_{0.2}Co_{0.8}Fe_{0.15}Cu_{0.05}O_{3-\delta}$ after calcined at 1000°C for 5 hours compared with $Ba_{0.5}Sr_{0.5}Co_{0.8}Fe_{0.2}O_{3-\delta}$ and $(Ba_{0.5}Sr_{0.5})_{0.8}La_{0.2}Co_{0.8}Fe_{0.2}O_{3-\delta}$.

The XRD pattern of $(Ba_{0.5}Sr_{0.5})_{0.8}La_{0.2}Co_{0.8}Fe_{0.15}Cu_{0.05}O_{3-\delta}$ showed single phase and cubic structure (Figure 3.16) and XRD peaks of $(Ba_{0.5}Sr_{0.5})_{0.8}La_{0.2}Co_{0.8}Fe_{0.15}Cu_{0.05}O_{3-\delta}$ shift to the higher angle as compared to BSCF and La0.2. It presented that La and Cu can be doped at A sites and B site simultaneously without distortion. The lattice parameter of $(Ba_{0.5}Sr_{0.5})_{0.8}La_{0.2}Co_{0.8}Fe_{0.15}Cu_{0.05}O_{3-\delta}$ was less than that of BSCF but it was more than that of BSCF doping with La^{3+} 0.2 mol specimen because ionic radius of Cu^{2+}(0.87A°) was larger than that of Fe^{4+}(0.725A°) (Table 3.10).

Table 3.10 The lattice parameter of $(Ba_{0.5}Sr_{0.5})_{0.8}La_{0.2}Co_{0.8}Fe_{0.15}Cu_{0.05}O_{3-\delta}$ compared with $Ba_{0.5}Sr_{0.5}Co_{0.8}Fe_{0.2}O_{3-\delta}$ and $(Ba_{0.5}Sr_{0.5})_{0.8}La_{0.2}Co_{0.8}Fe_{0.2}O_{3-\delta}$.

Sample	Lattice parameter (A°)
BSCF	3.9848
La0.2	3.9129
La0.2FeCu0.05	3.9100

B) SEM images

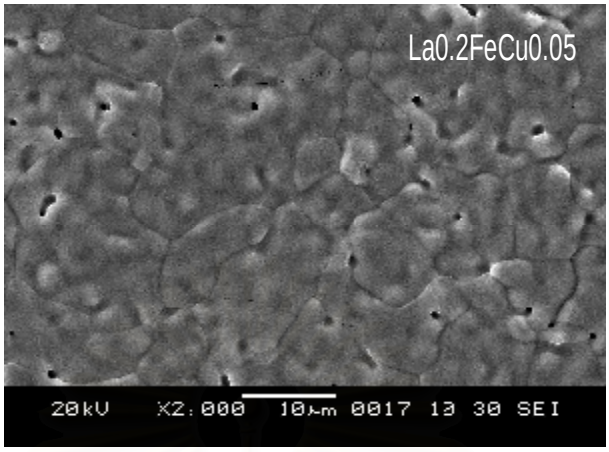

Figure 3.17 SEM micrograph of $(Ba_{0.5}Sr_{0.5})_{0.8}La_{0.2}Co_{0.8}Fe_{0.15}Cu_{0.05}O_{3-\delta}$ after sintered at 1,100°C for 10 hours.

The microstructure of La0.2FeCu0.05 was homogeneous as shown in Figure 3.17. Also, the porosity of La0.2FeCu0.05 was lower and the grain size (9 to 20 μm) was larger than that of La0.2.

It can be concluded that doping with Cu at B site improved the density and increased the grain size because Cu decreased the melting point of the specimens.

From the characterization by XRD and SEM, it is concluded that Mg and Ni can not be doped at B site in BSCF. However, all of Zn and Cu can be doped at B site in BSCF except FeCu0.1. For A site, Pr and La can be doped in that structure. Moreover, doping with both A site and B site can also be doped in BSCF. Hence, the properties pure phase and homogeneous samples listed in Table 3.11 were investigated.

Table 3.11 Summary the results of XRD and SEM

Sample	XRD	SEM	Pure phase
BSCF	√	√	√
FeMg 0.05	√	×	×
FeNi 0.05	√	×	×
FeZn 0.05	√	√	√
FeCu 0.05	√	√	√
CoMg 0.05	√	×	×
CoNi 0.05	√	×	×
CoZn 0.05	√	√	√
CoCu 0.05	√	√	√
Pr 0.05	√	√	√
La 0.05	√	√	√
FeMg 0.1	×	×	×
FeNi 0.1	√	×	×
FeZn 0.1	√	√	√
FeCu 0.1	×	√	×
CoMg 0.1	×	×	×
CoNi 0.1	√	×	×
CoZn 0.1	√	√	√
CoCu 0.1	√	√	√
Pr 0.1	√	√	√
La 0.1	√	√	√
Pr 0.15	√	√	√
La 0.15	√	√	√
Pr 0.2	√	√	√
La 0.2	√	√	√
Pr0.2FeCu0.05	√	√	√
La0.2FeCu0.05	√	√	√

√ **Pure phase** × **Impure phase**

3.3 Effect of A and B–sites doping on the oxygen vacancies of BSCF

One of characteristic features of perovskites was the adsorption–desorption a large amount of oxygen from crystal lattice with keeping the fundamental crystal structure intact when heated. The desorption and uptake of oxygen from and into the crystal lattice involve not only the migration of oxide ions in the bulk but also the association and dissociation of oxygen on the surface. Actually, there is well correlation between the permeation flux and the amount of thermally desorbed oxygen [28]. The oxygen desorption property of synthesized perovskites are described.

In general, the desorption peaks plotted from the perovskite-like mixed oxides contain three kinds of oxygen species. The desorption peak appeared at $T < 300$ °C is ascribed to the oxygen chemically adsorbed on the surface (denoted as: α oxygen); the desorption peak appeared at $300 < T < 800$ °C is ascribed to the oxygen chemically adsorbed on the oxygen vacancy (denoted as: β oxygen); and the desorption peak appeared at $T > 800$ °C is ascribed to the oxygen escaped from the lattice (denoted as: γ oxygen) [29]. With the programmed rise of the temperature, oxygen releases from the lattice, associating with the reduction of metal ions from high valence state to lower valence state and the creation of oxygen vacancies. For Co and/or Fe containing perovskites, the oxygen desorption peak appeared at intermediate temperatures (300–600°C) corresponding to the reduction of high valence state Co^{4+} and/or Fe^{4+} to tri–valence state Co^{3+} and/or Fe^{3+}. On the other hand, the loss of lattice oxygen at elevated temperatures would lead to the expansion of lattice distance [30, 31, 32].

3.3.1 Effect of B site doping on the oxygen vacancies of BSCF

3.3.1.1 Zn–doped BSCF

Figure 3.18 show the oxygen desorption profiles of BSCF and Zn specimens. The amount of oxygen desorption is determined from the peak area illustrated in Table 3.12.

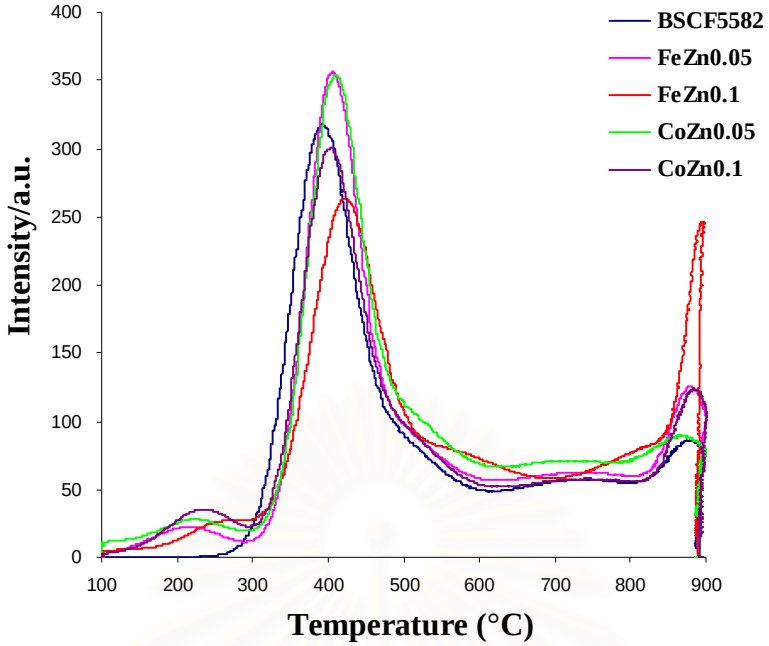

Figure 3.18 Oxygen temperature programmed desorption curves of $Ba_{0.5}Sr_{0.5}Co_{0.8}Fe_{0.2-x}Zn_xO_{3-\delta}$ and $Ba_{0.5}Sr_{0.5}Co_{0.8-x}Fe_{0.2}Zn_xO_{3-\delta}$ (x = 0, 0.05 and 0.1)

Table 3.12 The oxygen desorption of $Ba_{0.5}Sr_{0.5}Co_{0.8}Fe_{0.2-x}Zn_xO_{3-\delta}$ and $Ba_{0.5}Sr_{0.5}Co_{0.8-x}Fe_{0.2}Zn_xO_{3-\delta}$ (x = 0, 0.05 and 0.1)

Sample	a **oxygen (mmol/g)**	b **oxygen (mmol/g)**	g **oxygen (mmol/g)**
BSCF	-	0.3222	0.1664
FeZn0.05	0.0196	0.3550	0.1557
FeZn0.1	0.021	0.3377	0.2406
CoZn0.05	0.0252	0.3562	0.1545
CoZn0.1	0.0316	0.3676	0.1731

The α oxygen desorption peaks (150-300°C) were observed in all Zn specimens except BSCF. For doping BSCF with Zn 0.05 mol, the amount of oxygen desorption of doping with Zn at Fe was similar to that of doping Zn at Co. The values were more than that of BSCF. It was found that the β oxygen desorbed at intermediate temperature zone increased with increasing of Zn^{2+} doped at Co site. On the contrary, the amount of β oxygen desorbed decrease with increasing Zn replaced in Fe site. However, the introduction of Zn in BSCF had little influence on the onset temperature of oxygen desorption. The γ oxygen desorption peaks were observed for most of the oxides except $Ba_{0.5}Sr_{0.5}Co_{0.8}Fe_{0.1}Zn_{0.1}O_{3-\delta}$, which demonstrated one sharp peak at a

temperature zone higher than 800°C which corresponds to the thermal reduction part of Co^{3+} to Co^{2+}[33].

From the O_2–TPD results, it is concluded that the introduction of Zn^{2+} in BSCF can suppress the oxidation of Fe^{3+} and Co^{3+} to Fe^{4+} and Co^{4+}. The formation of oxygen vacancies in doped BSCF increased as compared to BSCF (see β oxygen desorption). It is suggested that doping with Zn increased oxygen vacancies (β oxygen) because valence state of Zn (+2) was lower than that of Co (+3 or +4) and Fe (+3 or +4). Therefore, the perovskite had to adjust the structure by releasing oxygen and oxygen vacancies were formed for balancing the charge [29].

At high temperature, Zn^{2+} 0.1 mol doped at Fe site had great influence on the reducibility of Co^{3+} to Co^{2+}. It should be acknowledged that doping site is also important. The result indicated that γ oxygen desorbed from crystal lattice of $Ba_{0.5}Sr_{0.5}Co_{0.8}Fe_{0.1}Zn_{0.1}O_{3-\delta}$ (0.2406 mmol/g) was more than that of $Ba_{0.5}Sr_{0.5}Co_{0.7}Fe_{0.2}Zn_{0.1}O_{3-\delta}$ (0.1731 mmol/g). There are two reasons to explain the release of oxide ions from the lattice. Firstly, the radius change associated with the transformation of the amount of Co^{3+} to Co^{2+}. Secondly, bond strength of Fe–O is greater than Co–O. Therefore, the amount of oxide ion in FeZn0.1 can be expelled more than CoZn0.1.

3.3.1.2 Cu–doped BSCF

The oxygen desorption curves of Cu specimens were shown in Figure 3.19 and amount of oxygen desorption were presented in Table 3.13.

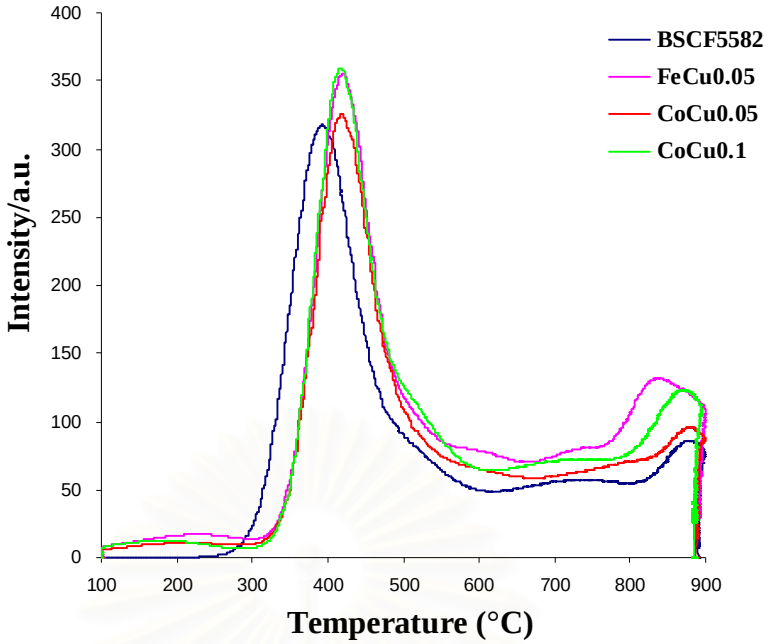

Figure 3.19 Oxygen temperature programmed desorption curves of $Ba_{0.5}Sr_{0.5}Co_{0.8}Fe_{0.15}Cu_{0.05}O_{3-\delta}$ and $Ba_{0.5}Sr_{0.5}Co_{0.8-x}Fe_{0.2}Cu_xO_{3-\delta}$ (x = 0, 0.05 and 0.1)

Table 3.13 The oxygen desorption of $Ba_{0.5}Sr_{0.5}Co_{0.8}Fe_{0.15}Cu_{0.05}O_{3-\delta}$ and $Ba_{0.5}Sr_{0.5}Co_{0.8-x}Fe_{0.2}Cu_xO_{3-\delta}$ (x = 0, 0.05 and 0.1)

Sample	a **oxygen (mmol/g)**	b **oxygen (mmol/g)**	g **oxygen (mmol/g)**
BSCF	-	0.3222	0.1664
FeCu0.05	0.0149	0.3563	0.2067
CoCu0.05	0.0135	0.3432	0.1560
CoCu0.1	0.0133	0.3608	0.1873

For the O_2–TPD results of Cu specimens, there are three oxygen desorption peaks in all Cu specimens. The amount of α oxygen of Cu specimens were less than that of Zn specimens. In addition, the amount of β oxygen of FeCu0.05 was higher than that of CoCu0.05 indicating more oxygen vacancies. For doping Cu at Co site, the amount of β and γ oxygen increased with increasing Cu contents. Moreover, the onset temperature of oxygen desorption of all Cu specimens were shifted to the higher temperature compared to BSCF. It indicated the substitution of Cu influence the bonding energy of metal ion–oxygen in the lattice resulting to release oxygen from

the lattice. Furthermore, FeCu0.05 showed the highest γ oxygen contents. Corresponding to Zn results**, it is confirmed that BSCF doping at Fe site were influence on reducibility of Co^{3+} to Co^{2+} more than that of Co site at high temperature.**

3.3.2 Effect of A site doping on the oxygen vacancies of BSCF

3.3.2.1 Pr–doped BSCF

The O_2-TPD profiles of Pr specimens with varying Pr contents were shown in Figure 3.20 and Table 3.14. No α oxygen desorption peak was observed in all Pr specimens. At high temperature, it was found that the amount of oxygen desorption of β oxygen increased with increasing doping contents of Pr. Doping A site of BSCF with concentration of Pr > 0.05 lowered the temperature for the onset temperature of oxygen desorption and the temperature for the desorption maximum (see Figure 3.20). It is expected that the introduction of Pr increased the amount of Co^{3+} and Fe^{3+}, whose ability to oxygen astriction was lower than that of Co^{4+} and Fe^{4+}. Thus the Pr doping promoted the oxygen diffusion, which was benefit to the reaction in equation (1) and (2).

$$2Co_{Co}^{\bullet} + O_O^{x} \rightleftharpoons 2Co_{Co}^{x} + V_O^{\bullet\bullet} + \frac{1}{2}O_2 \qquad (1)$$

$$2Fe_{Fe}^{\bullet} + O_O^{x} \rightleftharpoons 2Fe_{Fe}^{x} + V_O^{\bullet\bullet} + \frac{1}{2}O_2 \qquad (2)$$

$Co_{Co}^{\bullet}$ = a cobalt ion sitting on a cobalt lattice site with singular positive charge.

Co_{Co}^{x} = a cobalt ion sitting on a cobalt lattice site with neutral charge.

$Fe_{Fe}^{\bullet}$ = an iron ion sitting on a iron lattice site with singular positive charge.

Fe_{Fe}^{x} = an iron ion sitting on a iron lattice site with neutral charge.

O_O^{x} = an oxide ion sitting on an oxide lattice site, with neutral charge.

$V_O^{\bullet\bullet}$ = an oxygen vacancy with double positive charge.

At high temperature, γ oxygen desorption decreased when x = 0.05 and 0.1 and increased when x = 0.15 and 0.2 suggested that doping only small amount of Pr had no effect on the reduction of Co^{3+} to Co^{2+}. It is suggested that the amount of released oxygen from the lattice increased with increasing Pr contents.

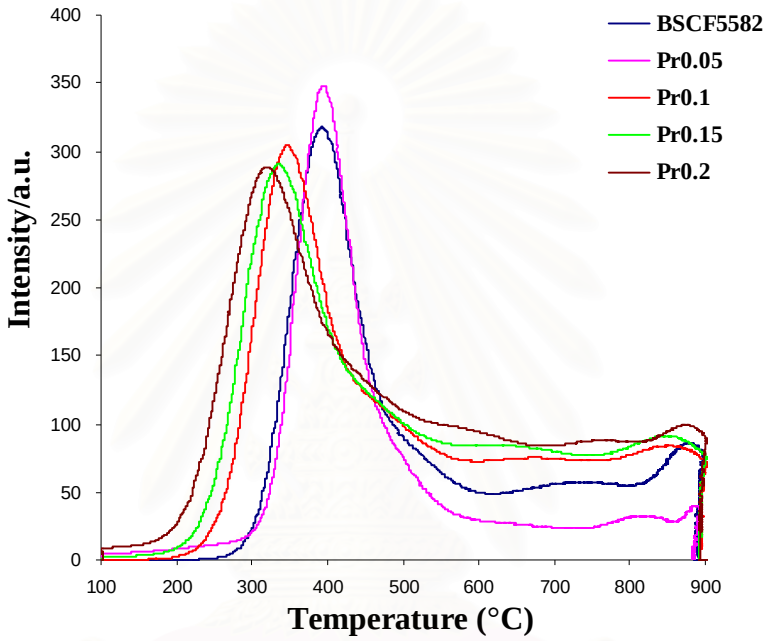

Figure 3.20 Oxygen temperature programmed desorption curves of $(Ba_{0.5}Sr_{0.5})_{1-x}Pr_xCo_{0.8}Fe_{0.2}O_{3-\delta}$ (x = 0, 0.05 and 0.1)

Table 3.14 The oxygen desorption of $(Ba_{0.5}Sr_{0.5})_{1-x}Pr_xCo_{0.8}Fe_{0.2}O_{3-\delta}$ (x = 0, 0.05, 0.1, 0.15 and 0.2)

Sample	a **oxygen (mmol/g)**	b **oxygen (mmol/g)**	g **oxygen (mmol/g)**
BSCF	-	0.3222	0.1664
Pr0.05	-	0.3133	0.0462
Pr0.1	-	0.4361	0.1603
Pr0.15	-	0.5090	0.2035
Pr0.2	-	0.5118	0.1844

3.3.2.2 La–doped BSCF

Two oxygen desorption peaks (β and γ oxygen) of La specimens are shown in Figure 3.21 and Table 3.15. It can be seen that the β oxygen increased with increasing La contents similar to the result for doping Pr. Doping with La in BSCF induced the reduction of high valence state Co^{4+} and/or Fe^{4+} to tri–valence state Co^{3+} and/or Fe^{3+} for balancing the charge in the structure. In oxygen desorption at high temperature, the γ oxygen were lower than that of BSCF except La0.1.

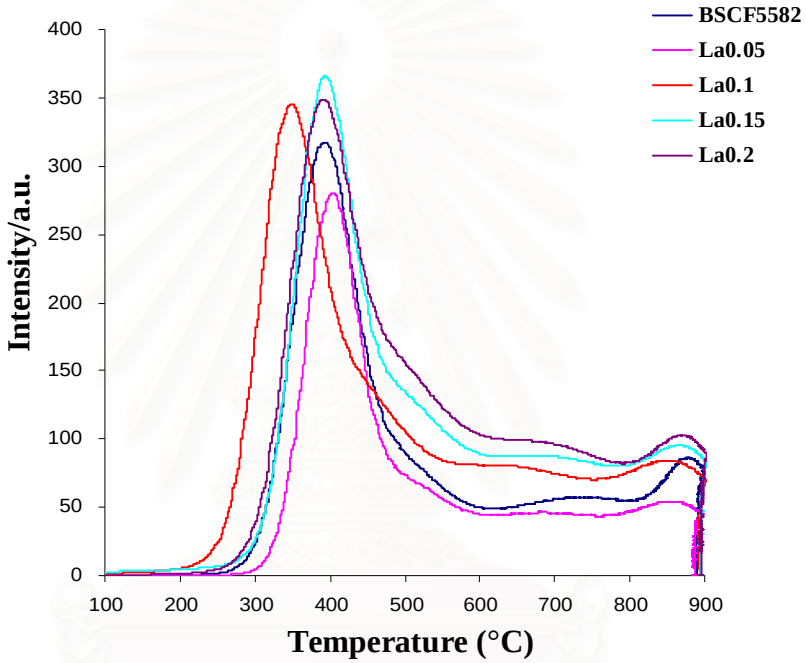

Figure 3.21 Oxygen temperature programmed desorption curves of $(Ba_{0.5}Sr_{0.5})_{1-x}La_xCo_{0.8}Fe_{0.2}O_{3-\delta}$ (x = 0, 0.05 and 0.1, 0.15, 0.2)

Table 3.15 The oxygen desorption of $(Ba_{0.5}Sr_{0.5})_{1-x}La_xCo_{0.8}Fe_{0.2}O_{3-\delta}$ (x = 0, 0.05 and 0.1, 0.15 and 0.2)

Sample	a **oxygen (mmol/g)**	b **oxygen (mmol/g)**	g **oxygen (mmol/g)**
BSCF	-	0.3222	0.1664
La0.05	-	0.3848	0.1160
La0.1	-	0.4360	0.1833
La0.15	-	0.4510	0.1406
La0.2	-	0.5261	0.1538

3.3.3 Effect of both A and B site doping on the oxygen vacancies of BSCF

3.3.3.1 Pr and Cu–doped BSCF

The O_2 TPD profile of Pr0.2FeCu0.05 is shown in Figure 3.22 and Table 3.16. The amount of β oxygen of Pr0.2FeCu0.05 was more than that of BSCF but was less than that of Pr0.2. In addition, the oxygen from lattice (γ oxygen) were less than that of BSCF and Pr0.2. Therefore, the oxygen vacancies of doping at both A and B sites were less than that of doping with A site.

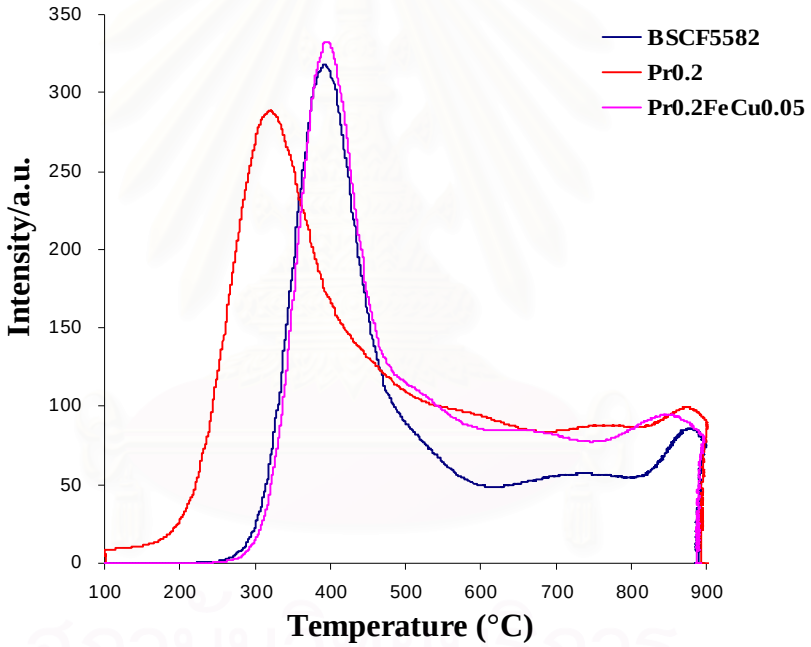

Figure 3.22 Oxygen temperature programmed desorption curves of $(Ba_{0.5}Sr_{0.5})_{0.8}Pr_{0.2}Co_{0.8}Fe_{0.15}Cu_{0.05}O_{3-\delta}$ compared with $Ba_{0.5}Sr_{0.5}Co_{0.8}Fe_{0.2}O_{3-\delta}$ and $(Ba_{0.5}Sr_{0.5})_{0.8}Pr_{0.2}Co_{0.8}Fe_{0.2}O_{3-\delta}$

Table 3.16 The oxygen desorption of $(Ba_{0.5}Sr_{0.5})_{0.8}Pr_{0.2}Co_{0.8}Fe_{0.15}Cu_{0.05}O_{3-\delta}$ compared with $Ba_{0.5}Sr_{0.5}Co_{0.8}Fe_{0.2}O_{3-\delta}$ and $(Ba_{0.5}Sr_{0.5})_{0.8}Pr_{0.2}Co_{0.8}Fe_{0.2}O_{3-\delta}$

Sample	a **oxygen (mmol/g)**	b **oxygen (mmol/g)**	g **oxygen (mmol/g)**
BSCF	-	0.3222	0.1664
Pr0.2	-	0.5118	0.1844
Pr0.2FeCu0.05	-	0.4226	0.1601

3.3.3.2 La and Cu–doped BSCF

As given in Figure 3.23 and Table 3.17, there are two oxygen desorption peaks. The oxygen vacancies (β oxygen) of La0.2Fe0.05 were more than that of BSCF but less than that of La0.2.

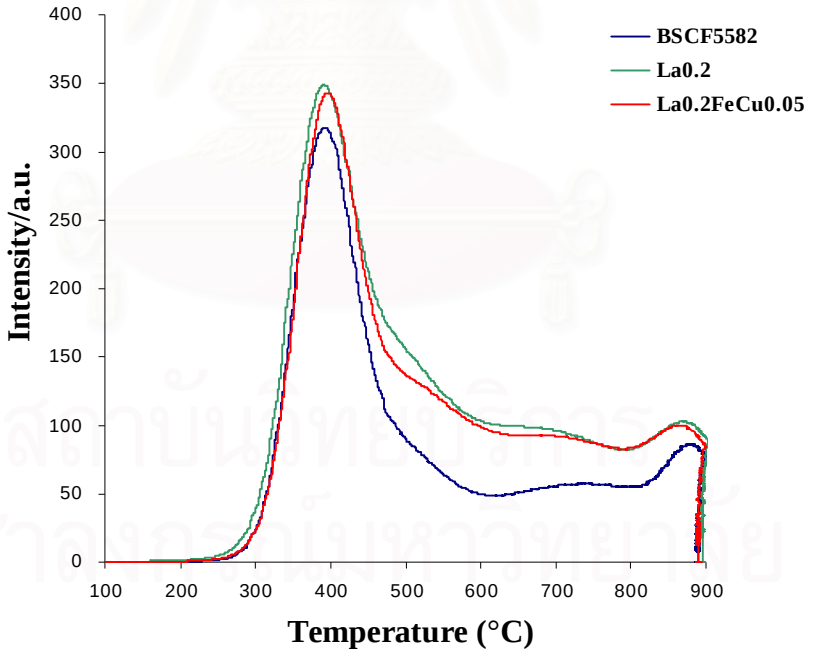

Figure 3.23 Oxygen temperature programmed desorption curves of $(Ba_{0.5}Sr_{0.5})_{0.8}La_{0.2}Co_{0.8}Fe_{0.15}Cu_{0.05}O_{3-\delta}$ compared with $Ba_{0.5}Sr_{0.5}Co_{0.8}Fe_{0.2}O_{3-\delta}$ and $(Ba_{0.5}Sr_{0.5})_{0.8}La_{0.2}Co_{0.8}Fe_{0.2}O_{3-\delta}$

Table 3.17 The oxygen desorption of $(Ba_{0.5}Sr_{0.5})_{0.8}Pr_{0.2}Co_{0.8}Fe_{0.15}Cu_{0.05}O_{3-\delta}$ compared with $Ba_{0.5}Sr_{0.5}Co_{0.8}Fe_{0.2}O_{3-\delta}$ and $(Ba_{0.5}Sr_{0.5})_{0.8}Pr_{0.2}Co_{0.8}Fe_{0.2}O_{3-\delta}$

Sample	a **oxygen (mmol/g)**	b **oxygen (mmol/g)**	g **oxygen (mmol/g)**
BSCF	-	0.3222	0.1664
La0.2	-	0.5261	0.1538
La0.2FeCu0.05	-	0.4567	0.1801

3.4 Effect of A and B–sites doping on the electrical conductivity of BSCF

Generally, there are two kinds of conductive mechanisms (electronic and ionic conductivity) in these perovskite oxides, owing to the co-presence of holes and oxygen vacancies. Since the ionic conductivity is about two orders of magnitude lower than the electronic conductivity [34], it can be reasonably assumed that the measured values mainly refer to the electronic conductivity. In this section, the conductivities of perovskite membranes were studied by DC-4 probe technique.

Undoped BSCF

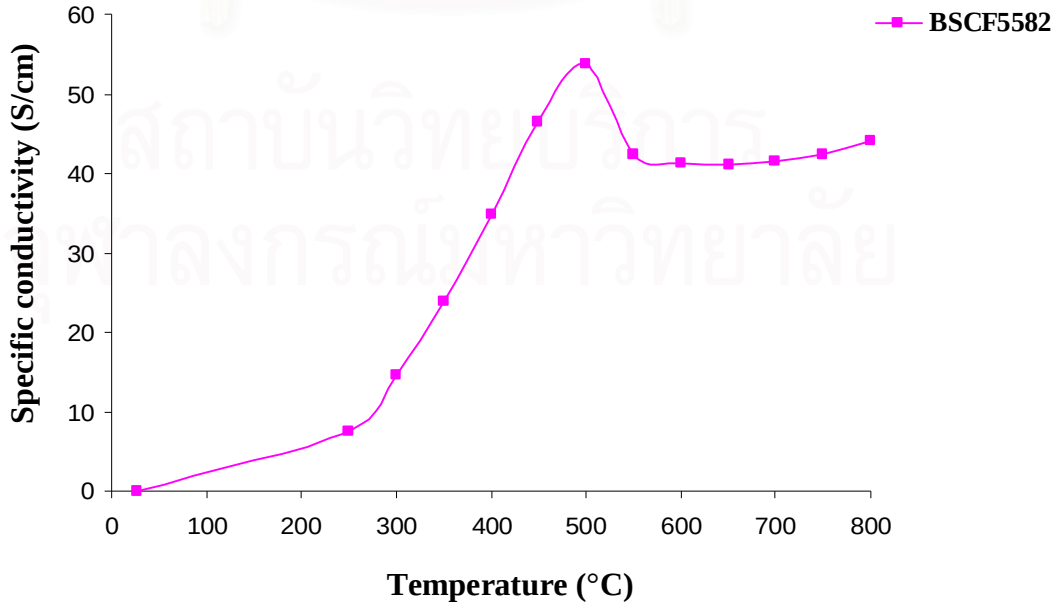

Figure 3.24 Variations of the electrical conductivity measured in air of $Ba_{0.5}Sr_{0.5}Co_{0.8}Fe_{0.2}O_{3-\delta}$ with temperature.

As presented in Figure 3.24, the electrical conductivity of BSCF increased gradually with temperature and had the maximum electrical conductivity at 500°C. This was due to the behavior of lattice oxygen that became active at this temperature range [35]. It showed the maximum conductivity of 53.7 S/cm at 500°C and the activation energy calculated from the linear part of Figure 3.25 was 36.17 kJ/mol. The conductivity mechanism can be attributed to two factors. Firstly, the hopping of p–type small polarons were associated with the behavior of triple and tetravalent states of Co and Fe cations. The electron transition between the triple and the tetravalent of Co and Fe caused the electronic conductivity. Secondly, along with the thermal induced lattice oxygen losses, more oxygen deficiency was formed, which thus caused the thermal reduction of Co and Fe cations to lower states, described in equations (1) and (2) [35].

$$2Co_{Co}^{\bullet} + O_O^{x} \rightleftharpoons 2Co_{Co}^{x} + V_O^{\bullet\bullet} + \frac{1}{2}O_2 \qquad (1)$$

$$2Fe_{Fe}^{\bullet} + O_O^{x} \rightleftharpoons 2Fe_{Fe}^{x} + V_O^{\bullet\bullet} + \frac{1}{2}O_2 \qquad (2)$$

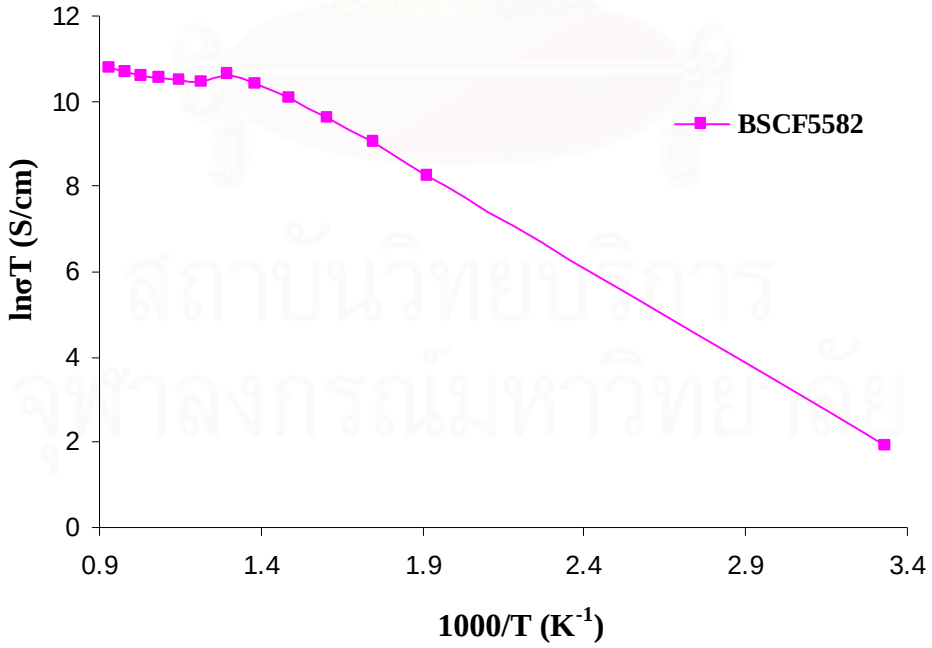

Figure 3.25 Arrhenius plot of $Ba_{0.5}Sr_{0.5}Co_{0.8}Fe_{0.2}O_{3-\delta}$

3.4.1 Effect of B site doping on the electrical conductivity of BSCF

3.4.1.1 Zn–doped BSCF

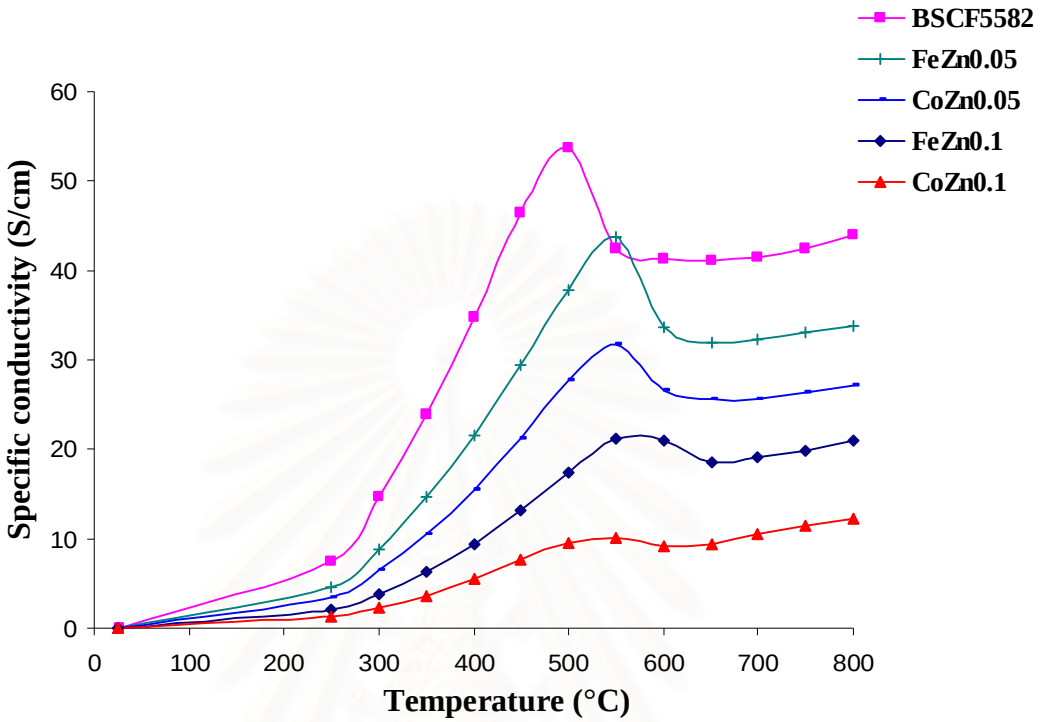

Figure 3.26 Variations of the electrical conductivity measured in air of $Ba_{0.5}Sr_{0.5}Co_{0.8}Fe_{0.2-x}Zn_xO_{3-\delta}$ and $Ba_{0.5}Sr_{0.5}Co_{0.8-x}Fe_{0.2}Zn_xO_{3-\delta}$ (x = 0, 0.05 and 0.1) with temperature

In Figure 3.26 and Table 3.18, the electrical conductivity of Zn doped BSCF was measured in air as a function of temperature indicating a semi–conducting behavior at low temperatures ($T \leq 550°C$). The electrical conductivity of each composition increased with temperature up to its a maximum value and then decreased. Compared among different composition, the conductivity decreased with increasing Zn contents. The reasons for the relatively low conductivity of Zn specimens can be mainly intercepted as follows. The first one was the high vacancy concentration in Zn specimen lattice. There is large concentration of oxygen vacancy, which will lead to the significantly decrease in charge carriers concentration. In addition, the vacancies can also act as the scattering centers, or as random traps for electrons, resulting in the decrease of the carrier mobility [36]. The second reason can be ascribed to the fact that Zn holds fixed bivalent state, which will not contribute to the conductivity. With Zn doping in B-sites, the conductivity will decrease due to the decrease of the total concentration at Co and Fe at B–sites that participated in the

electronic transport processes. Moreover, it can be seen that electrical conductivities of BSCF doped with Zn by replacing Fe were more than those of BSCF doped with Zn by replacing Co. It showed that contribution of Co on electrical conductivity were more than that of Fe [37].

Table3.18 The specific conductivity of $Ba_{0.5}Sr_{0.5}Co_{0.8}Fe_{0.2-x}Zn_xO_{3-\delta}$ and $Ba_{0.5}Sr_{0.5}Co_{0.8-x}Fe_{0.2}Zn_xO_{3-\delta}$ (x = 0, 0.05 and 0.1)

Sample	Specific conductivity, σ (S/cm)						
	300°C	400°C	500°C	600°C	700°C	800°C	σ_{max} (T,°C)
BSCF	14.7	34.8	53.7	41.2	41.4	44.4	53.7 (500)
FeZn0.05	8.9	21.5	37.8	33.6	32.2	33.9	43.8 (550)
CoZn0.05	6.4	15.5	27.7	26.6	25.7	27.2	31.7 (550)
FeZn0.10	3.9	9.4	17.3	21.1	19.1	21.0	21.2 (550)
CoZn0.10	2.2	5.5	9.6	9.3	10.4	12.3	12.3 (800)

The activation energy of Zn specimens calculated from the linear part of Figure 3.27 were shown in Table 3.19. The activation energies of Zn specimens were slightly different with that of BSCF.

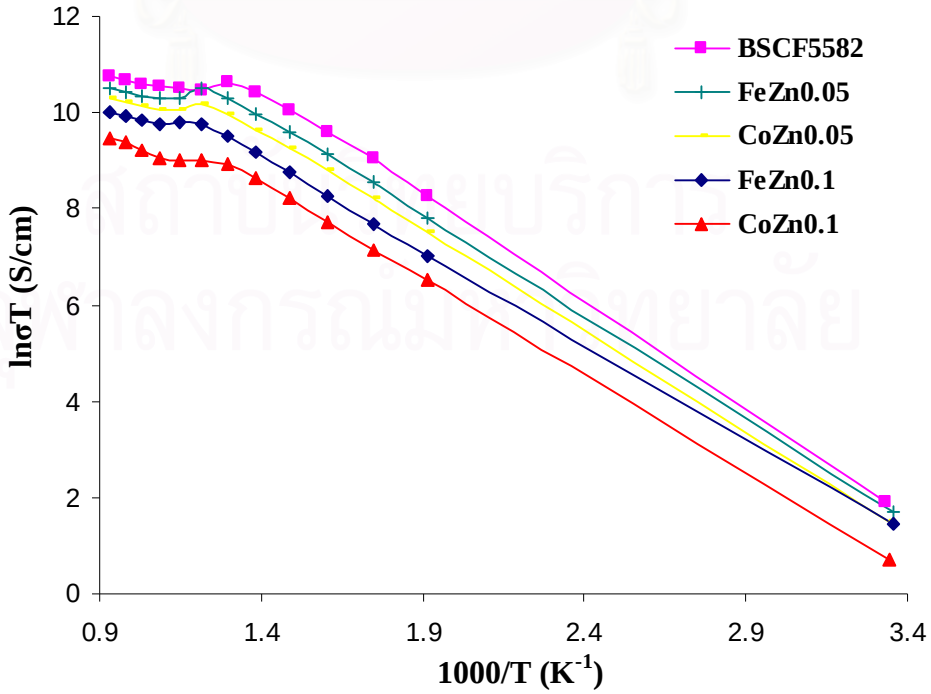

Figure 3.27 Arrhenius plots of $Ba_{0.5}Sr_{0.5}Co_{0.8}Fe_{0.2-x}Zn_xO_{3-\delta}$ and $Ba_{0.5}Sr_{0.5}Co_{0.8-x}Fe_{0.2}Zn_xO_{3-\delta}$ (x = 0, 0.05 and 0.1)

Table 3.19 Activation energy of $Ba_{0.5}Sr_{0.5}Co_{0.8}Fe_{0.2-x}Zn_xO_{3-\delta}$ and $Ba_{0.5}Sr_{0.5}Co_{0.8-x}Fe_{0.2}Zn_xO_{3-\delta}$ (x = 0, 0.05 and 0.1)

Sample	E_a (kJ/mol)
BSCF	36.17
FeZn0.05	34.51
FeZn0.1	32.40
CoZn0.05	34.30
CoZn0.1	33.14

3.4.1.2 Cu–doped BSCF

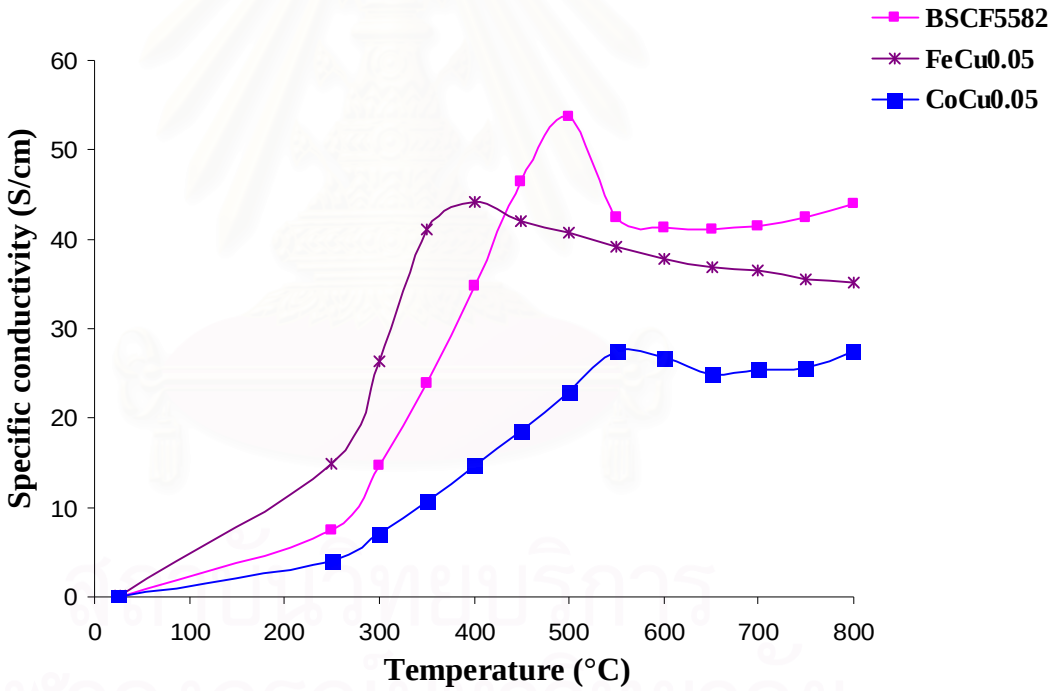

Figure 3.28 Variations of the electrical conductivity measured in air of $Ba_{0.5}Sr_{0.5}Co_{0.8}Fe_{0.2-x}Cu_xO_{3-\delta}$ and $Ba_{0.5}Sr_{0.5}Co_{0.8-x}Fe_{0.2}Cu_xO_{3-\delta}$ (x = 0, 0.05 and 0.1)

The electrical conductivity of BSCF doped with Cu indicated a semi–conducting behavior at low temperature (T ≤ 550°C) of these materials. Shown in Figure 3.28 and Table 3.20, the electronic conductivity of Cu specimen was lower than that of BSCF. The decrease in conductivity with the partial replacement of Co by

Cu in BSCF was due to an increase in the charge–transfer gap between the metal:3d and oxygen:2p bands and the decrease in the covalency of the metal–oxygen bonds [34]. Moreover, the electrical conductivity of FeCu specimen was more than that of CoCu, similar to the case of Zn specimens.

Table3.20 The specific conductivity of $Ba_{0.5}Sr_{0.5}Co_{0.8}Fe_{0.15}Cu_{0.05}O_{3-\delta}$ and $Ba_{0.5}Sr_{0.5}Co_{0.75}Fe_{0.2}Cu_{0.05}O_{3-\delta}$

Sample	Specific conductivity, σ (S/cm)						
	300°C	400°C	500°C	600°C	700°C	800°C	σ_{max} (T,°C)
BSCF	14.7	34.8	53.7	41.2	41.4	44.4	53.7 (500)
FeCu0.05	26.3	44.1	40.7	37.9	36.4	35.1	40.7 (500)
CoCu0.05	7.0	14.6	23.0	26.7	25.4	27.4	27.5 (550)

Shown in Table 3.21, the activation energies of Cu specimens were calculated from the linear part of Figure 3.29. The activation energies of Cu specimens were slightly different from that of BSCF.

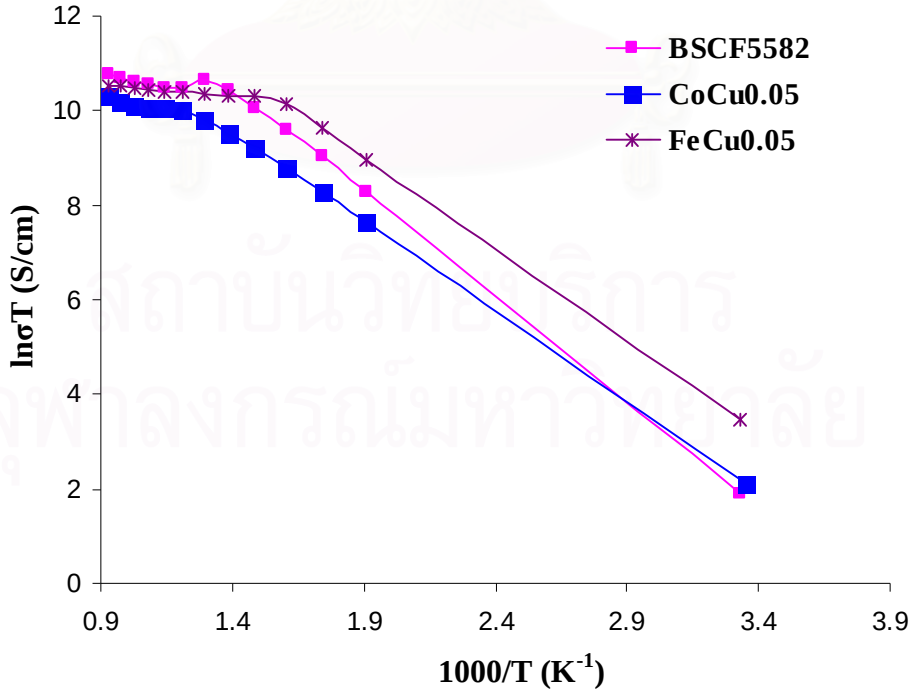

Figure 3.29 Arrhenius plots of $Ba_{0.5}Sr_{0.5}Co_{0.8}Fe_{0.2-x}Cu_xO_{3-\delta}$ and $Ba_{0.5}Sr_{0.5}Co_{0.8-x}Fe_{0.2}Cu_xO_{3-\delta}$ (x = 0, 0.05 and 0.1)

Table 3.21 Activation energy of $Ba_{0.5}Sr_{0.5}Co_{0.8}Fe_{0.2-x}Cu_xO_{3-\delta}$ and $Ba_{0.5}Sr_{0.5}Co_{0.8-x}Fe_{0.2}Cu_xO_{3-\delta}$ (x = 0, 0.05 and 0.1)

Sample	E_a (kJ/mol)
BSCF	36.17
FeCu0.05	31.47
CoCu0.05	30.93

3.4.2 Effect of A site doping on the electrical conductivity of BSCF

3.4.2.1 Pr–doped BSCF

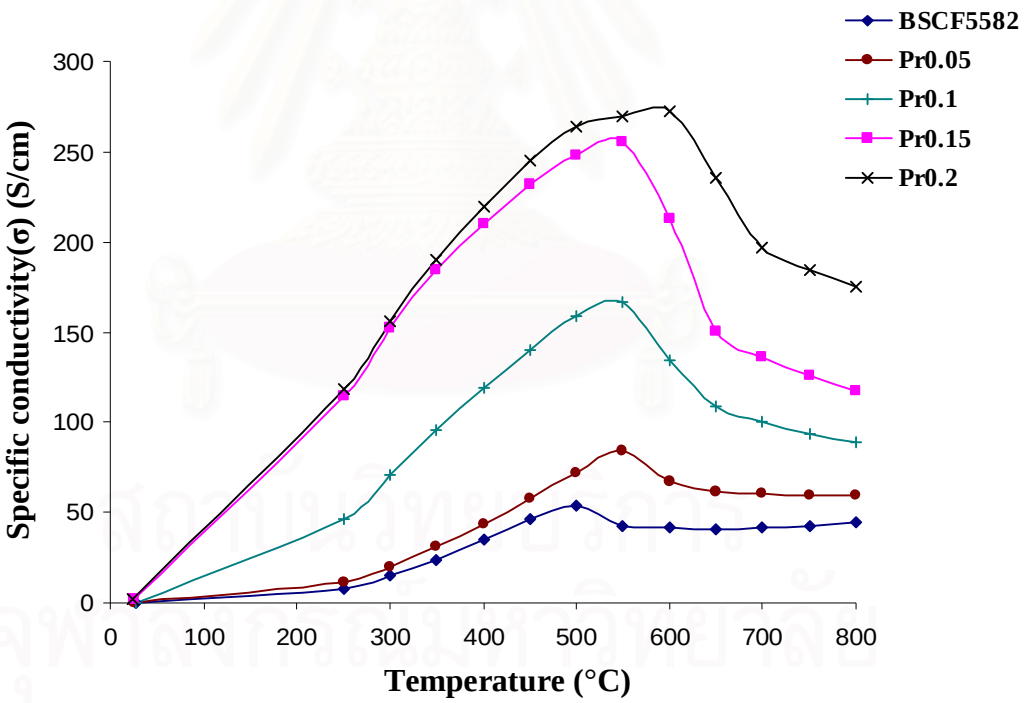

Figure 3.30 Variations of the electrical conductivity measured in air of $(Ba_{0.5}Sr_{0.5})_{1-x}Pr_xCo_{0.8}Fe_{0.2}O_{3-\delta}$ (x = 0, 0.05, 0.1, 0.15 and 0.2) with temperature

As can be seen in Figure 3.30 and Table 3.22, the electrical conductivity of all compounds increased gradually with temperature up to about 500–600 °C. It is noted that the electrical conductivity of Pr specimens increased with the amount of Pr. The

electrical conductivity of $(Ba_{0.5}Sr_{0.5})_{0.8}Pr_{0.2}Co_{0.8}Fe_{0.2}O_{3-\delta}$ reached the maximum of 272.4 S/cm at 600 °C and then decreased continuously. This is because the concentration of Co^{3+} and Fe^{3+} increased when bivalent Ba^{2+} and Sr^{2+} were substituted by trivalent Pr^{3+} for corresponding to the previous works of Li et al. [37]. Maintaining the electrical neutrality, the introduction of Pr^{3+}, which enhanced the average valence of the A site, induced the reduction of Co^{4+} and Fe^{4+} in B site to maintain the electrical neutrality. Therefore, the average valence of Co and Fe decreased corresponding to the increase of Co^{3+} and Fe^{3+}. Moreover, Co^{3+} and Fe^{3+} increased the concentration of electronic charge carriers and thus increased the electrical conductivity [39].

Table 3.22 The specific conductivity of $(Ba_{0.5}Sr_{0.5})_{1-x}Pr_xCo_{0.8}Fe_{0.2}O_{3-\delta}$ (x = 0, 0.05, 0.1, 0.15 and 0.2) in various temperature

Sample	Specific conductivity, σ (S/cm)						
	300°C	**400°C**	**500°C**	**600°C**	**700°C**	**800°C**	**σ_{max} (T,°C)**
BSCF	14.7	34.8	53.7	41.2	41.4	44.4	53.7 (500)
Pr0.05	20.0	43.9	72.0	67.2	60.2	60.0	84.1 (550)
Pr0.10	70.6	118.9	158.8	134.3	100.0	89.1	167.0 (550)
Pr0.15	152.1	210.5	247.5	213.1	136.4	117.6	255.9 (550)
Pr0.20	155.8	220.0	264.3	272.4	197.2	175.1	272.4 (600)

The activation energies of Pr specimens were calculated from the linear part of Arrhenius plots (Figure 3.31). Shown in Table 3.23, it can be clearly seen that the activation energy of Pr specimens decreased with the increase of the Pr contents as well as the electrical conductivity.

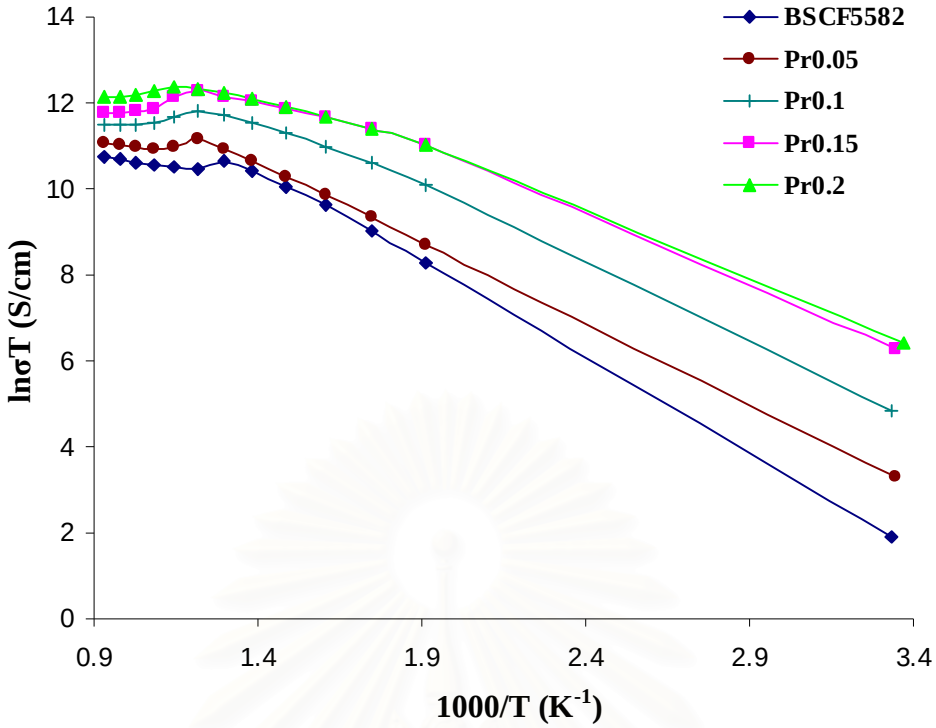

Figure 3.31 Arrhenius plots of $(Ba_{0.5}Sr_{0.5})_{1-x}Pr_xCo_{0.8}Fe_{0.2}O_{3-\delta}$ (x = 0, 0.05, 0.1, 0.15 and 0.2)

Table 3.23 Activation energy of $Ba_{0.5}Sr_{0.5}Co_{0.8}Fe_{0.2}O_{3-\delta}$ and $(Ba_{0.5}Sr_{0.5})_{1-x}Pr_xCo_{0.8}Fe_{0.2}O_{3-\delta}$ (x = 0, 0.05, 0.1, 0.15 and 0.2)

Sample	E_a (kJ/mol)
BSCF	36.17
Pr0.05	30.96
Pr0.10	28.03
Pr0.15	14.97
Pr0.20	14.77

3.4.2.2 La–doped BSCF

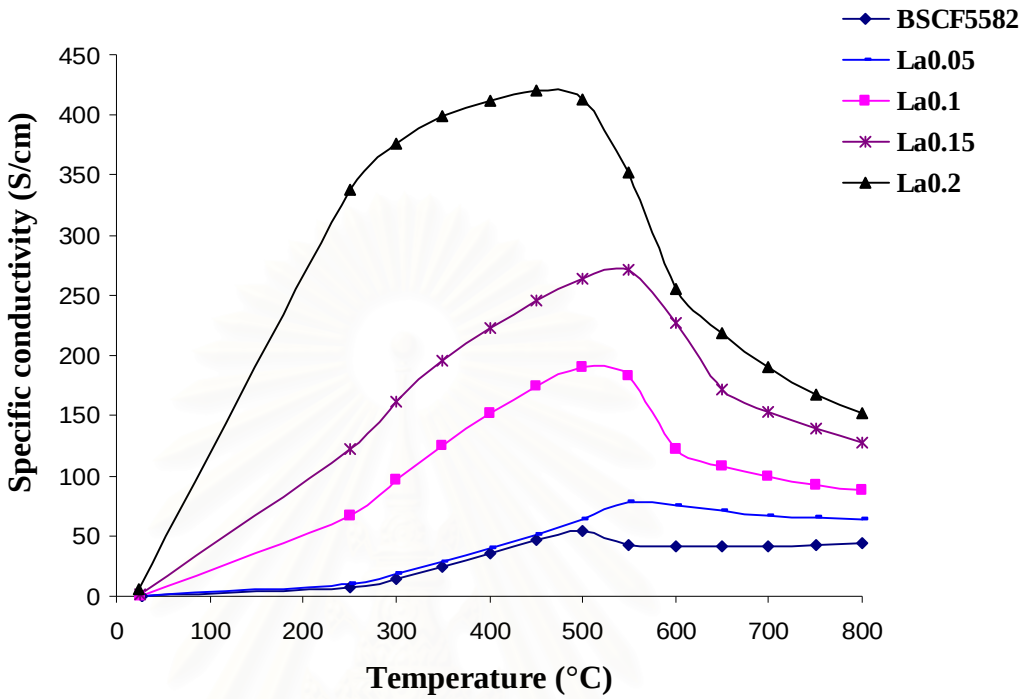

Figure 3.32 Variations of the electrical conductivity measured in air of $(Ba_{0.5}Sr_{0.5})_{1-x}La_xCo_{0.8}Fe_{0.2}O_{3-\delta}$ (x = 0, 0.05, 0.1, 0.15 and 0.2)

The electrical conductivity of La and Pr specimens showed similar trend (Figure 3.32 and Table 3.24). However, the maximum conductivity of the La specimen (419.6 S/cm at 450°C) was more than that of the Pr specimen (272.4 S/cm at 600°C). This result was consistent with previous research that the electrical conducting properties decreased by reducing the size of the lanthanide cations [40]. The decrease in the average cationic radius of the A site induced tilting and rotation of the BO_6 octahedron to accommodate the extra space that otherwise would be present around the A site. This occurrence reduced the B–O–B bond angle, which was unfavorable for the orbital overlap and consequently the B–O–B electrical transport. This hypothesis is believed to account for the degradation in electrical conducting properties with smaller lanthanide cation size [41, 42].

Table 3.24 The specific conductivity of $(Ba_{0.5}Sr_{0.5})_{1-x}La_xCo_{0.8}Fe_{0.2}O_{3-\delta}$ (x = 0, 0.05, 0.1, 0.15 and 0.2)

Sample	Specific conductivity, σ(S/cm)						
	300°C	400°C	500°C	600°C	700°C	800°C	σ_{max} (T,°C)
BSCF	14.7	34.8	53.7	41.2	41.4	44.4	53.7 (500)
La0.05	17.8	39.2	64.0	75.5	67.3	63.4	77.5 (550)
La0.10	96.7	151.3	189.7	122.2	99.1	87.9	189.7 (500)
La0.15	161.4	222.9	263.5	226.9	153.4	127.1	271.1 (550)
La0.20	376.8	411.8	412.4	255.1	189.8	151.5	419.6 (450)

In Table 3.25, the activation energies of La specimen were calculated from linear part of Arrhenius plots in Figure 3.33. Similar to Pr specimens, the activation energy decreased with increasing the amount of La.

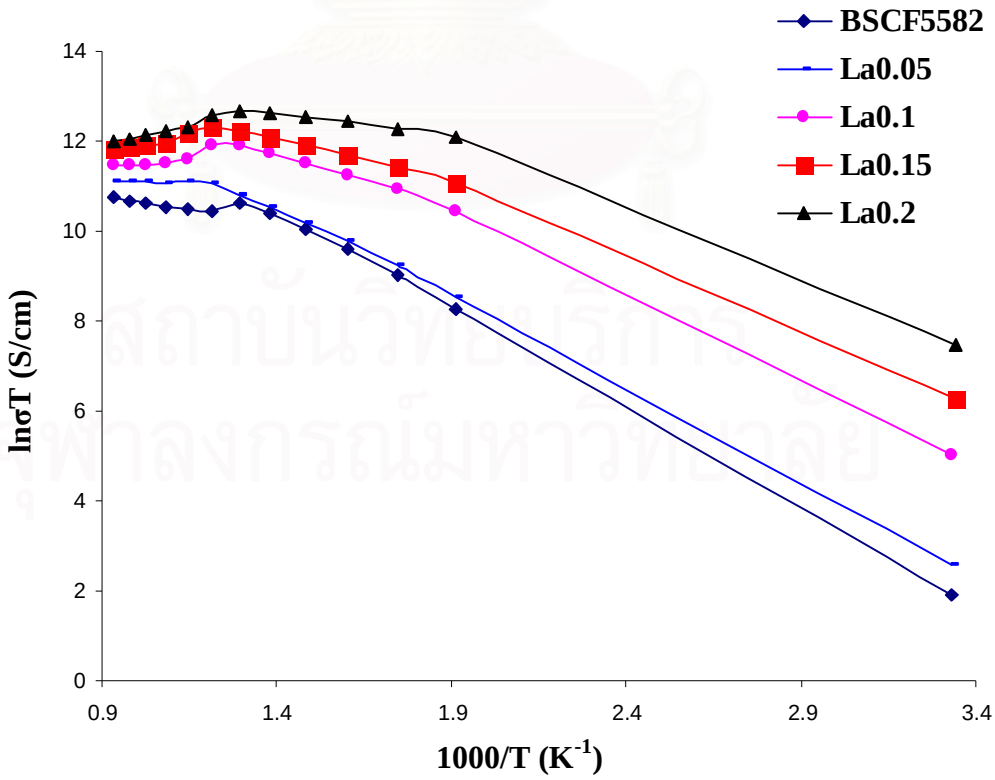

Figure 3.33 Arrhenius plots of $(Ba_{0.5}Sr_{0.5})_{1-x}La_xCo_{0.8}Fe_{0.2}O_{3-\delta}$ (x = 0, 0.05, 0.1, 0.15 and 0.2)

Table 3.25 Activation energy of $(Ba_{0.5}Sr_{0.5})_{1-x}La_xCo_{0.8}Fe_{0.2}O_{3-\delta}$ (x = 0, 0.05, 0.1, 0.15 and 0.2)

Sample	E_a (kJ/mol)
BSCF	36.17
La0.05	33.65
La0.10	19.37
La0.15	14.96
La0.20	8.44

3.4.3 Effect of both A and B site doping on the electrical conductivity of BSCF

3.4.3.1 Pr–and Cu–doped BSCF

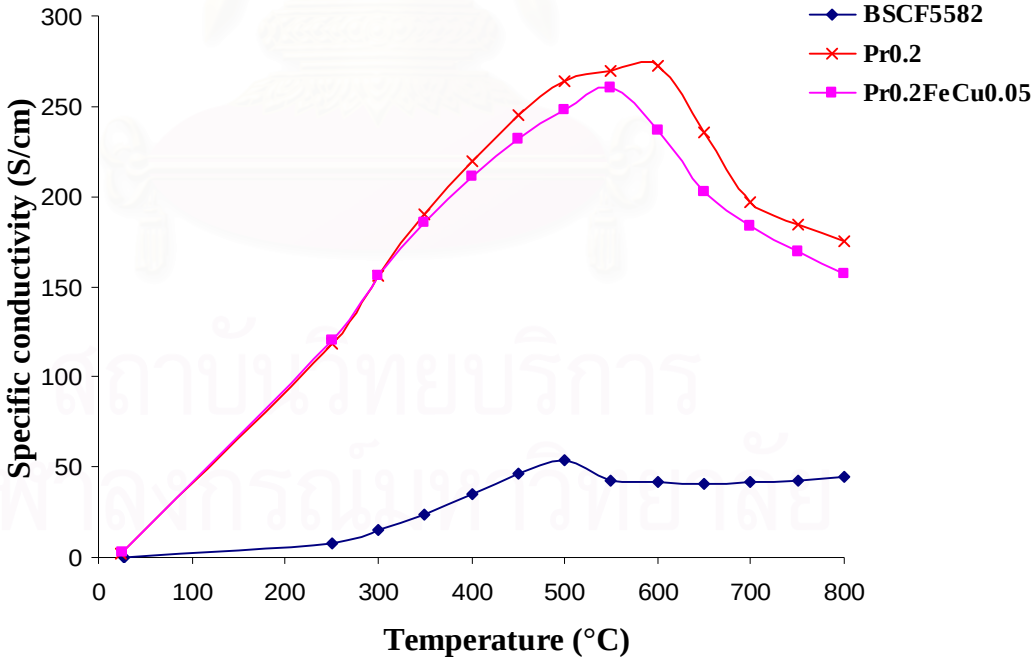

Figure 3.34 Variations of the electrical conductivity measured in air of $(Ba_{0.5}Sr_{0.5})_{0.8}Pr_{0.2}Co_{0.8}Fe_{0.15}Cu_{0.05}O_{3-\delta}$, $Ba_{0.5}Sr_{0.5}Co_{0.8}Fe_{0.2}O_{3-\delta}$ and $(Ba_{0.5}Sr_{0.5})_{0.8}Pr_{0.2}Co_{0.8}Fe_{0.2}O_{3-\delta}$ with temperature

As displayed in Figure 3.34 and Table 3.26, the maximum electrical conductivity of Pr0.2FeCu0.05 (260.1 S/cm at 550°C) was higher than that of BSCF (53.7 S/cm) but lower than Pr0.2 (272.4 S/cm at 600°C). Like the result observed BSCF, doping Cu in the structure of Pr–doped BSCF decreased its electronic conductivity.

Table 3.26 The specific conductivity of $(Ba_{0.5}Sr_{0.5})_{0.8}Pr_{0.2}Co_{0.8}Fe_{0.15}Cu_{0.05}O_{3-\delta}$, $Ba_{0.5}Sr_{0.5}Co_{0.8}Fe_{0.2}O_{3-\delta}$ and $(Ba_{0.5}Sr_{0.5})_{0.8}Pr_{0.2}Co_{0.8}Fe_{0.2}O_{3-\delta}$

Sample	Specific conductivity, σ(S/cm)						
	300°C	400°C	500°C	600°C	700°C	800°C	σ_{max} (T,°C)
BSCF	14.7	34.8	53.7	41.2	41.4	44.4	53.7 (500)
Pr0.20	155.8	220.0	264.3	272.4	197.2	175.1	272.4 (600)
Pr0.20FeCu0.05	156.4	211.5	248.1	236.4	183.6	156.7	260.1 (550)

Obtained from Figure 3.35, the activation energy of Pr0.2FeCu0.05 is shown in Table 3.27. The activation energy of Pr0.2FeCu0.05 was lower than that of Pr0.2, but higher than BSCF.

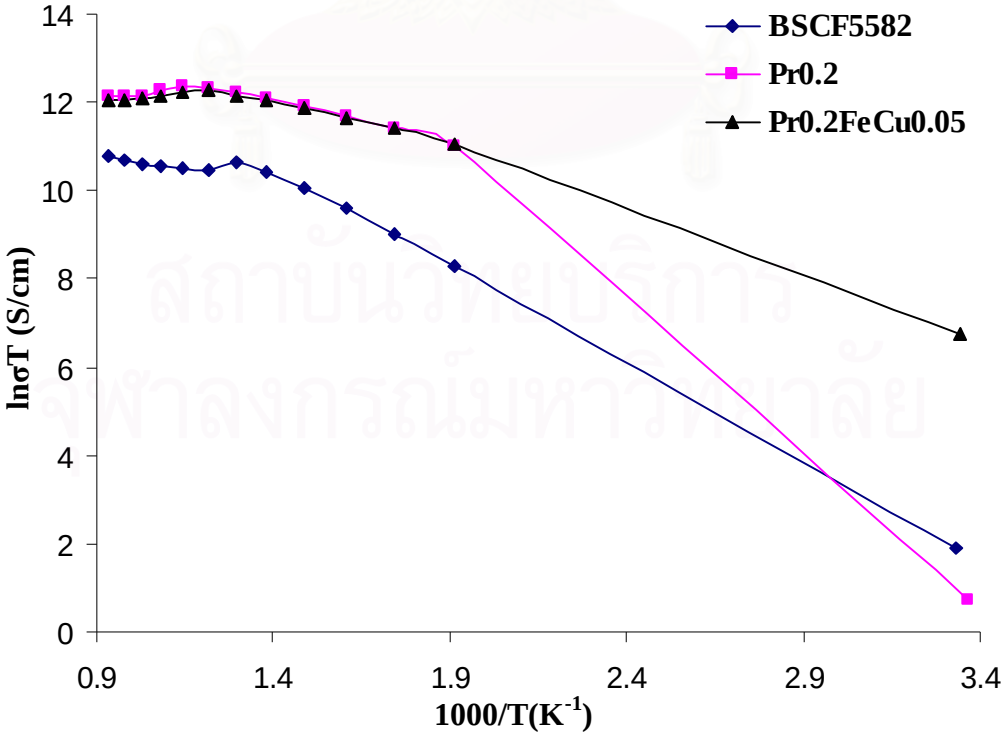

Figure 3.35 Arrhenius plots of $(Ba_{0.5}Sr_{0.5})_{0.8}Pr_{0.2}Co_{0.8}Fe_{0.15}Cu_{0.05}O_{3-\delta}$, $Ba_{0.5}Sr_{0.5}Co_{0.8}Fe_{0.2}O_{3-\delta}$ and $(Ba_{0.5}Sr_{0.5})_{0.8}Pr_{0.2}Co_{0.8}Fe_{0.2}O_{3-\delta}$

Table 3.27 Activation energy of $(Ba_{0.5}Sr_{0.5})_{0.8}Pr_{0.2}Co_{0.8}Fe_{0.15}Cu_{0.05}O_{3-\delta}$, $Ba_{0.5}Sr_{0.5}Co_{0.8}Fe_{0.2}O_{3-\delta}$ and $(Ba_{0.5}Sr_{0.5})_{0.8}Pr_{0.2}Co_{0.8}Fe_{0.2}O_{3-\delta}$

Sample	E_a(kJ/mol)
BSCF	36.17
Pr0.20	14.77
Pr0.2FeCu0.05	14.52

3.4.3.2 La and Cu–doped BSCF

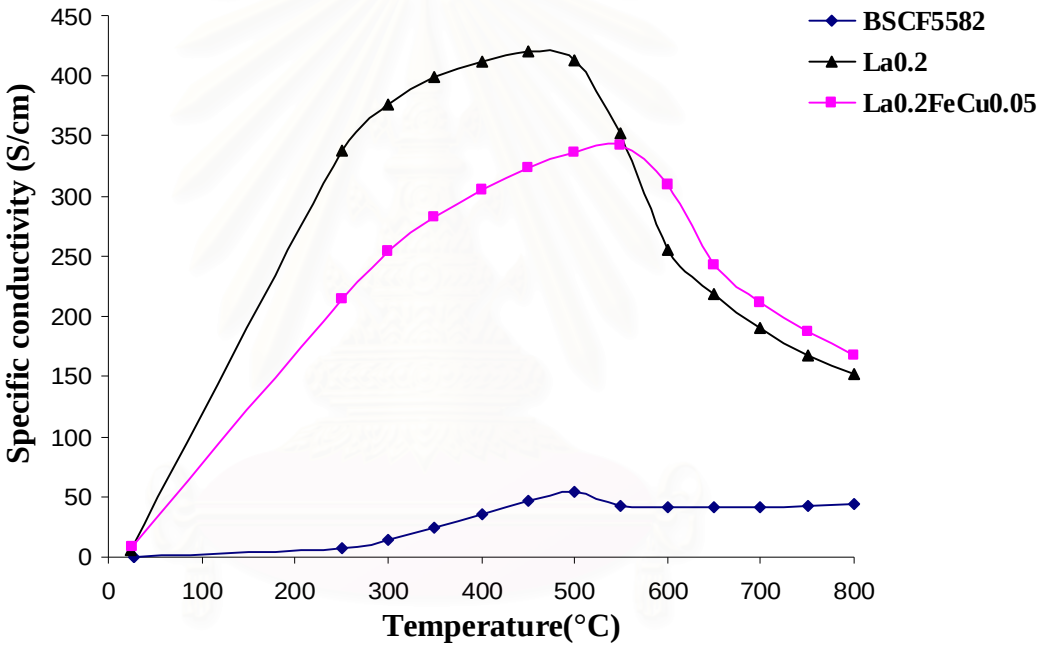

Figure 3.36 Variations of the electrical conductivity measured in air of $(Ba_{0.5}Sr_{0.5})_{0.8}La_{0.2}Co_{0.8}Fe_{0.15}Cu_{0.05}O_{3-\delta}$, $Ba_{0.5}Sr_{0.5}Co_{0.8}Fe_{0.2}O_{3-\delta}$ and $(Ba_{0.5}Sr_{0.5})_{0.8}La_{0.2}Co_{0.8}Fe_{0.2}O_{3-\delta}$ with temperature

Figure 3.36 and Table 3.28 show the electrical conductivity of La0.2FeCu0.05, compared with those of BSCF and La–doped BSCF. The electrical conductivity result of La0.2FeCu0.05 was similar to that of Pr0.2FeCu0.05. The maximum electrical conductivity of La0.2FeCu0.05 (342.5 S/cm at 550°C) was less than that of La0.2 (419.6 S/cm), but more than that of Pr0.2FeCu0.05 (260.1 S/cm at 550°C). It is confirmed that doping Cu at the B site of BSCF decreased the electrical conductivity.

Table 3.28 The specific conductivity of $(Ba_{0.5}Sr_{0.5})_{0.8}La_{0.2}Co_{0.8}Fe_{0.15}Cu_{0.05}O_{3-\delta}$, $Ba_{0.5}Sr_{0.5}Co_{0.8}Fe_{0.2}O_{3-\delta}$ and $(Ba_{0.5}Sr_{0.5})_{0.8}La_{0.2}Co_{0.8}Fe_{0.2}O_{3-\delta}$

Sample	Specific conductivity, σ(S/cm)						
	300°C	400°C	500°C	600°C	700°C	800°C	σ_{max} (T,°C)
BSCF	14.7	34.8	53.7	41.2	41.4	44.4	53.7 (500)
La0.20	376.8	411.8	412.4	255.1	189.8	151.5	419.6 (450)
La0.2FeCu0.05	253.9	305.9	336.5	309.4	211.0	168.0	342.5 (550)

From Figure 3.37 and Table 3.29, the activation energy of La0.2FeCu0.05 was more than that of La0.2, but less than that of BSCF.

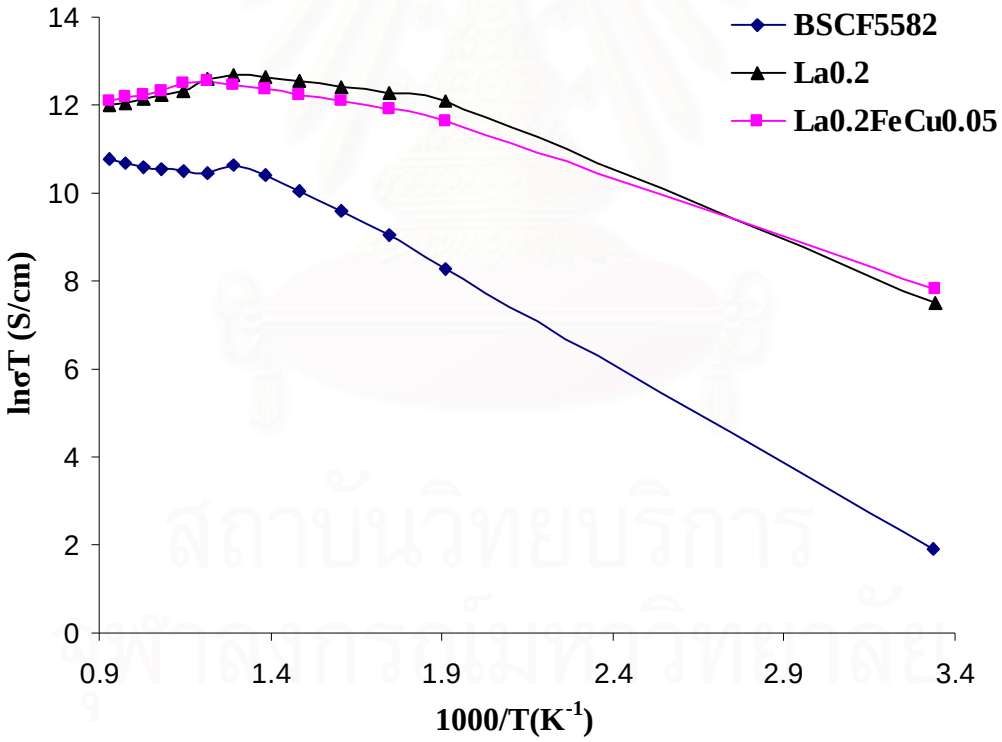

Figure 3.37 Arrhenius plots of $(Ba_{0.5}Sr_{0.5})_{0.8}La_{0.2}Co_{0.8}Fe_{0.15}Cu_{0.05}O_{3-\delta}$, $Ba_{0.5}Sr_{0.5}Co_{0.8}Fe_{0.2}O_{3-\delta}$ and $(Ba_{0.5}Sr_{0.5})_{0.8}La_{0.2}Co_{0.8}Fe_{0.2}O_{3-\delta}$

Table 3.29 Activation energy of $(Ba_{0.5}Sr_{0.5})_{0.8}La_{0.2}Co_{0.8}Fe_{0.15}Cu_{0.05}O_{3-\delta}$, $Ba_{0.5}Sr_{0.5}Co_{0.8}Fe_{0.2}O_{3-\delta}$ and $(Ba_{0.5}Sr_{0.5})_{0.8}La_{0.2}Co_{0.8}Fe_{0.2}O_{3-\delta}$

Sample	E_a(kJ/mol)
BSCF	36.17
La0.20	8.44
La0.2FeCu0.05	11.26

3.5 Effect of A and B–sites doping on thermal expansion of BSCF

From the conductivity part, it can be seen that doping with metal ions at A-site can improve the conductivity of BSCF. However, another important property for using as cathode material in solid oxide fuel cell is thermal expansion. The thermal expansion coefficients were measured by dilatometer.

3.5.1 Effect of A site doping on thermal expansion of BSCF

3.5.1.1 Pr–doped BSCF

Figure 3.38 illustrates the thermal expansion of $(Ba_{0.5}Sr_{0.5})_{1-x}Pr_xCo_{0.8}Fe_{0.2}O_{3-\delta}$ (x = 0.05, 0.1, 0.15 and 0.2) in air in the temperature range from room temperature to 800°C

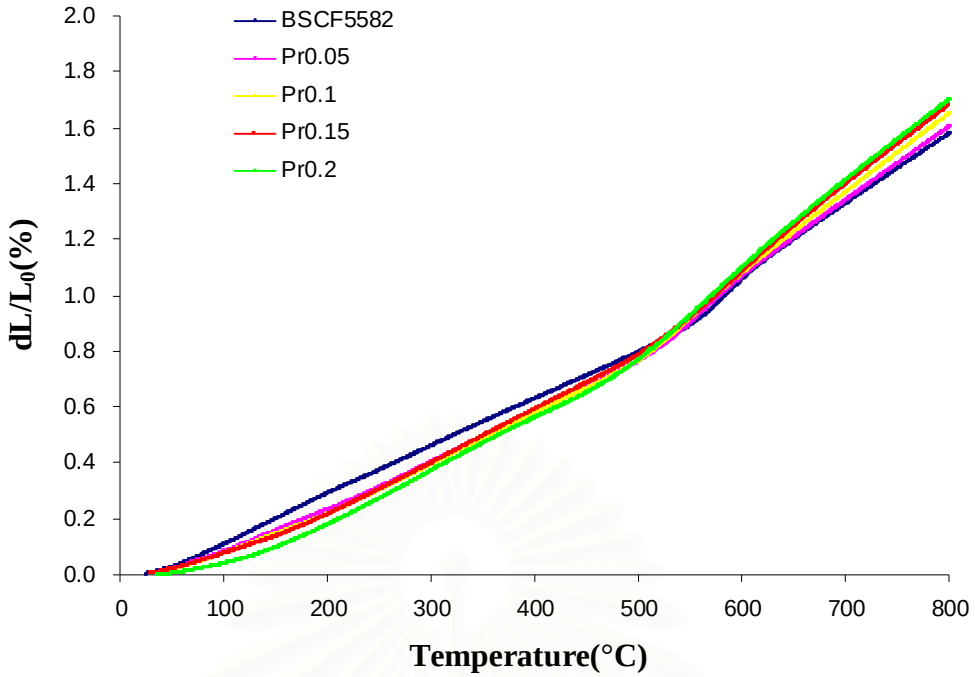

Figure 3.38 The thermal expansion curves for $(Ba_{0.5}Sr_{0.5})_{1-x}Pr_xCo_{0.8}Fe_{0.2}O_{3-\delta}$ (x = 0, 0.05, 0.1, 0.15 and 0.2)

The perovskite oxides expanded almost linearly in the temperature range 100–500°C but they became steeper at high temperature. The change of slope occurred about 490–560°C. The lattice expansion observed at high temperature may be attributed to the loss of oxygen and the formation of oxygen vacancies. There were two reasons for the lattice expansion concerned with the formation of oxygen vacancies. Firstly, the repulsion force arising between those mutually exposed cations when oxygen ions are extracted from the lattice. Secondly, the increase in cation size due to the reduction of Co and Fe ions from higher to lower valences, which must occur concurrently with formation of oxygen vacancies in order to maintain electrical neutrality, described in equation (1) and (2) [36, 38, 43].

$$2Co_{Co}^{\bullet} + O_O^{x} \rightleftharpoons 2Co_{Co}^{x} + V_O^{\bullet\bullet} + \frac{1}{2}O_2 \qquad (1)$$

$$2Fe_{Fe}^{\bullet} + O_O^{x} \rightleftharpoons 2Fe_{Fe}^{x} + V_O^{\bullet\bullet} + \frac{1}{2}O_2 \qquad (2)$$

Thermal reduction of Co^{4+}, Fe^{4+} to Co^{3+}, Fe^{3+} was found to occur at about 490–570°C. The thermal expansion curves occurred turning around this temperature suggested the reduction of Co^{4+} and Fe^{4+}. Therefore, the formation of oxygen vacancies enhanced the thermal expansion coefficients.

The thermal expansion coefficients of all samples are listed in Table 3.30

Table 3.30 The TEC values of $(Ba_{0.5}Sr_{0.5})_{1-x}Pr_xCo_{0.8}Fe_{0.2}O_{3-\delta}$ with(x = 0, 0.05, 0.1, 0.15 and 0.2)

Sample	Temperature range	TEC $x10^{-6}(°C^{-1})$	Turning Temperature(°C)
BSCF	100-500	18.3415	561.8
	650-800	25.6417	
Pr0.05	100-500	17.076	521.2
	600-800	26.8498	
Pr0.1	100-500	17.2494	509.6
	550-800	29.2793	
Pr0.15	100-500	17.7607	524.5
	550-800	30.5176	
Pr0.2	100-500	18.2169	490.3
	550-800	30.8474	

It can be seen that doping with Pr^{3+} at A site of BSCF increased the thermal expansion coefficient as compared with BSCF and it increased with increasing the Pr contents.

In Figure 3.39, the linear thermal expansion coefficients (TEC) are plotted versus Pr content at low and high temperature.

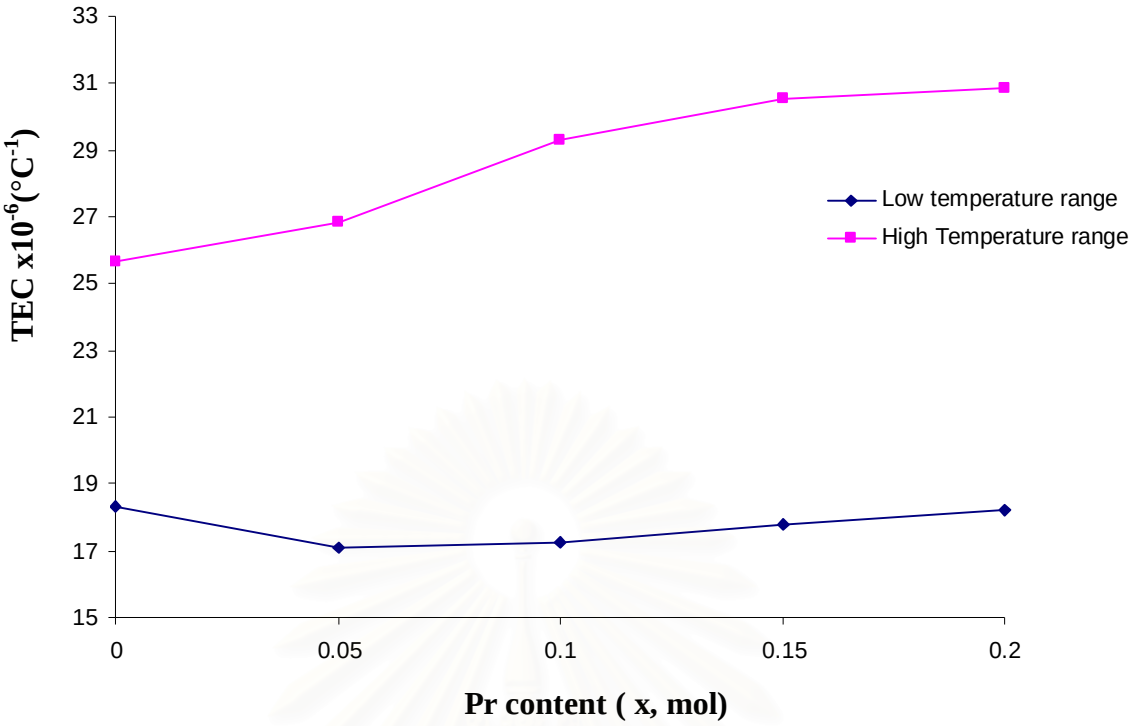

Figure 3.39 The thermal expansion coefficient VS x of $(Ba_{0.5}Sr_{0.5})_{1-x}Pr_xCo_{0.8}Fe_{0.2}O_{3-\delta}$ (x = 0.00, 0.05, 0.1, 0.15 and 0.2) as function of Pr content in air

The linear TEC at low temperature actually corresponding to the whole temperature range from 100°C up to about 500°C, was lower for x = 0.05 but at higher x values it showed a gradually increase. At high temperature, TEC increased with the increasing of Pr content. Hence, it is expected that the introduction of Pr^{3+} increased the amount of Co^{3+} and Fe^{3+} [44].

3.5.1.2 La–doped BSCF

The thermal expansion curves are shown in Figure 3.40 and TEC of the oxides are listed in Table 3.31. The thermal expansion coefficient of La^{3+} samples increased with increasing the amount of La^{3+}. They were similar to the results of Pr^{3+} but the TEC value of La^{3+} specimens were higher than those of Pr^{3+} and this results agree with the previous works of Kammer [26]. He reported that the TEC increased with increasing the size of the A-site cation.

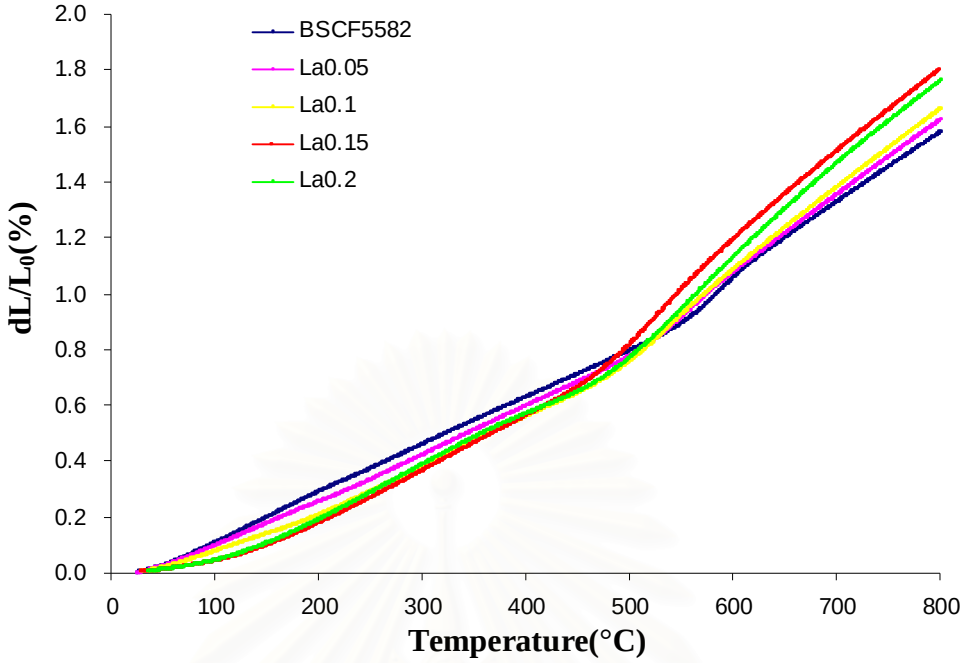

Figure 3.40 The thermal expansion curves for $(Ba_{0.5}Sr_{0.5})_{1-x}La_xCo_{0.8}Fe_{0.2}O_{3-\delta}$ (x = 0, 0.05, 0.1, 0.15 and 0.2)

Table 3.31 The TEC values of $(Ba_{0.5}Sr_{0.5})_{1-x}La_xCo_{0.8}Fe_{0.2}O_{3-\delta}$ (x = 0, 0.05, 0.1, 0.15 and 0.2)

Sample	Temperature range	TEC x10^{-6}(°C^{-1})	Turning Temperature(°C)
BSCF	100-500	18.3415	561.8
	650-800	25.6417	
La0.05	100-500	16.9718	520.5
	600-800	27.2986	
La0.1	100-450	16.1546	488.4
	600-800	28.719	
La0.15	100-450	17.7158	474.0
	600-800	30.5554	
La0.2	100-500	18.1225	485.7
	550-800	32.6338	

In Figure 3.41, the linear thermal expansion coefficients obtained from the slopes of the thermal expansion curves of Figure 3.40 are plotted against La content at low temperature and high temperature. At high temperature, TEC increase steadily as La content increased. At low temperature, TEC decreased in the range $0 \leq x \leq 0.1$ while for $x > 0.1$, it increased. This increase suggested the formation of oxygen vacancies.

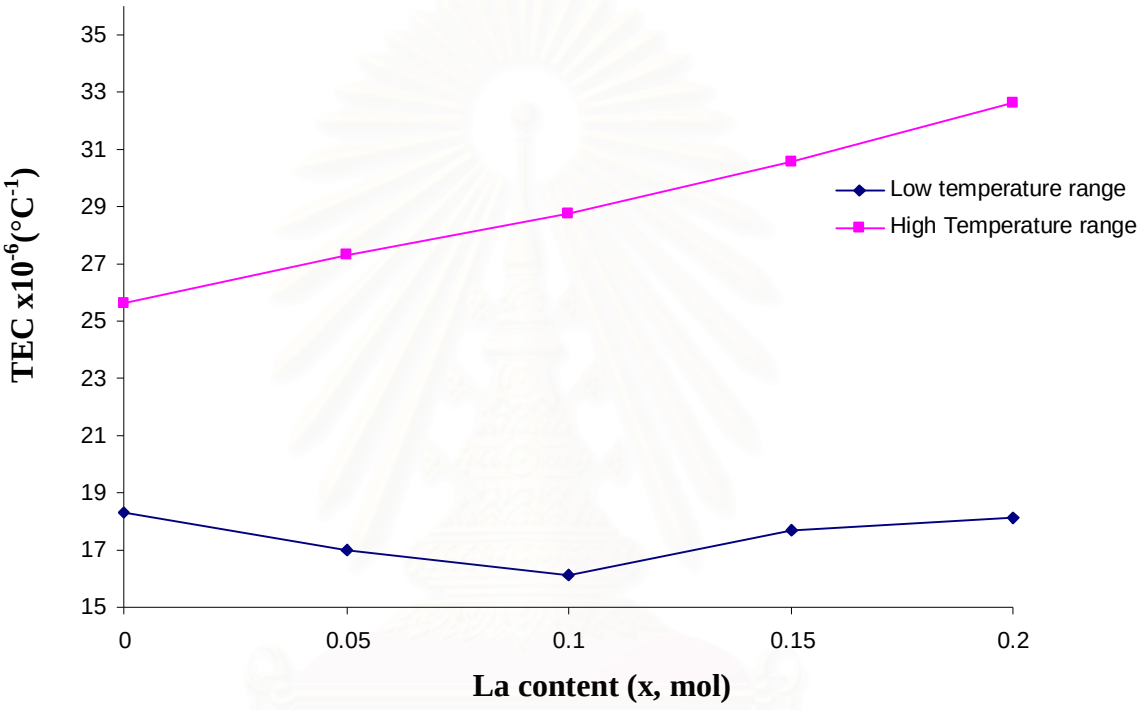

Figure 3.41 The thermal expansion coefficient VS x of $(Ba_{0.5}Sr_{0.5})_{1-x}La_xCo_{0.8}Fe_{0.2}O_{3-\delta}$ (x = 0.00, 0.05, 0.1, 0.15 and 0.2) in air

3.5.2 Effect of A and B site doping on thermal expansion of BSCF

In Figure 3.42 and Table 3.32, it can be clearly seen that doping with Cu at B site (Pr0.2FeCu0.05 and La0.2FeCu0.05) slightly decreased the TEC compared with undoped Cu at B site (Pr0.2 and La0.2). However, they were still more than BSCF. The TEC is inversely proportional to bonding energy between ions in the lattice [45]. It is expected that bonding energy of Cu–O is stronger than that of Fe–O corresponding to the works of Lee et al. [34]. They reported the tendency to form oxide ion vacancies increases in the order Ti<Cr<Mn<Cu<Fe<Co, implying that M-O

bond strength decreases on going from Ti to Co. Consequently, the TEC of doping with Cu at B site were lower than that of undoped Cu at B site.

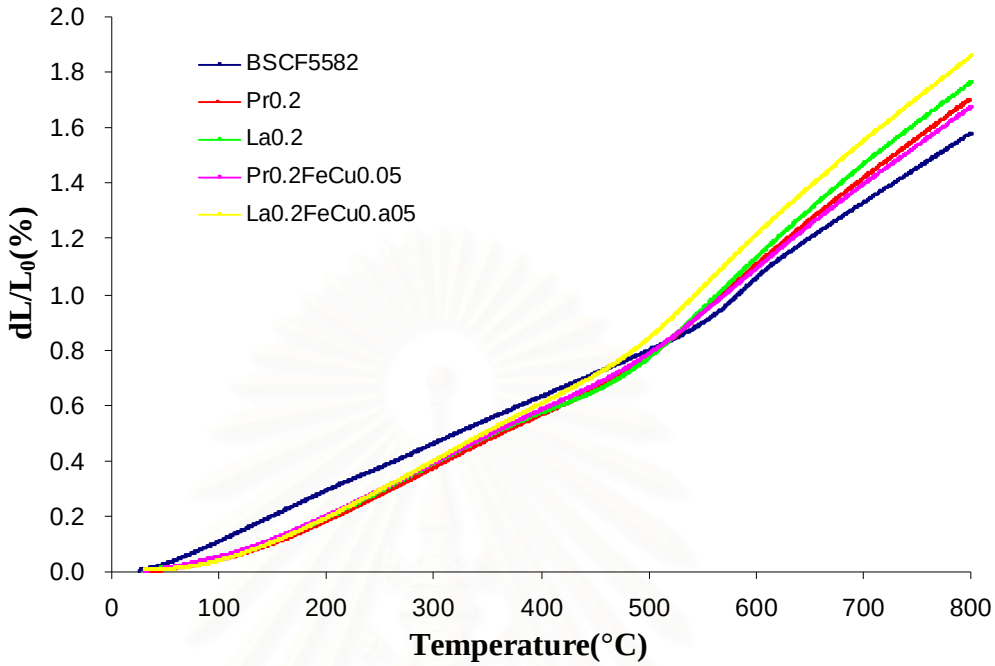

Figure 3.42 The thermal expansion curves for $(Ba_{0.5}Sr_{0.5})_{0.8}Pr_{0.2}Co_{0.8}Fe_{0.15}Cu_{0.05}O_{3-\delta}$ and $(Ba_{0.5}Sr_{0.5})_{0.8}La_{0.2}Co_{0.8}Fe_{0.15}Cu_{0.05}O_{3-\delta}$ compared with $Ba_{0.5}Sr_{0.5}Co_{0.8}Fe_{0.2}O_{3-\delta}$, $(Ba_{0.5}Sr_{0.5})_{0.8}Pr_{0.2}Co_{0.8}Fe_{0.2}O_{3-\delta}$ and $(Ba_{0.5}Sr_{0.5})_{0.8}La_{0.2}Co_{0.8}Fe_{0.2}O_{3-\delta}$.

Table 3.32 The TEC values of $(Ba_{0.5}Sr_{0.5})_{1-x}La_xCo_{0.8}Fe_{0.2}O_{3-\delta}$ (x = 0, 0.05, 0.1, 0.15 and 0.2)

Sample	Temperature range	TEC x10^{-6}(°C^{-1})	Turning Temperature(°C)
BSCF	100-500	18.3415	561.8
	650-800	25.6417	
Pr0.2	100-500	18.2169	490.3
	550-800	30.8474	
La0.2	100-500	18.1225	485.7
	550-800	32.6338	
Pr0.2FeCu0.05	100-500	18.2563	500.7
	600-800	29.082	
La0.2FeCu0.05	100-490	19.7499	490.4
	550-800	32.1234	

CHAPTER IV

CONCLUSIONS

$Ba_{0.5}Sr_{0.5}Co_{0.8}Fe_{0.2}O_{3-\delta}$(BSCF) doped with Pr and La ions at A site and Mg, Ni, Zn, and Cu ions at B site were synthesized by modified citrate method. From XRD and SEM results, there are a lot of impurity phase in all BSCF doped with Mg and Ni at Co and Fe site. On the contrary, all of Zn– and Cu–doped BSCF showed single phase with cubic perovskite–type structure and homogeneous, except FeCu0.1. For A site, the structure of Pr and La specimens were cubic and pure phase. The lattice parameters estimated from the XRD analysis was varied, according to the size of ionic cation. The ionic radius of Mg^{2+}, Ni^{2+}, Zn^{2+}, and Cu^{2+} were higher than that of Co and Fe, so the lattice parameters slightly increased for B site. On the other hand, the lattice parameters of Pr and La specimens gradually decreased with increasing the amount of metal ion contents (Pr and La) because the ionic radius of Pr^{3+} and La^{3+} were lower than that of Ba^{2+} and Sr^{2+} leading to shrinkage of the lattice. It showed that doping at A site affected on the lattice parameter more than doping at B site.

From O_2–TPD results, BSCF doped with metal ions at B site (Zn and Cu) had three oxygen desorption peaks. The amount of β and γ oxygen increased with increasing Zn and Cu content. In addition, those of Cu–doped BSCF were slightly higher than those of Zn–doped BSCF. Moreover, the replacement metal ions at Fe site had more influent on the release of oxygen lattice than Co site. It is suggested that Cu enhanced the oxygen vacancies more than Zn. For the results of doping at A site, the amount of β oxygen indicating oxygen vacancies increasing with the enhancement of Pr and La contents. La0.2 showed the highest β oxygen desorption (0.5261 mmol/g) indicating the highest oxygen vacancies. It can be concluded that doping at A site affected on oxygen vacancies more than doping at B site.

The electrical conductivity decreased with increasing the amount of Zn and Cu (B site) but increased with increasing the amount of Pr and La (A site). It is due to doping at A site stabilized by enhanced the reduction of Co^{4+} and Fe^{4+} to Co^{3+} and Fe^{3+} (small polaron) but doping at B site mainly stabilized by the formation of oxygen vacancies. Therefore, the electrical conductivity of BSCF doped with metal ion both A and B site were less than that of only A site. La0.2 also showed the highest

electrical conductivity (419.6 S/cm at 450°C) which was about 8 times higher than that of BSCF (53.7 S/cm at 500°C). It is concluded that the main factor for the electrical conductivity was small polaron.

For the thermal expansion results, the TEC values of doping at A site (Pr and La) increased with increasing Pr and La content because of the expansion of lattice, due to the formation of oxygen vacancies. Furthermore, The TEC values of doping with both A and B site were lower than that of only A site. La0.2 showed the highest TEC values ($32x10^{-6}$ $°C^{-1}$)

In conclusion, BSCF doped at A site (Pr and La) is good candidate for SOFC cathode material.

Suggestion

From all results, the future work should be focused on the study of the performance of Pr–and La–doped BSCF specimens used as cathode on the single cell.

REFERENCES

1. Sharke, P. Freedom of Choice *Mechanical Engineering* 126(2004) : 33.
2. Tejuca, L. G., Fierro, J. L. G. *Properties and Applications of Perovskite-type Oxides*, New York, Marcel Dekker, Inc., 1p, 1993.
3. Pen˜a, M. A.; Fierro J. L. G. Chemical Structures and Performance of Perovskite Oxides *Chemical Reviews* 101(2001) : 1981–2017.
4. Rao, C. N. R.; Gopalakrishnan, J.; Vidyasagar, K. Superstructure, Ordered Defects and Nonstoichiometry in Metal Oxides of Perovskite and elated Structure *Indian Journal of Chemistry 23A(4)*(1984) : 265-284.
5. Teraoka, Y.; Nobunaga, T.; and Yamazoe, N. Effect of Cation Substitution on the Oxygen Semipermeability of Perovskite-type Oxide *Chemistry Letters* (1988), 503-506.
6. Cui, X.; Liu, Y. New methods to prepare ultrafine particles of some perovskite-type oxides *Chemical Engineering Journal 78* (2000) : 205–209.
7. Hassel, V. B. A.; Kawada, T.; Sakai, N.; Yokokawa, H.; Dokiya, M.; Bouwmeester, H. J. M. Oxygen Permeation Modeling of Perovskites *Solid State Ionics 66*(1993) : 295–305.
8. Suresh, K.; Panchapagesan, T. S.; Patil, K. C. Synthesis and Properties of $La_{1-x}A_xFeO_3$ *Solid State Ionics 126* (1999) : 299–305.
9. Richerson, D. W. Modern Ceramic Engineering, Properties, Processing, and Use in Design 2nd ed. : p378-381, 1992.
10. Kuczynski, G. C. Transactions of the American Institute of Mining, Metallurgical, and Petroleum Engineering *Journal of Applied Physics* 21(1950) : 632-637.
11. Zhang, H. M.; Shimizu Y.; Teraoka Y.; Miuran, N.; Yamazoe, N. Oxygen sorption and catalytic properties of $La_{1-x}Sr_xCo_{1-y}Fe_yO_3$ perovskite-type oxides *Journal of catalysis* 121(1990) : 432-440
12. Tan, L.; Gu, X.; Yang, L.; Jin, W.; Zhang, L.; Xu, N. Influence of powder synthesis methods on microstructure and oxygen permeation performance of $Ba_{0.5}Sr_{0.5}Co_{0.8}Fe_{0.2}O_{3-\delta}$ perovskite-type membranes *Journal of Membrane Science* 212(2003) : 157–165.

13. Wang, H.; Tablet, T.; Feldhoff, A.; Caro, J. Investigation of phase structure, sintering, and permeability of perovskite-type $Ba_{0.5}Sr_{0.5}Co_{0.8}Fe_{0.2O3-\delta}$ membranes *Journal of Membrane Science* 262(2005) : 20–26.

14. Lee, S.; Lima Y.; Lee, E. A.; Hwang, H. J.; Moon J. W. $Ba_{0.5}Sr_{0.5}Co_{0.8}Fe_{0.2}O_{3-\delta}$ (BSCF) and $La_{0.6}Ba_{0.4}Co_{0.2}Fe_{0.8}O_{3-\delta}$ (LBCF) cathodes prepared by combined citrate-EDTA method for IT-SOFCs *Journal of Power Sources* 157(2006) : 848–854.

15. Lu, H.; Tong, J.; Deng, Z.; Cong, Y.; Yang, W. Crystal structure, oxygen permeability and stability of $Ba_{0.5}Sr_{0.5}Co_{0.8}Fe_{0.1}M_{0.1}O_{3\_d}$ (M = Fe, Cr, Mn, Zr) oxygen-permeable membranes *Materials Research Bulletin* 41(2006) : 683–689.

16. Duan, Z.; Yang, M.; Yan, A.; Hou, Z.; Dong, Y.; Chong, Y.; Cheng, M.; Yang, W. $Ba_{0.5}Sr_{0.5}Co_{0.8}Fe_{0.2}O_{3-\delta}$ as a cathode for IT-SOFCs with a GDC interlayer *Journal of Power Sources* 160(2006): 57–64.

17. Li, S.; L¨u, Z.; Wei, B.; Huang, X.; Miao, J.; Cao, G.; Zhu, R.; Su, W. A study of $(Ba_{0.5}Sr_{0.5})_{1-x}Sm_xCo_{0.8}Fe_{0.}2O_{3-\delta}$ as a cathode material for IT-SOFCs *Journal of Alloys and Compounds* 426(2006) : 408–414.

18. Li, S.; Lü, Z.; Huang, X.; Wei, B.; Su W. Electrical and thermal properties of $(Ba_{0.5}Sr_{0.5})_{1-x}Sm_xCo_{0.8}Fe_{0.2}O_{3-\delta}$ perovskite oxides *Solid State Ionics* 178(2007) : 417–422.

19. Wang , Y.; Wang, S.; Wang, Z.; Wen, T.; Wen, Z. Performance of $Ba_{0.5}Sr_{0.5}Co_{0.8}Fe_{0.2}O_{3-\delta}$-CGO-Ag cathode for IT-SOFCs *Journal of Alloys and Compounds* 428(2007) : 286–289.

20. Peña-Martínez, J.; Marrero-López, D.; Ruiz-Morales, J.C.; Buergler, B.E.; Núñez, P.; Gauckler, L.J. SOFC test using $Ba_{0.5}Sr_{0.5}Co_{0.8}Fe_{0.2}O_{3-\delta}$ as cathode on $La_{0.9}Sr_{0.1}Ga_{0.8}Mg_{0.2}O_{2.85}$ electrolyte *Solid State Ionics* 177 (2006) : 2143–2147

21. Meng, G.; Jiang, C.; Ma, J.; Ma, Q.; Liu, X. Comparative study on the performance of a SDC-based SOFC fueled by ammonia and hydrogen *Journal of Power Sources* xxx (2007) : xxx–xxx.

22. Mosadeghkhah, A.; Alaee, M. A.; Mohammadi, T. Effect of sintering temperature and dwell time and pressing pressure on

$Ba_{0.5}Sr_{0.5}Co_{0.8}Fe_{0.2}O_{3\_d}$ perovskite-type membranes *Materials and Design* 28(2007) : 1699–1706.

23. Subramania, A.; Saradha, T.; Muzhumathi, S. Synthesis of nano-crystalline $(Ba_{0.5}Sr_{0.5})Co_{0.8}Fe_{0.2}O_{3-\delta}$ cathode material by a novel sol–gel thermolysis process for IT-SOFCs *Journal of Power Sources* 165(2007) : 728–732.
24. Snezana, B.; Bos˘kovic´.; Branko, Z.; Matovic.; Milan, D.; Vlajic´.; Vladimir, D.; Kristic´. Modified glycine nitrate procedure (MGNP) for the synthesis of SOFC nanopowders *Ceramics International* 33(2007) : 89–93.
25. Chen, Z.; Ran, R.; Zhou, W.; Shao, Z.; Liu, S. Assessment of $Ba_{0.5}Sr_{0.5}Co_{1-y}Fe_yO_{3-\delta}$ (y = 0.0–1.0) for prospective application as cathode for IT-SOFCs or oxygen permeating membrane *Electrochimica Acta* 52(2007) : 7343–7351.
26. Kammer K. Studies of Fe–Co based perovskite cathodes with different A-site cations *Solid State Ionics* 177(2006) : 1047–1051.
27. Lv, H.; Zhao, B. Y.; Wu, Y. J.; Sun, G.; Chen, G.; Hu, K. A. Effect of B-site doping on $Sm_{0.5}Sr_{0.5}M_xCo_{1\_x}O_{3\_d}$ properties for IT-SOFC cathode material (M = Fe, Mn) *Materials Research Bulletin* 42(2007) : 1999–2012.
28. Teraoka, Y.; Furukawa, S.; Zhang, H. M.; Yamazoe, N., *Nippon kaguku kaishi*, 1988, 1084.
29. Vijayanandhini, K.; Kutty T. R. N. Effects of Zn substitution on the magnetic and transport properties of $La_{0.6}Sr_{0.4}Mn_{1-y}Zn_yO_{3-\_}$ (0 _ y _ 0.3) *Solid State Communications* 141(2007) : 252–257.
30. Zongping, S.; Weishen, Y.; You, C.; Hui, D.; Jianhua, T.; Guoxing, X. Investigation of the permeation behavior and stability of a $Ba_{0.5}Sr_{0.5}Co_{0.8}Fe_{0.2}O_{3-\delta}$ oxygen membrane *Journal of Membrane Science* 172 (2000) : 177–188.
31. Chung, Y. T.; Anthony, G. D.; Yi, H. M.; William, R. M.; Marina, R. P. Dense Perovskite, $La_{1-x}A^*_xFe_{1-y}Co_yO_{3-\delta}$ (A* = Ba, Sr, Ca), Membrane Synthesis, Applications, and Characterization *Journal of American Ceramic Society* 81[6](1998) : 1437–1444.

32. Pei, S.; Kleefisch, M. S.; Kobylinski, T. P.; Faber, J.; Udovich, C. A.; Zhang, V. M.; Dabrowski, B.; Balachandran, U.; Mieville, R. L.; Poeppel, R. B. Failure mechanisms of ceramic membrane reactors in partial oxidation of methane to synthesis gas *Catalysis Letters* 30(1995) : 201–212.

33. Teraoka, Y.; Yoshimatsu, M.; Yamazoe, N.; Seiyama, T., *Chemistry letters* (1984) 893.

34. Lee, K. T. Effect of cation doping on the physical properties and electrochemical performance of $Nd_{0.6}Sr_{0.4}Co_{0.8}M_{0.2}O_{3-\delta}$ (M=Ti, Cr, Mn, Fe, Co, and Cu) cathodes, Manthiram, A.; *Solid State Ionics* 178(2007) : 995–1000.

35. Subramania , A.; Saradha , T.; Muzhumathi S. Synthesis of nano-crystalline $(Ba_{0.5}Sr_{0.5})Co_{0.8}Fe_{0.2}O_{3-\delta}$ cathode material by a novel sol–gel thermolysis process for IT-SOFCs *Journal of Power Sources* 165 (2007) : 728–732.

36. Tai, L. W.; Nasrallah, M. M.; Anderson, H. U.; Sparlin, D. M.; Sehlin, S. R. Structure and electrical properties of $La_{1-x}Sr_xCo_{1-y}Fe_yO_3$. Part 1. The system $La_{0.8}Sr_{0.2}Co_{1-y}Fe_yO_3$ *Solid State Ionics* 76(1995) : 259-27.

37. Wei, B.; L¨u, Z.; Huanga, X.; Liu, M.; Lia, N.; Sua, W. Synthesis, electrical and electrochemical properties of $Ba_{0.5}Sr_{0.5}Zn_{0.2}Fe_{0.8}O_{3-\delta}$ perovskite oxide for IT-SOFC cathode *Journal of Power Sources* 176(2008) : 1–8.

38. Li, S.; Lü, Z.; Huang, X.; Su, W. Thermal, electrical, and electrochemical properties of Nd-doped $Ba_{0.5}Sr_{0.5}$ $Co_{0.8}Fe_{0.2}O_{3-\delta}$ as a cathode material for SOFC *Solid State Ionics* 178(2008) : 1853–1858.

39. Hashimoto, S.; Kammer, K.; Larsen, P. H.; Poulsen, F. W. Mogensen, M. A study of $Pr_{0.7}Sr_{0.3}Fe_{1\_x}Ni_xO_{3\_d}$ as a cathode material for SOFCs with intermediate operating temperature *Solid State Ionics* 176(2005) : 1013–1020.

40. Xu, Q.; Huang, D.; Chen, W.; Zhang, F.; Wang, B. Structure, electrical conducting and thermal expansion properties of $Ln_{0.6}Sr_{0.4}Co_{0.2}Fe_{0.8}O_3$ (Ln = La, Pr, Nd, Sm) perovskite-type complex oxides *Journal of Alloys and Compounds* 429(2007) : 34–39.

41. Uhlenbruck, S.; Tietz, F. High-temperature thermal expansion and conductivity of cobaltites: potentials for adaptation of the thermal expansion to the demands for solid oxide fuel cells *Materials Science and Engineering* B107(2004) : 277–282.

42. Cherif, K.; Dhahri, J.; Dhahri, E.; Oumezzine, M.; Vincent, H. Effect of the A Cation Size on the Structural, Magnetic, and Electrical Properties of Perovskites $(La_{1\_x}Nd_x)_{0.7}Sr_{0.3}MnO_3$ *Journal of Solid State Chemistry* 163(2002) : 466–471.

43. Shao, Z.; Xiong , G.; Tong, J.; Dong, H.; Yang, W. Ba effect in doped $Sr(Co_{0.8}Fe_{0.2})O_{3-\_}$ on the phase structure and oxygen permeation properties of the dense ceramic membranes *Separation and Purification Technology* 25(2001) : 419–429.

44. Li, S.; Lu, Z.;e Huang, X.; Wei, B.; Sua, W. Thermal, electrical, and electrochemical properties of Lanthanum-doped $Ba_{0.5}Sr_{0.5}Co_{0.8}Fe_{0.2}O_{3-d}$ *Journal of Physics and Chemistry of Solids* 68(2007) : 1707–1712.

45. Hayashia, H.; Kanoha, M.; Quana, C. J.; Inabaa, H.; Wangb, S.; Dokiya, M.; Tagawa, H. Thermal expansion of Gd-doped ceria and reduced ceria *Solid State Ionics* 132(2000) : 227–233.

46. Shannon, R.D. Revised effective ionic radii and systematic studies of interatomic distances in halides and chalcogenides *Acta Crystallographica* A32(1976) : 751–753.

APPENDICES

APPENDICES

APPENDICE A

Tolerance number

Goldschmidt (1926) defined the tolerance limits of the size of ions through a tolerance factor, t as Equation (A.1)

$$t = (r_A + r_O)/ [\sqrt{2} (r_B + r_O)] \quad (A.1)$$

where r_A, r_B, and r_O are the radii of respective ions. For the substituted perovskite at A and B site, $A_{1-x}A'_xB_{1-y}B'_yO_{3-\delta}$, r_A and r_B were calcuated from the sum of each metal at A site and B site, respectively, time its compostition. The atomic weight, ionic charge, coordination number, and ionic radius of all concerned metals were shown in Table A.1

Table A.1 Atomic weight, ionic charge, coordination number, and ionic radius of concerned metals[46]

Element	Charge	Ionic radius
Ba	2+	1.750
Sr	2+	1.580
Co	2+	0.890
Co	3+	0.750
Co	4+	0.670
Fe	2+	0.920
Fe	3+	0.785
Fe	4+	0.725
Mg	2+	0.860
Ni	2+	0.830
Zn	2+	0.880
Cu	1+	0.910
Cu	2+	0.870
Cu	3+	0.680
Pr	3+	1.319
La	3+	1.500
O	2-	1.260

Therefore, as Equation A.1 the tolerance number of perovskite compounds such as LSGF 6428 was calculated as below.

$$\text{tolerance number of LSCF8264} = \frac{(1.36 \times 0.8) + (1.44 \times 0.2) + 1.40}{\sqrt{2}\,[(0.65 \times 0.8) + (0.62*0.2) + 1.40]}$$

$$= 1.43$$

APPENDICE B

$$\sigma = (A/T)\, e^{(-Ea/RT)}$$

$$\ln(\sigma T) = \ln A\, e^{(-Ea/RT)}$$

$$\ln(\sigma T) = \ln e^{(-Ea/RT)} + \ln A$$

$$\ln(\sigma T) = (-E_a/R)\,(1000/T) + \ln A$$

y **slope** **x** **intercept y axis**

$$-E_a/K = \text{Slope of the linear}$$

$$E_a = -\text{Slope}*K$$

σ = The specific conductivity (S/cm)

E_a = The activation energy (kJ/mol)

T = Temperature (K)

R = The gas constant = 8.314472 J/K.mol

For example

BSCF ; The linear equation is

$$y = -4.3499x + 16.493$$

$$\text{Slope} = -4.3499 = -E_a/R$$

Then, $E_a = -4.3499 \times 8.314472 = 36.17$ kJ/mol

VITAE

Mr. Watcharin Ngampeungpis was born on April 10, 1983 in Bangkok, Thailand. He graduated with Bachelor's Degree in Chemistry from Faculty of Science, Chulalongkorn University in 2005. He continued his study in Department of Chemistry, Faculty of Science, Chulalongkorn University in 2005 and completed in 2008.